UNIVERSITY OF SOUTHAMPTON

FACULTY OF PHYSICAL AND APPLIED SCIENCES

Engineering and the Environment

A Numerical Study of some Vortex Ring Phenomena using Direct Numerical Simulation (DNS)

by

Shankar Kumar Balakrishnan

Thesis for the degree of Doctor of Philosophy

June 2013

UNIVERSITY OF SOUTHAMPTON

ABSTRACT

FACULTY OF PHYSICAL AND APPLIED SCIENCES
Engineering and the Environment

Doctor of Philosophy

A NUMERICAL STUDY OF SOME VORTEX RING PHENOMENA USING DIRECT NUMERICAL SIMULATION (DNS)

by Shankar Kumar Balakrishnan

Direct numerical simulation (DNS) is used to study some aspects of the dynamics of vortex rings in viscous, incompressible flow at Reynolds numbers (defined as the ratio of the initial circulation to the kinematic viscosity) in the range of 10^3 to 10^4.

Firstly, the effect of the particular initial core azimuthal vorticity profile of a vortex ring on its subsequent evolution in unbounded flow is studied. Vortex rings with a wide range of initial core vorticity profiles are shown to relax to a common equilibrium state. Additionally the behaviour of the equilibrium vortex ring at large times is studied. When the slenderness ratio of the vortex rings increases beyond a particular limit, the vortex rings diverge from the common equilibrium state and follow paths determined by the viscosity of the fluid.

Secondly, the interaction of a laminar vortex ring with a non-deformable, free-slip surface at an oblique angle of incidence leading to the phenomenon of vortex reconnection is investigated. Specifically the effect of Reynolds number on the dynamics of the reconnection process is studied. The scaling of the reconnection timescale with the Reynolds number is obtained. At high Reynolds numbers the reconnection process leads to a breakdown of the entire vortex ring structure to a turbulent-like flow. This phenomenon is shown to be related to the mechanics of the reconnection process.

Finally, the dynamics of vortex rings with swirl in unbounded flow is studied. Two different types of vortex rings with swirl were considered: i) Vortex rings with Gaussian distributions of core azimuthal vorticity and core azimuthal velocity and ii) Steady state solutions of the Euler equations for vortex rings with swirl. Both types of vortex rings develop an elongated axial vortex after initialisation. The existence of a maximum limit for the swirl on a vortex ring is shown above which the vortex rings undergo a rapid de-swirling readjustment. A helical instability occurring in vortex rings due to swirl at high Reynolds numbers is presented. A relation is shown to exist between one of the modes of the helical instability and the geometric parameters of the vortex ring.

Contents

List of Figures

List of Tables

Declaration of Authorship

I, Shankar Kumar Balakrishnan , declare that the thesis entitled *A Numerical Study of some Vortex Ring Phenomena using Direct Numerical Simulation (DNS)* and the work presented in the thesis are both my own, and have been generated by me as the result of my own original research. I confirm that:

- this work was done wholly or mainly while in candidature for a research degree at this University;
- where any part of this thesis has previously been submitted for a degree or any other qualification at this University or any other institution, this has been clearly stated;
- where I have consulted the published work of others, this is always clearly attributed;
- where I have quoted from the work of others, the source is always given. With the exception of such quotations, this thesis is entirely my own work;
- I have acknowledged all main sources of help;
- where the thesis is based on work done by myself jointly with others, I have made clear exactly what was done by others and what I have contributed myself;
- parts of this work have been published as: (Balakrishnan et al., 2011)

Signed:.....

Date:.....

Acknowledgements

I would like to express my gratitude to my supervisors Dr. Gary Coleman and Dr. Glyn Thomas. Working with both of them has been a wonderful learning experience. I'd like to thank Gary firstly for providing me the opportunity to do a Ph.D. and further for his advice, encouragement and constant support throughout. His knowledge along with his kind and patient guidance made him an ideal supervisor. I'm thankful to Glyn for the many hours of engrossing discussions about vortex rings during which he patiently answered all my questions. His immense knowledge and ability to analyse and quickly identify the crux of a problem rescued me from many a tricky situation when I was lost in the details. His infectious enthusiasm for fluid mechanics was also a great source of encouragement.

I am very thankful to Dr. Phil Archer for his tremendous help and guidance during the crucial early stages of my Ph.D. I would also like to thank my fellow Ph.D. students, Dr. Watchapon Rojanaratanangkule and Azad Noorani for our several valuable discussions. Thanks also to Dr. Roderick Johnstone for his help with the spectral code.

I am grateful to the UK Overseas Research Students Award Scheme (ORSAS) and the University of Southampton for providing the funding necessary for my Ph.D.

Thanks to my friends - flat mates, office mates and cricket team mates especially Aditya Prabhakar, Azad, Aditya Karnik and Negus for the many chats and the fun times we had.

Most importantly I would like to express my deep gratitude to my parents without whose love, advice and incredible support I could not have reached this far. Thanks to Uma and Badri for the many relaxing and enjoyable holidays I had with them away from work.

Finally I'd like to thank Prof. S. N. Balagangadhara whose fascinating work provided me with great intellectual stimulation outside of fluid mechanics and taught me what true science is.

Nomenclature

Roman symbols

A	circulation transfer rate
$\mathcal{A}$	axial component of angular impulse
c	celerity
C	translation parameter
E	energy
F_K	flux of kinetic energy
g	gravitational acceleration
h	depth of vortex ring centre from free-slip surface at initial time
H	sum of convective and diffusive terms
I	axial component of linear impulse
k	wavenumber
K	kinetic energy
L_x, L_y, L_z	box lengths
n_θ	twisting mode
n_ϕ	shaping mode
N_x, N_y, N_z	number of grid cells in the x,y and z directions
p	pressure
Q	second invariant of the velocity gradient tensor
r	radial coordinate
R	ring radius
Re	Reynolds number
S	swirl parameter
t	time
t_1	time at the beginning of the circulation transfer
T_R^*	normalised reconnection time
u, v, w	Cartesian velocity components
u_r, u_θ, u_z	cylindrical velocity components
u^*	provisional velocity
$\tilde{w}$	velocity induced by periodic image rings
W_{ref}	Speed of the comoving reference frame
X	location of vortex ring along x-axis with respect to

	comoving reference frame
x, y, z	Cartesian coordinates
Z	axial location of vortex ring with respect to comoving reference frame

Greek symbols

α, β	parameters defining Euler solution initialised vortex ring
γ	initial inclination of vortex ring axis to surface
δ	core radius
ϵ	slenderness ratio
ϵ_K	dissipation
ζ	exponent of power law representing vorticity density
η	perturbation amplitude
θ	ring azimuthal coordinate
λ	wavelength of helical instability
ν	kinematic viscosity
ρ	density
σ	radial distance from toroid centreline
ϕ	core azimuthal coordinate
ψ	Stokes stream function
ω	vorticity
Γ	circulation
$\mathbf{\Psi}$	vector stream function
Ω	enstrophy

Subscripts

$_0$	initial condition
$_{\max}$	maximum value
$_{i,j,k}$	indices for Cartesian tensor notation
$_r$	quantity value at beginning of circulation transfer
$_\parallel$	quantity value along surface-parallel direction
$_\perp$	quantity value along surface-normal direction

Chapter 1

Introduction

Vortex rings are ubiquitous in nature and their dynamics include a range of interesting phenomena which have been investigated for more than a century through experimental and numerical studies and theoretical analysis. Apart from its importance in several engineering and environmental flows, vortex ring dynamics also provides simpler, canonical instances of the various vortical interactions that occur in more complex turbulent flows. Direct numerical simulation (DNS) has been increasingly used to gain a better understanding of these phenomena. The present work uses DNS to focus primarily on three aspects of vortex rings in viscous, incompressible flow: i) The evolution of vortex rings without swirl ('classical' vortex rings) in unbounded flow ii) The oblique angle interaction of a vortex ring with a non-deformable free-slip surface resulting in vortex reconnection with the surface and iii) The dynamics of vortex rings with swirl in unbounded flow.

1.1 Classical vortex rings

In numerical simulations of vortex ring dynamics we need to consider the issue of the initialisation of the vortex ring. The initialisation involves the selection of a profile that represents the variation of azimuthal vorticity within the finite core of the vortex ring. A standard practice used in numerical simulations of vortex rings is to use a circular core with a Gaussian distribution of vorticity. However, the Gaussian profile is only an exact solution for the Navier-Stokes equations in the limit of a vanishingly thin core. A Gaussian-initialised vortex ring with a finite core size would undergo a readjustment to a different vorticity profile. Such a rapid initial readjustment involving changes in the structure of the vortex core is seen in both experiments (Dabiri and Gharib, 2004) and numerical simulations (Stanaway et al., 1988; Archer et al., 2008). After this initial transient phase, the vortex rings reach a quasi-steady state (referred to in this report

as an 'equilibrium state') wherein changes in the vortex ring structure are slow and predominantly due to viscous diffusion.

In experiments, the dynamics of the vortex rings formed after the initial readjustment appears to be independent of the different techniques used to generate them. In this report, numerical simulations are used to study the issue of whether the structure of the equilibrium vortex ring formed after the initial readjustment depends upon the initial vorticity profile. Additionally the issue of the continuation of the common equilibrium state, if it exists, up to large times is investigated.

1.2 Oblique interaction of vortex ring with free surface

Research in understanding the interaction of a vorticity field with a free surface is relevant to a variety of geophysical flows. One area of particular importance is the interaction of the wakes of partially or completely submerged moving bodies with a free surface. The aspect of this interaction focussed upon in the present study is the phenomenon of vortex reconnection wherein the vortex filaments at a free surface disconnect from themselves and connect with the surface. Apart from the interaction of vortices with a free surface the vortex reconnection phenomenon also occurs when a pair of vortex rings or line vortices undergo a collision leading to disconnection and reconnection with each other resulting in a linked pair. A couple of examples of geophysical flows where vortex reconnection occurs are (i) the vortex ring emitted by a submarine performing a diving manoeuvre which travels towards the surface and collides with it and (ii) the collision of the growing sinusoidal perturbations of a vortex pair in the wake of an aircraft undergoing a Crow instability. Vortex reconnection has been studied in these various contexts through experiments and numerical simulations.

The key non-dimensional parameters which characterise a vortex ring – surface interaction are the Reynolds number and the Froude number. The Reynolds number is defined as the ratio between the initial circulation of the ring and the kinematic viscosity (Γ_0/ν). The Froude number is defined using the initial circulation, initial radius of the ring and the acceleration due to gravity as $\Gamma_0/(gR_0^3)^{1/2}$ and is a measure of the displacement amplitude of the surface. In the present work, interactions in the limit of zero Froude number viz. interactions of a vortex ring with a non-deformable, free-slip surface are considered. Specifically vortex reconnection occurring due to the impingement of a vortex ring on a non-deformable, free-slip surface at an oblique angle of incidence is investigated. This problem is equivalent to an oblique-angle collision of two vortex rings with the interaction plane coinciding with the surface. As the vortex ring impinges upon the surface, vortex filaments in the interaction region are disconnected via viscous diffusion

towards the surface (or equivalently diffusion towards the oppositely-signed image vortex filaments) and thereby link normally with the disconnected image filaments across the surface.

The primary focus of this study is the effect of the Reynolds number on the reconnection. The scaling of the rate of the reconnection process (characterised by a reconnection time T_R) with Re is obtained. An instability occurring during reconnection at high Re is identified and explained in light of the effect of Reynolds number on the reconnection process. A new phenomenon is presented wherein the reconnection of a vortex ring with a free-slip surface at a high Reynolds number leads to a breakdown of the entire vortex ring structure to a turbulent-like flow.

1.3 Vortex rings with swirl

A vortex ring with swirl consists of an axisymmetric, compact distribution of azimuthal vorticity with non-zero azimuthal velocity. While classical vortex rings have been analysed extensively over decades, vortex rings with swirl have not been studied in great detail. The existence of inviscid, steady solutions for vortex rings with swirl have been shown by Moffatt (1988) and Turkington (1986). In this report the properties of vortex rings initialised with swirl in viscous, unbounded flow were studied. The issue of whether a limit exists for the maximum amount of swirl on a vortex ring is investigated.

The non-swirling vortex ring is known to be unstable to azimuthal perturbations which lead to the Widnall instability (Widnall et al., 1974). In this work a helical instability occurring in vortex rings due to swirl at high Reynolds numbers is introduced. A method for identifying the modal structure of the helical instability is presented and the dependence of one of the instability modes on the geometric properties of the vortex ring is shown.

The thesis is organised into the following chapters. In Chapter 2, a review of the literature relevant to the three aspects of vortex ring dynamics discussed in this report is presented. The numerical method and approach used in the DNS computations of vortex ring dynamics is described in Chapter 3. In Chapters 4, 5, 6, 7 and 8 the results of the study of (i) Classical vortex rings in unbounded flow (Chapter 4) (ii) The interaction of a vortex ring with a free-slip surface leading to the phenomenon of vortex reconnection (Chapters 5 and 6) and (iii) Vortex rings with swirl in unbounded flow (Chapters 7 and 8) are presented and discussed. A summary of all the findings and suggestions for future work are provided in Chapter 9.

Chapter 2

Literature Review

The vortex ring is defined in section 2.1. The reviews of the literature relevant to the main topics of investigation in this report are presented in sections 2.2, 2.3 and 2.4.

2.1 Definitions

A vortex ring is a bounded, toroidal distribution of vorticity. The bounded region of vorticity is referred to as the core of the vortex ring. The vortex ring is represented in a cylindrical coordinate system (r, θ, z) with its origin at the centre of the vortex ring (as shown in 2.1) and translating along with the ring. The axis of the vortex ring is aligned with the z-axis. The components of the velocity and vorticity fields are (u_r, u_θ, u_z) and $(\omega_r, \omega_\theta, \omega_z)$ respectively.

The radius of the vortex ring, R, is the distance between the center of the ring and the centre of the core. The core radius, δ, is the radius of the toroid. The ratio of the core radius to the ring radius is the slenderness ratio, ϵ. The exact mathematical definitions of R and δ are introduced in section 4.2. The vortex ring has a circulation, Γ defined as

$$\Gamma = \iint \omega_\theta dr dz$$

with the integration performed on a radial plane. An axisymmetric vortex ring is defined by the circulation, ring radius, core radius and the shape of the vorticity distribution within the vortex core.

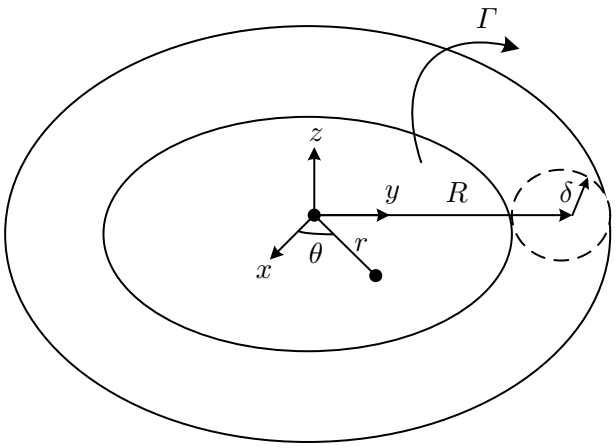

Figure 2.1: Schematic of a vortex ring.

2.2 Classical vortex rings without swirl

2.2.1 Inviscid dynamics

The equation for azimuthal vorticity in axisymmetric, inviscid flow is given by

$$\frac{D(\omega_\theta/r)}{Dt} = 0$$

(Batchelor, 1967) where D/Dt is the material derivative. For steady flow,

$$\frac{\omega_\theta}{r} = g(\psi) \tag{2.1}$$

where g is an arbitrary function and ψ is the Stokes streamfunction with

$$u_r = -\frac{1}{r}\frac{\partial \psi}{\partial z},\ u_z = \frac{1}{r}\frac{\partial \psi}{\partial r}$$

For $g(\psi)$ =constant, Norbury (1973) computed a solution family of vortex rings ranging from thin-cored vortex rings to the Hill's spherical vortex.

Helmholtz (1858) derived the following expression for the self-induced propagation velocity of a vortex ring

$$U = \frac{\Gamma}{4\pi R}\left[\log\left(\frac{8R}{\delta}\right) + C\right] \tag{2.2}$$

Kelvin (1867) determined the value of the constant, C to be -0.25 for a thin, steady vortex ring in inviscid flow.

2.2.2 Vortex rings in viscous flow

Saffman (1970) generalised the equation for the propagation velocity by deriving an expression for the translation parameter C for an arbitrary vorticity profile within the core. Saffman (1970) assumed a Gaussian distribution of vorticity within the vortex ring core for a thin cored vortex ring in viscous flow given by

$$\omega_\theta(\rho) = \frac{\Gamma_0}{\pi\delta^2} \exp\left(-\rho^2/\delta^2\right) \tag{2.3}$$

and showed that its propagation velocity is given by

$$U = \frac{\Gamma}{4\pi R}\left[\log\left(\frac{8R}{\delta}\right) - 0.558 + \mathcal{O}(\epsilon \log \epsilon)\right] \tag{2.4}$$

Stanaway et al. (1988) performed Navier-Stokes simulations of laminar vortex rings initialised with a Gaussian core and found that the propagation velocity with $C = -0.558$ was accurate to within an error of the order of $\epsilon^2 \log \epsilon$.

Stanaway et al. (1988) observed that for a thick-cored vortex ring, the initially circular core underwent a readjustment to an elliptical shape (figure 2.2). An experimental study of vortex ring formation and subsequent evolution was performed by Dabiri and Gharib (2004). The core of the post-formation vortex ring visualised using digital particle image velocimetry (DPIV) was also found to be elongated along the axial direction and non-symmetric along the radial direction. Archer et al. (2008) performed direct numerical simulation of Gaussian initialised vortex rings and found that the amount of vorticity shed into the wake during the initial readjustment and the skewness of the vorticity distribution of the readjusted vortex ring increased with the initial slenderness ratio.

The vortex ring is surrounded by a co-moving mass of rotational fluid known as an entrainment bubble. As the vortex ring propagates, irrotational fluid is entrained into the bubble. Additionally the vortex ring also sheds fluid with vorticity into a trailing wake. Therefore the vortex ring properties such as impulse, circulation, radius etc... vary with time. Archer et al. (2008) calculated the velocity of the vortex rings and determined the value of the translational parameter C according to (2.2) using the instantaneous values of circulation, ring radius and core radius. They showed that the plots of C vs. ϵ for Gaussian initialised vortex rings with different initial slenderness ratios and at differing Reynolds numbers, converged to a common curve after the initial readjustment (figure 2.3), represented by

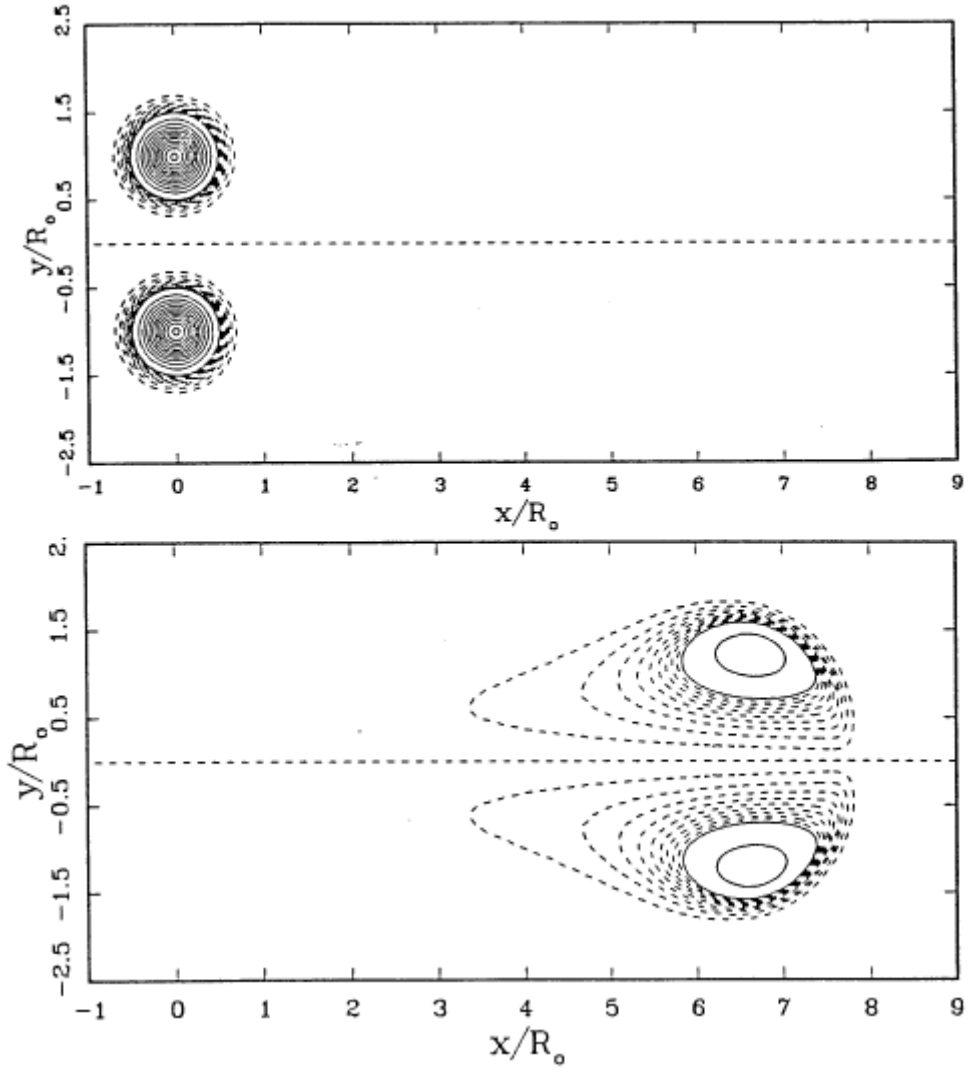

Figure 2.2: Contours of azimuthal vorticity from Stanaway et al. (1988) showing the skewed vorticity profile of a vortex ring after the initial readjustment.

$$C = -1.12\epsilon^2 - 5.0\epsilon^4 - 0.558.$$

The equation is asymptotic in the thin core limit of $\epsilon \to 0$ to the value for a Gaussian profile of -0.558. Since C is a function of the shape of the core vorticity profile, this showed that the Gaussian initialised vortex rings readjusted to a common equilibrium state in which the shape of the core vorticity profile was dependent only on the slenderness ratio.

2.2.3 Large time behaviour of vortex rings in viscous flow

Kambe and Oshima (1975) found that the propagation velocity of vortex rings at large

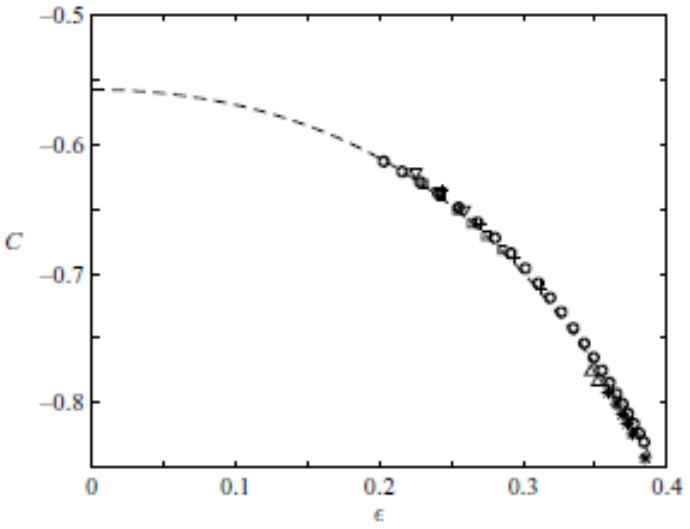

Figure 2.3: Translational parameter C vs. ϵ from Archer et al. (2008),- - - - $C = -1.12\epsilon^2 - 5\epsilon^4 - 0.558$, the symbols correspond to Gaussian initialised vortex rings with different initial slenderness ratios and different Reynolds numbers after their initial readjustment.

times in experiments decayed as $t^{-1.5}$. Cantwell and Rott (1988) provided an analytical solution for the asymptotic drift velocity as $t \to \infty$ dependent only on the initial impulse of the vortex ring I and the kinematic viscosity of the fluid:

$$\begin{aligned} U &= k\frac{I}{\rho}(\nu t)^{-1.5} \\ k &= 3.7038 \times 10^{-3} \end{aligned}$$

The asymptotic state corresponds to a slowly decaying, self-similar, fat vortex ring governed by the Stokes equations. Stanaway et al. (1988) used Stokes dipoles as the initial condition in their numerical simulations and verified the asymptotic drift velocity given by Cantwell and Rott (1988) obtaining an excellent match for the value of the proportionality constant k.

Weigand and Gharib (1997) generated vortex rings in a water tank using a piston-cylinder mechanism at different Reynolds numbers and tracked their propagation velocities from their formation up to large times. The measured propagation velocities were in good agreement with the data from the numerical simulations of Stanaway et al. (1988). They also showed that at large times, the propagation velocity approached the exact asymptotic solution for the drift velocity given by Cantwell and Rott (1988).

2.3 Vortex ring reconnection with a non-deformable, free-slip surface

2.3.1 Vortex ring and vortex pair collision

2.3.1.1 Experimental studies

The earliest experimental studies of vortex ring collisions (Kambe and Takao, 1971; Fohl and Turner, 1975; Oshima and Asaka, 1975, 1977) used flow-visualization techniques with smoke (in air) and dye (in water) to mark the rings. The Reynolds number for these experimental studies was defined based on the diameter and the initial velocity of the vortex rings. Oshima and Asaka (1975) used a water tank apparatus to simultaneously generate a pair of vortex rings travelling along parallel axes in the same direction at a Reynolds number of 400. The inner portions of the rings, under mutual induction, were decelerated and the rings turned towards each other. As the ring cores with oppositely signed vorticity came into contact the vortex filaments got delinked and cross-linked with the respective filaments from the other ring. Thus a new deformed ring was formed with halves of its fluid material from both the original rings. This was visualised by using differently coloured dyes for the two rings (figure 2.4). The newly connected ends moved away from each other and the outer portions of the ring began to approach the collision plane. If the rings were initially imparted an impulse higher than a particular level, the outer portions also came into contact and the filaments de-linked and cross-linked again creating two separate rings each consisting of fluid material from both the original rings. If the initial impulse was lower the deformed ring underwent oscillations similar to an elliptic vortex ring with the major and minor axes switching with each other in addition to an out of plane distortion. Kambe and Takao (1971) had also reported this 'fusion' and subsequent 'fission' phenomenon using smoke vortex rings. They had also observed a similar dependence of the second reconnection on the initial impulse.

Fohl and Turner (1975) studied the motion of the distorted vortex ring formed from the merging of two colliding vortex rings as the $n = 2$ mode of free vibration of a circular ring. They proposed that the condition for the merged ring to further split up was that the component of the velocity of the approaching vortex rings towards the collision plane had to be comparable to the maximum transverse velocity of the oscillations of the filaments of the distorted vortex ring. This gave a condition of the half-angle between the initial trajectories of the rings to be roughly 16° above which successive reconnections occurred in almost all the cases. This was supported by experiments of vortex ring collisions at a Reynolds number of 4000 studying the percentage of collisions leading to two successive reconnections at varying angles of approach. Oshima and Asaka (1977) however, demonstrated that even parallel vortex rings undergo reconnection and suggested that the low percentage in the case of Fohl and Turner might be due to low

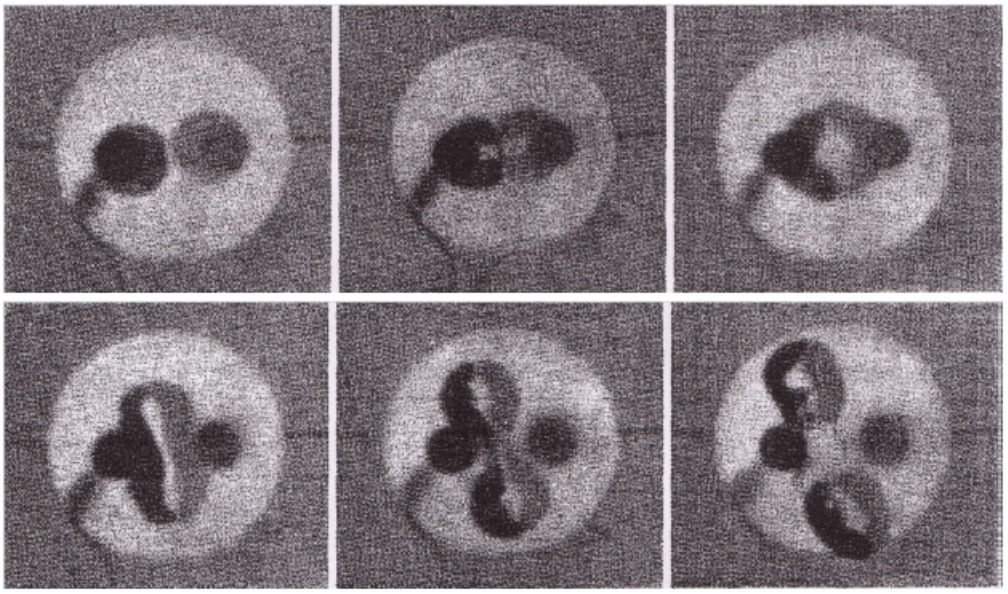

Figure 2.4: Series of photographs from Oshima and Asaka (1975) of the first (top) and second (bottom) reconnection events during a collision of two vortex rings visualised using different dyes

reproducibility and inaccuracy in vortex formation at high Reynolds numbers due to the high initial speeds involved. In their experiments, they varied the Reynolds number by modifying the initial speed. They found that for $Re < 230$ there was no reconnection, for $230 < Re < 300$ a single reconnection event occurred, for $300 < Re < 420$ two reconnection events occurred and for $420 < Re < 650$ the two rings formed by the previous reconnections once again underwent a third reconnection to yield a deformed ring which oscillated and diffused away. Greater initial velocities resulted in an initially turbulent ring which diffused away before any reconnection.

Oshima and Asaka also studied the variation of the time up to the first reconnection which showed an exponential variation with Reynolds number. Kida et al. (1989) pointed out that the change in topology of a passive scalar used to mark the flow such as smoke or dye would not necessarily track the changes in the vorticity field. While vorticity magnitude intensifies when vortex lines undergo stretching, scalar markers would decrease in density.

Experimental studies involving quantitative measurements of the flow-field were carried out by Oshima and Izutsu (1988) and Izutsu and Oshima (1991) using hot-wire anemometry and Schatzle (1987) using Laser Doppler velocimetry. Schatzle plotted (see figure 2.5 for their initial configuration) contour maps of, apart from vorticity, velocity gradients on the symmetry plane as the vortex rings interacted. The vortex cores upon collision were observed to be stretched and flattened into a shape with an elongated tail referred to as a 'head-tail' structure (figure 2.6). During this process, the out-of-plane strain $\partial v/\partial y$ (where the symmetry plane is defined by $y = 0$) was observed to be

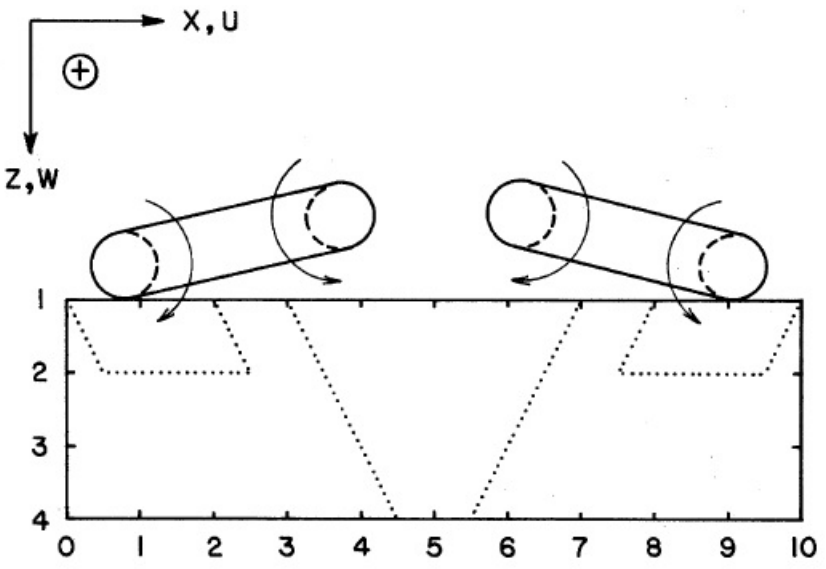

Figure 2.5: Schematic from Schatzle (1987) showing the flow configuration

significantly large in the region. The in-plane strain $\partial u/\partial x$ was negative implying the compression of the fluid between the two cores.

Schatzle observed that the reconnection process occurred over a timescale much smaller than would be predicted by a purely viscous cancellation process. He proposed the following sequence of events emphasizing the role played by the out-of-plane strain which was observed to increase simultaneous with the reconnection process. Initially as the two rings approach each other along their axes, the in-plane strains ($\partial u/\partial x$ and $\partial w/\partial z$) are oppositely signed with the fluid being compressed laterally between the two cores (in the x-direction) and stretched along the z-axis direction. As the oppositely signed vortex filaments from the two rings come into contact, cancel out each other and reconnect, they induce a flow opposite to that due to the unconnected filaments in the z-direction. Now both the in-plane velocity gradients are negative contributing to the growth of the out-of-plane strain ($\partial v/\partial y$) which stretches the vortex filaments and thereby increases the vorticity gradient across the vortex cores which aids the cancellation of vorticity by viscosity.

Based on the importance of viscosity and the strain rate, Schatzle considered two expressions for the reconnection time: $T_R \sim d/(\alpha\nu)$ and $T_R \sim d^2/(\Gamma\nu)^{1/2}$ where d is the diameter of the vortex cores and α is an average measure of the out-of-plane strain rate during the connection process. Also based on a one-dimensional model he derived another expression for the reconnection time: $T_R \sim (1/2\epsilon)\log(d^2\epsilon'/\nu)$ where ϵ' is the in-plane strain. His measurements were insufficient to decide between the timescales.

Oshima and Izutsu (1988) plotted the vorticity isosurfaces and the variation of circulation on both the symmetry and collision planes and showed the simultaneous depletion of vorticity on the symmetry plane and appearance of new cross-links on the collision

Figure 2.6: Head-Tail structure from Kida et al. (1991) vorticity contours on the symmetry plane. Solid and broken lines represent vorticity of opposite signs

plane. They identified that the disconnection and reconnection did not occur at one location or instantaneously but rather gradually with the vortex cores depleting over a finite time. The new cross-links coalesced to form two 'bridges' which then moved apart owing to their strong curvature.

2.3.1.2 Numerical simulations

Melander and Hussain (1989) performed a direct numerical simulation of reconnection of an anti-parallel vortex pair at a Reynolds number (Γ_0/ν) of 1000 using a pseudo-spectral method. The vortex pair were initialised with a sinusoidal perturbation which grew and brought the vortices into contact initiating the vortex reconnection process. They proposed a bridging mechanism for the reconnection process (described below).

Kida et al. (1991) performed a numerical simulation of the collision of two vortex rings at an oblique angle using a spectral method on a grid with 64^3 points. The rings were initialised with a Gaussian distribution of vorticity in the cores and aligned along axes subtending an angle 2θ between them. Simulations were performed for varying values of Re and θ. Plotting the vorticity contours on the symmetry and collision planes, they outlined the deformation of the vortex cores upon collision into dipole-like structures with a head containing the vorticity peak and an elongated tail (figure 2.6).

The interaction process was described in terms of the 'bridging' mechanism proposed by Melander and Hussain (1989) involving three phases:

1. An inviscid advection phase wherein, due to the induced velocity field of the vortex rings, the rings tilt towards each other and come into contact stretching and flattening their respective cores into a head-tail structure (figure 2.6) which advects towards the direction of the head.

2. A bridging phase involving the mutual cancellation of oppositely signed vortex filaments through viscous diffusion and simultaneous reconnection along the normal

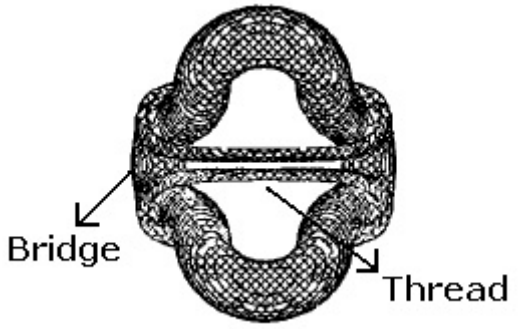

Figure 2.7: Vorticity iso-surface from Kida et al. (1991) illustrating the bridges and threads formed during vortex reconnection

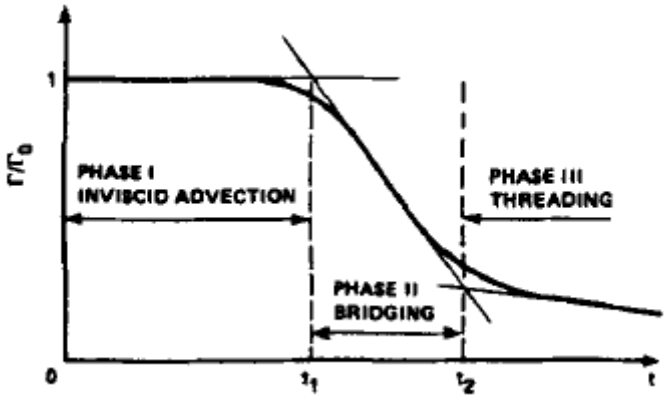

Figure 2.8: History of circulation of interacting vortex core during the different phases of reconnection from Melander and Hussain (1989).

to the collision plane at the site of two 'bridges' (figure 2.7). The circulation is transferred from the initial direction to the orthogonal direction (figure 2.8).

3. A threading phase involving the movement of the unconnected vortex filaments, termed 'threads' (figure 2.7) away from each other and the termination of the reconnection process before completion. The incompleteness of the reconnection was attributed to the reversal of curvature of the threads due to the induced velocity of the bridges and the non-interacting parts of the vortex rings. The self-induced velocity of the threads after the curvature reversal would lead their separation to increase slowing the rate of reconnection. As a consequence of this mechanism it was predicted that an entanglement of vortex lines would occur close to the bridges due to both the reconnected and uncancelled vortex lines rotating about the vortex core.

The history of the circulation of the interacting vortex core during these three phases is shown in figure 2.8.

A second reconnection occurred as observed in experiments with the previously non-interacting ends of the rings approaching each other. The mechanism was seen to be similar to the first reconnection. The rate of decline of the circulation of the vortex core was found to be slower than during the first reconnection. Also the reconnection process left behind a greater amount of uncancelled vorticity than in the first. These were attributed to the absence of a background flow pushing the vortex cores together as was present in the case of the first reconnection as a result of the non-interacting parts of the vortex rings.

From the kinetic energy, dissipation rate and enstrophy fields the regions where high energy dissipation prevailed were found to be very localized, occurring predominantly at the interaction zone, the bridges and the threads. Tracking the time evolution of a passive scalar, they demonstrated that the iso-surfaces of scalar markers and vorticity magnitude do not develop in the same way. This had implications for using smoke, dye visualisation to study quantitative aspects such as the reconnection time.

Chen (1991) performed direct numerical simulations of vortex ring collisions at varying Reynolds numbers. The vortex rings were initialised by simulating the ejection of fluid through circular openings (the generation process for vortex rings used in experiments). The core deformation due to the interaction was found to be minimal for the low Reynolds number simulation. The maximum dissipation rate in the flow field increased with time when the reconnection began attaining a peak value (figure 2.9) before decreasing. The peak value was found to increase with Reynolds number. The dissipation process was hence identified to be critical to the reconnection process. Chen reasoned that reconnection would occur even in the limit of $\nu \to 0$ since the energy dissipation rate ($2\nu\epsilon$ where ϵ is the square of the strain-rate tensor) would remain finite since ϵ would tend to infinity.

All the studies in the literature investigating the scaling of reconnection time with Re pertain to the reconnection of anti-parallel vortex pair.

Shelley et al. (1993) used a pseudo-spectral method on a uniform grid to simulate the interaction of two perturbed counter-rotating vortex tubes at Reynolds numbers varying from 500 to 1500. An adaptive spectral method on a stretched grid was used to perform the simulation at higher Reynolds numbers (1500 to 3500). The vortices collided and were flattened against each other. The vortex stretching process began as the regions of high vorticity and strain rate on the symmetry plane became aligned. The cores were flattened into ribbons along the length of which the viscous dissipation was strong. The flattening of the vortex core during reconnection increased with Reynolds number. The vorticity maximum attained during the reconnection increased with Reynolds number and at $\mathrm{Re} = 3500$, the vorticity was found to stretch to nearly seven times its initial value (figure 2.10). The reconnection time, defined as the time to halve the circulation on the

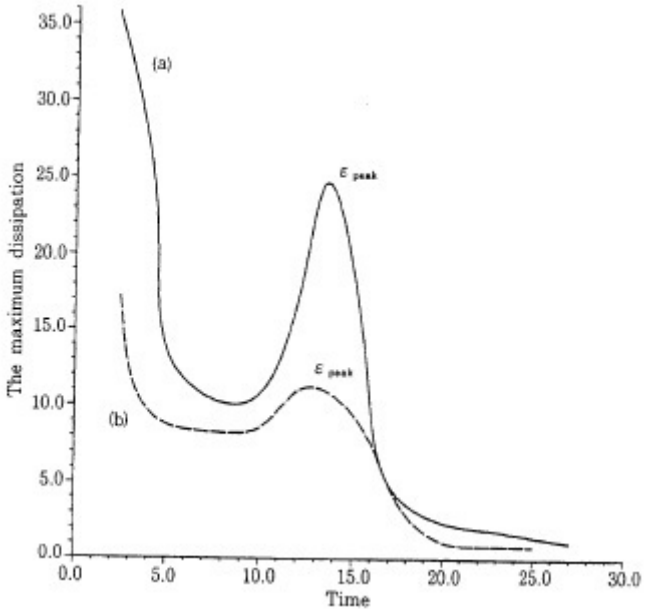

Figure 2.9: Maximum energy dissipation rate vs. Time at Reynolds numbers of a) 1000 b) 600 from Chen (1991)

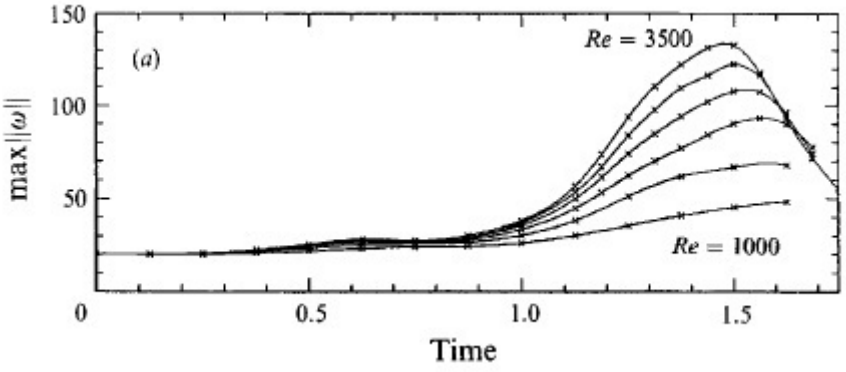

Figure 2.10: Vorticity maximum on the symmetry plane for Re = 1000, 1500, 2000, 2500, 3000 and 3500 from Shelley et al. (1993)

symmetry plane, was found to vary with Reynolds number slower than a logarithmic variation.

Garten et al. (2001) performed a direct numerical simulation of a vortex pair undergoing the Crow instability and subsequent vortex reconnection in stratified and unstratified fluid at varying Reynolds numbers. The reconnection time, defined as the inverse of the rate of decay of the circulation of the interacting vortex core when the circulation decreases to half its initial value, decreased with increasing Reynolds number as $1/Re$. Melander and Hussain (1989) had attributed the incompleteness of the reconnection to the curvature reversal of the threads due to the induced velocity of the bridges and the consequent self-induced velocity away from the collision plane. Garten et al. (2001)

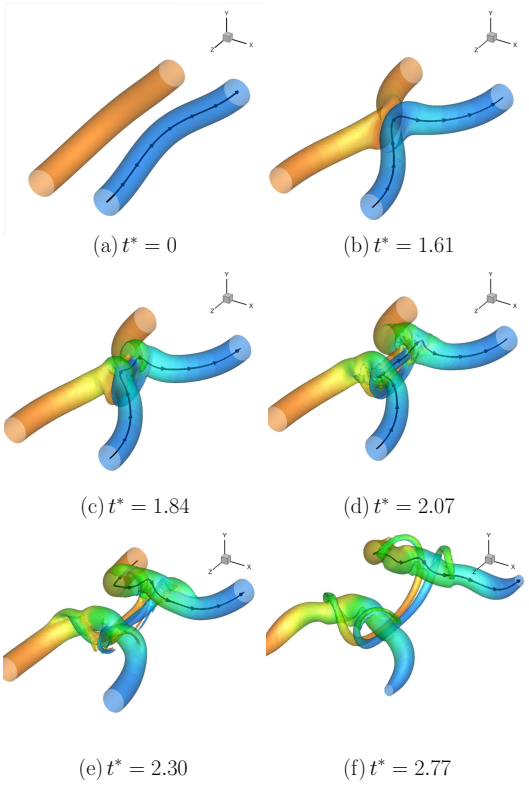

(a) $t^* = 0$ (b) $t^* = 1.61$

(c) $t^* = 1.84$ (d) $t^* = 2.07$

(e) $t^* = 2.30$ (f) $t^* = 2.77$

Figure 2.11: Vorticity magnitude isosurfaces showing typical reconnection of an anti-parallel vortex pair at $Re = 2000$ from Hussain and Duraisamy (2011).

found that the curvature reduced without undergoing a complete reversal. Apart from the curvature reduction they showed that viscous diffusion also played an important part in increasing the thread separation during the late stages of reconnection.

Hussain and Duraisamy (2011) performed direct numerical simulation of the reconnection of an anti-parallel pair using a pseudospectral method for Reynolds numbers ranging from 250 to 9000.

They reported that the maximum rate of change of circulation scaled as Re^n with $n = 1.0$. At high Reynolds numbers they found that the vortex core was flattened into a vortex sheet. The 'head' of the vortex sheet split away from the remaining part. This was attributed to a Kelvin-Helmholtz instability. The reconnection at high Reynolds numbers was also accompanied by the appearance of anti-symmetric features and found to lead to a rapid development of small scale structures (figure 2.12).

Rees et al. (2012) performed a simulation of a reconnecting vortex pair at a Reynolds number of 10000. The energy spectrum during the reconnection of two vortex tubes without axial flow was shown to follow a slope of -5/3. A subsequent second reconnection due to the reconnection of the oscillating elliptic vortex ring formed at the end of the first reconnection had an energy spectrum with a -7/3 slope. As in the case of Hussain

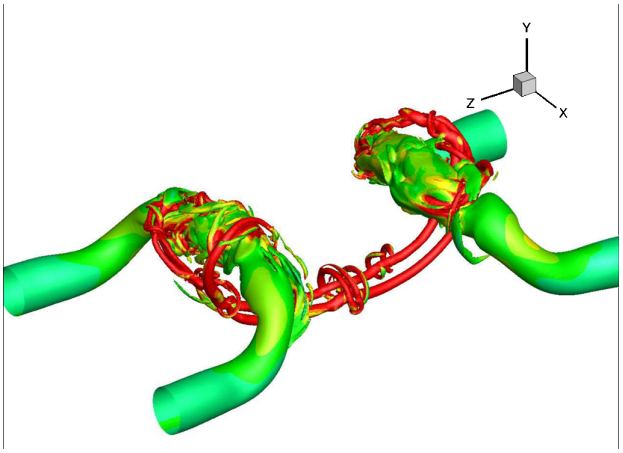

Figure 2.12: Vorticity magnitude isosurfaces showing development of small-scale features during reconnection of an anti-parallel vortex pair at $Re = 7500$ from Hussain and Duraisamy (2011).

and Duraisamy (2011), they also found a rapid generation of small-scale structure along with the reconnection at high Re (figure 2.13).

2.3.1.3 Analytical models for vortex pair reconnection

Shelley et al. (1993) discussed some analytical models proposed for vortex pair reconnection and performed a numerical simulation of the reconnection of two anti-parallel vortex tubes to assess these models. Pumir and Siggia (1987) modelled the vortex reconnection phenomenon in inviscid Euler flow using vortex filaments to represent the vorticity field. The core of the vortex filaments was constrained to be circular throughout the interaction. Also the model did not take into account the effect of axial flows along the vortex tube. Shelley et al. (1993) showed that the Siggia-Pumir model, if viscous effects are included leads to a variation of reconnection time (defined as the time taken for the circulation on the symmetry plane to be halved) with Reynolds number as $T_R = t_* + O(1/Re)$ where t_* is the singularity time in the inviscid case.

Kambe (1983) had modelled the reconnection of two vortex layers under the influence of an in-plane two-dimensional strain and obtained the reconnection time to be $T_R \sim \log(Re/2\alpha)$ where α is the strain rate in the limit of large Reynolds numbers. Buntine and Pullin (1989) modified Kambes model by specifying an out-of-plane strain. However the strain rate was not affected by the evolution of the vorticity field and the same timescale for the reconnection time as Kambe was obtained.

Saffman (1990) proposed an analytical model consisting of a set of equations describing the time evolution of the circulation, core deformation, distance between the interacting cores and the velocity component normal to the symmetry plane (involving the out-of-plane pressure gradient). Based on the model, Saffman presented a couple of timescales

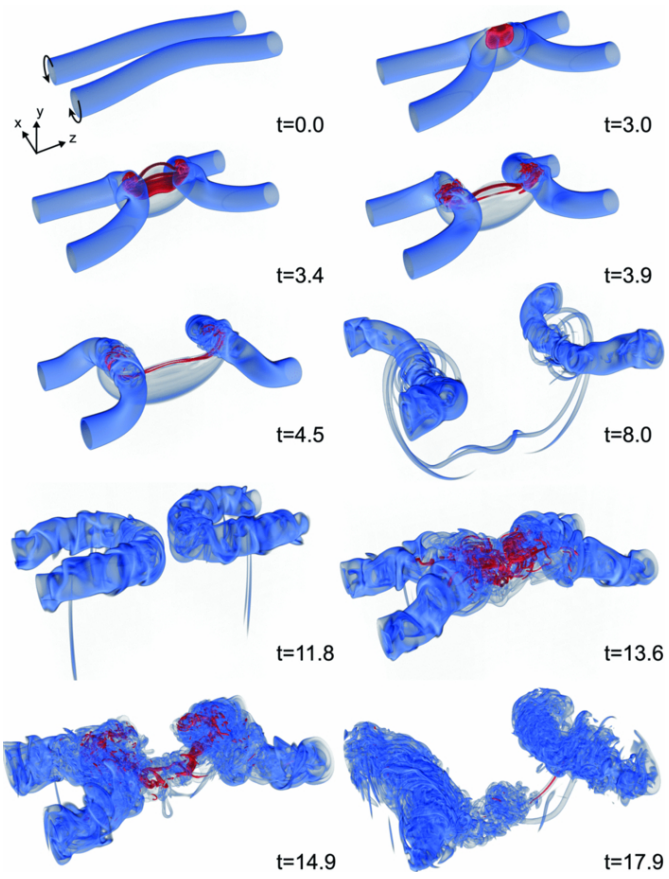

Figure 2.13: Vorticity isosurfaces (at two levels) from Rees et al. (2012) showing generation of small scale structures during vortex reconnection at Re=10000.

for the duration of the reconnection process. Shelley et al. computed the numerical solution of Saffmans model and showed that it predicts an increase of the reconnection time with the Reynolds number according to $t_R \sim \log(Re/2\alpha)$.

2.3.2 Vortex ring reconnection with a deformable free surface

A free surface boundary is characterised by zero tangential stress and constant pressure along the surface. An interface where the density and viscosity of one of the fluids is negligible compared to that of the other fluid (as in the case of a water-air interface) can hence be approximated as a free surface. A deformable free surface introduces additional dynamics. Unlike a flat surface, surface parallel vorticity can exist over a deformable surface.

Experimental studies of vortex ring reconnection with a free surface have been performed by Bernal and Kwon (1989), Weigand and Gharib (1995) and Gharib and Weigand (1996). As the vortex ring approaches a free surface surface, it induces a changing velocity field at the surface. The surface gains elevation appropriate to the velocity and

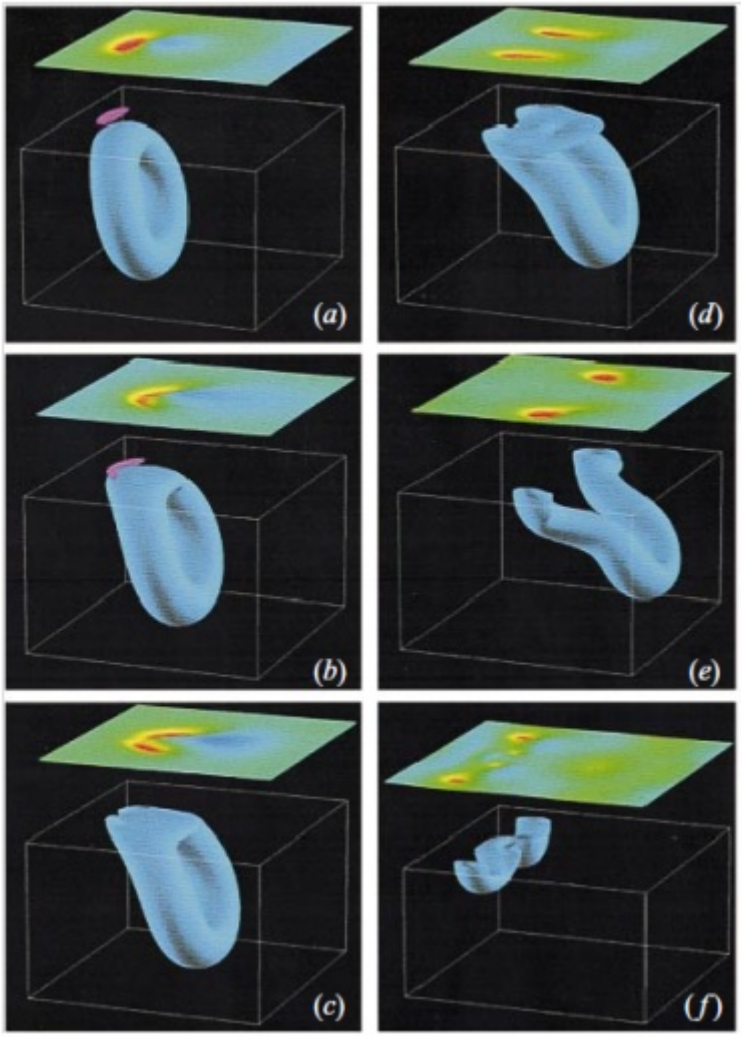

Figure 2.14: Vortex ring reconnection with a linearised free surface from Zhang et al. (1999).

acceleration (at each point on the surface). The curvature and the tangential variation of the surface normal velocity lead to regions of positive and negative vorticity (same as the upper tip of the vortex ring). The negative vorticity rolls up to form a secondary vortex. The secondary vortex interacts with the primary vortex and influences the reconnection process.

Zhang et al. (1999) performed a direct numerical simulation of an oblique vortex ring interacting with a deformable surface. They used linearised free-surface boundary conditions assuming small free-surface elevation. The different stages of the reconnection of the vortex ring with the linearised free surface are shown in figure 2.14.

To explain the mechanism of vortex connection they presented a model of two layers below the surface: An inner viscous layer immediately below the surface and an outer blockage layer. The blockage layer facilitates the variation of the flow velocities to satisfy

the kinematic boundary condition at the free surface. Its thickness is dependent on the flow length scale. The viscous layer facilitates the dynamics stress boundary conditions at the surface by the viscous effects. Hence, its thickness is dependent on the Reynolds number.

During the surface connection period it was found that the blockage layer involved mainly vortex stretching and tilting wherein the surface parallel vorticity was converted into surface normal vorticity. This reached a maximum at the inner edge of blockage layer and diminished within the viscous layer. Within the viscous layer, vorticity diffusion caused flux of the surface parallel vorticity to the surface and transport of surface normal vorticity towards the surface.

2.4 Vortex rings with swirl

Vortex rings with swirl or angular momentum have not been investigated as extensively as classical vortex rings. The earliest literature on vortex rings with swirl is concerned with the existence of axisymmetric, steady solutions to the Euler equations.

The Euler equations for axisymmetric, inviscid, incompressible flow with non-zero azimuthal velocity can be expressed in terms of the Stokes streamfunction (Batchelor, 1967) as

$$ru_\theta = f(\psi) \tag{2.5}$$

$$\frac{\omega_\theta}{r} = -h'(\psi) + \frac{f(\psi)f'(\psi)}{r^2} \tag{2.6}$$

$$\text{where } h(\psi) = \frac{p}{\rho} + \frac{1}{2}(u_r^2 + u_\theta^2 + u_z^2).$$

f and h are arbitrary functions of the streamfunction. In vortex rings without swirl a streamline is confined to a radial plane. In the presence of swirl, the streamlines are helical.

Turkington (1986) showed the existence of steady solutions using a variational method. The solution is a two-parameter family of vortex rings. One parameter specifies the swirl with the extreme cases of a vortex ring without swirl and a Beltrami vortex ring in which the vorticity field is parallel to the velocity field everywhere in the flow. The other parameter specifies the size of the cross-section of the vortex ring with the extreme cases of a thin cored vortex ring and a spherical vortex ring. Moffatt (1988) used an analogy between the Euler equations and the equations governing magnetostatic equilibrium in a

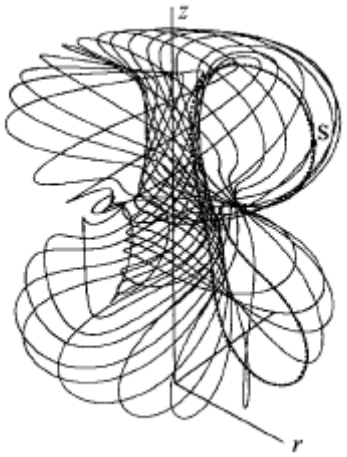

Figure 2.15: Vortex line geometry of a polarized vortex ring from Virk et al. (1994).

viscous perfectly conducting fluid and obtained the exact solutions of the Euler equations using a method of magnetic relaxation.

Eydeland and Turkington (1988) presented an iterative, numerical method to obtain the exact solutions found by Turkington (1986). Lifschitz et al. (1996) eliminated the requirement for a large computational domain in this method by using non-reflective boundary conditions ensuring smooth variation of the computed streamfunction at the boundary. They performed a short-wavelength analysis and predicted the growth rates of localised instabilities. They also used a three-dimensional vortex particle method to perform Euler simulations with perturbed vortex rings and compared the observed growth rates with the predictions.

Virk et al. (1994) performed axisymmetric Navier-Stokes simulations of initially polarized isolated viscous vortex rings containing swirl using helical wave decomposition (HWD). They described the coupling of the swirl and meridional flow and showed that it lead to destruction of azimuthal vorticity in the front of the ring (as defined by the propagation direction) and generation in the rear. They found that the polarized vortex ring developed an axial vortex on the axis of symmetry. Figure 2.15 shows the vortex line geometry after the development of the axial vortex. They also found that the propagation velocity of the vortex ring decreased with increasing polarization.

Hu et al. (2001) performed Navier-Stokes simulations of vortex rings with swirl using exact solutions of the steady Euler equations obtained using the method of Lifschitz et al. (1996) as the initial condition. They introduced azimuthal perturbations and studied their growth. The azimuthal perturbation modes initially grew linearly and two bands of growing waves were observed.

Cheng et al. (2010) used a Lattice Boltzmann method to study vortex rings with swirl in viscous fluid. They initialised the vortex rings with a Gaussian distribution of azimuthal vorticity and an additional swirl velocity profile. Due to swirl, the vortex ring developed a region of negative azimuthal vorticity. At high swirl, the negative azimuthal vorticity rolled up to form a secondary vortex ring. The secondary vortex ring interacted with the primary ring leading to intertwining vortex filaments (figure 2.16).

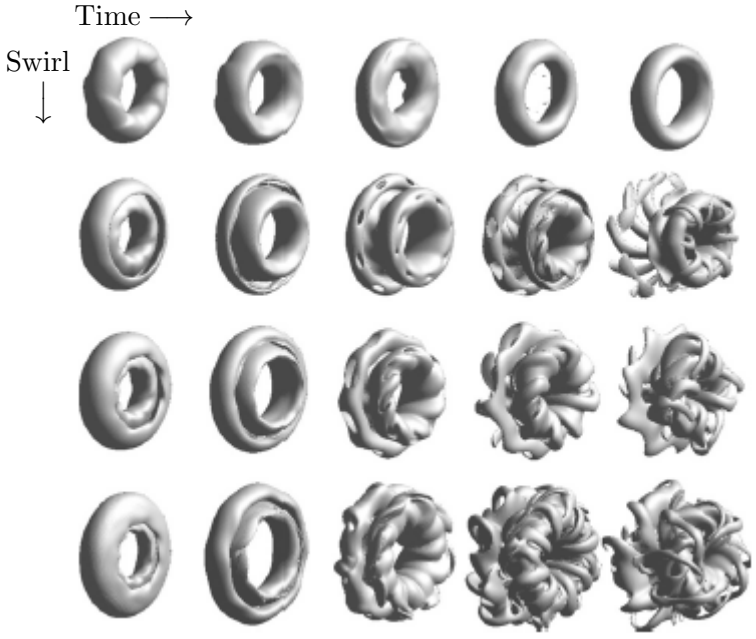

Figure 2.16: Evolution of vortex rings with swirl visualised using isosurfaces of vorticity from Cheng et al. (2010). Each row represents the evolution of a single vortex ring. The amount of initial swirl in the ring increases from the top row to the bottom.

Chapter 3

Numerical method

The direct numerical simulation (DNS) studies performed in this work utilised the parallelised finite-difference numerical solver CGLES. The code has been written in C/C++ and uses Message Passing Interface (MPI) libraries to implement the parallelisation. It was initially used in large-eddy simulations (LES) and DNS of flow over complex geometries (Thomas and Williams (1997),Yao et al. (2001)). CGLES was recently used in DNS studies of vortex rings in unbounded fluid (Archer et al., 2008) and vortex ring collision with a free-slip, non-deformable surface (Archer et al., 2010).

The incompressible mass conservation equation and the incompressible, viscous Navier-Stokes momentum equations are solved in a Cartesian coordinate system.

$$\frac{\partial u_i}{\partial x_i} = 0 \tag{3.1}$$

$$\frac{\partial u_i}{\partial t} + u_j \frac{\partial u_i}{\partial x_j} = -\frac{1}{\rho}\frac{\partial p}{\partial x_i} + \nu \frac{\partial^2 u_i}{\partial x_j \partial x_j} \tag{3.2}$$

ρ and ν are the density and the kinematic viscosity of the fluid respectively. p is the kinematic pressure and $u_i = (u, v, w)$ is the fluid velocity at point $x_i = (x, y, z)$ at time t.

The code uses a staggered grid to implement a second-order central difference scheme for spatial discretisation conserving momentum and energy. The computational domain with $N_x \times N_y \times N_z$ uniformly spaced grid points is partitioned into N_b blocks with $n_x \times n_y \times n_z$ points in each block. The N_b blocks are mapped to $N_p \leq N_b$ processors. In addition to the points within its boundary, each block maintains an overlap region consisting of a layer of grid points extending beyond the block boundary. The message passing interface is used to transmit information about changes in the flow data within each block to the overlap regions of the neighbouring blocks.

The computation is initiated with an initial velocity field and the boundary conditions. The projection method and a second order, explicit Adams-Bashforth scheme is used for the time advancement. Using the velocity and pressure field data from the $(n-1)^{\text{th}}$ and n^{th} timesteps, the velocity field at the $(n+1)^{\text{th}}$ timestep is given by

$$u_i^{n+1} = u_i^n + \frac{3\Delta t}{2}\left(H_i^n - \frac{\partial p^n}{\partial x_i}\right) - \frac{\Delta t}{2}\left(H_i^{n-1} - \frac{\partial p^{n-1}}{\partial x_i}\right) \tag{3.3}$$

where Δt is the time step and H_i is defined as

$$H_i = -u_j\frac{\partial u_i}{\partial x_j} + \nu\frac{\partial^2 u_i}{\partial x_j \partial x_j}. \tag{3.4}$$

In the projection method, an intermediate velocity u_i^* is computed, neglecting the pressure gradient at the n^{th} timestep from (3.3).

$$u_i^* = u_i^n + \frac{3\Delta t}{2}H_i^n - \frac{\Delta t}{2}\left(H_i^{n-1} - \frac{\partial p^{n-1}}{\partial x_i}\right) \tag{3.5}$$

$$\implies u_i^{n+1} = u_i^* - \frac{3\Delta t}{2}\frac{\partial p^n}{\partial x_i} \tag{3.6}$$

By enforcing continuity (equation 3.1) at the $(n+1)^{\text{th}}$ timestep, a Poisson equation for the pressure at the n^{th} timestep is obtained.

$$\frac{\partial^2 p^n}{\partial x_i \partial x_i} = \frac{2}{3\Delta t}\frac{\partial u_i^*}{\partial x_i} \tag{3.7}$$

Finally after solving for the pressure field at the n^{th} timestep, the velocity field at the $(n+1)^{\text{th}}$ timestep is obtained from equation 3.6.

The Poisson equation for the pressure field is solved using a parallel, multigrid method. Within each block a hierarchy of grids with different mesh sizes is constructed by binary subdivision. Beginning from the finest grid with (n_x, n_y, n_z) gridpoints, each successive subdivision results in a coarser grid with half the number of grid points along each direction. The values of n_x, n_y and n_z are therefore chosen such that the number of possible subdivisions is maximised. At each level of subdivision, the grids have overlap regions and the message passing interface is used to transmit information about changes in the flow data.

The algorithm of the multigrid method consists of the following steps:

1. At the finest grid level, two iterations of the Gauss-Seidel method are performed and the residual of the Poisson equation is computed (Pre-Smoothing).

2. The residual is transferred to a coarser grid by a 'restriction' operator. The residual value at a gridpoint on the coarser grid is computed as a linear combination of the values of the residual at neighbouring gridpoints on the finer grid. Two iterations of the Gauss-Seidel method are performed at the coarser grid.

3. Step 2 is repeated until the coarsest grid level is reached. At the coarsest grid level, a Red-Black successive over-relaxation scheme is used to solve the Poisson equation. Iterations of the scheme are performed until the error norm is reduced below a defined tolerance level.

4. The corrected pressure field is transferred to the next finer grid level using a 'prolongation' operator which interpolates the values from the coarser grid level. Two iterations of the Gauss-Seidel method are performed at the finer grid (Post-Smoothing).

5. Step 4 is repeated until the finest grid level (the initial grid) is reached. Two final Gauss-Seidel iterations are performed at the initial grid level. If the error norm at the initial grid level is higher than a defined tolerance level, the entire cycle is repeated.

With a sufficiently high level of subdivision, the computational time spent at the coarsest grid level (step 3) is negligible compared to the time spent in performing the other steps.

The simulations in this report have been performed at Reynolds numbers of up to $\sim 10^4$ using up to $\sim 1.0 \times 10^9$ cells. The numerical code is highly parallelised and large-scale computations have been performed using up to 4096 processors. The simulations were run on the University of Southampton Iridis 3 cluster and HECToR, the UK's high-end computing resource.

Chapter 4

Classical vortex rings in unbounded flow

The velocity of a vortex ring given by (2.2)

$$U = \frac{\Gamma}{4\pi R}\left[\log\left(\frac{8R}{\delta}\right) + C\right],$$

provides a sensitive measure of the vortex core structure since the translation parameter C is purely a function of the shape of the core vorticity profile. Archer et al. (2008) used this property to show that Gaussian initialised vortex rings with different initial slenderness ratios and at different Reynolds numbers, after undergoing an initial adjustment, relaxed into a common equilibrium state. Using plots of the translation parameter against the slenderness ratio, they showed that this equilibrium state constitutes a single parameter family wherein the shape of the core vorticity profile is uniquely determined by the slenderness ratio.

In this chapter, a DNS study of classical vortex rings with a wide range of initial core azimuthal vorticity profiles is presented. They are shown to readjust to the common equilibrium state identified by Archer et al. (2008). The structure of the equilibrium state vortex rings is described. The issue of whether the common equilibrium state continues up to large times is also studied.

The numerical approach used for the simulations discussed in this chapter is outlined in section 4.1. The method used to track the structure of the vortex ring core is described in section 4.2. An assessment of the numerical approach is provided in section 4.3. The study of vortex rings with various initial core vorticity profiles is presented in section 4.4. The structure of the equilibrium state vortex rings is described in section 4.5. The behaviour of the vortex rings at large times is investigated in section 4.6. Finally, the conclusions of the study are summarised in section 4.7.

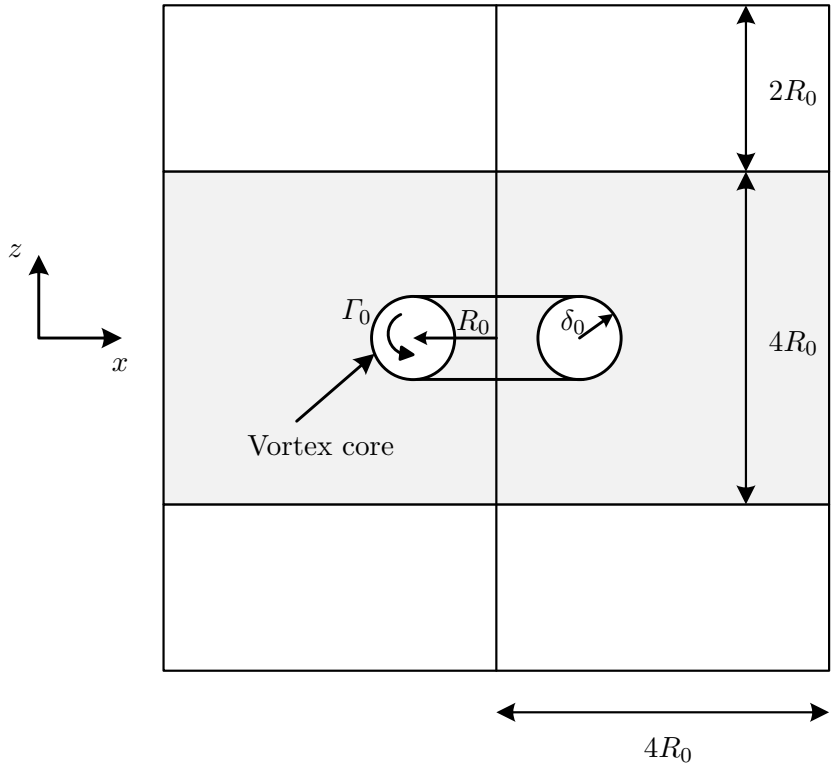

Figure 4.1: Schematic of a section of the computational domain ($y = 0$) for the study of the classical vortex rings. The shaded region corresponds to the logging domain.

4.1 Numerical approach

The simulations were carried out in a cubic domain with dimensions $L_x \times L_y \times L_z$ along the Cartesian coordinate directions x, y, and z respectively. The initial setup consisted of a vortex ring of radius R_0 and circulation Γ_0 with its centre located at $(0, 0, 0)$ and its axis aligned with the z-axis (Figure 4.1).

Periodic boundary conditions were used along the x and y directions. This effectively simulates a periodic square array of vortex rings. Therefore the domain size needs to be large enough that the effect of the array on the evolution of a single ring is negligible.

4.1.1 Comoving reference frame

During the propagation of a vortex ring in viscous flow, a narrow trailing wake is formed. If the simulation of vortex ring dynamics is performed in a triply periodic domain, the vortex ring would encounter and interact with its own wake. To avoid this, the computation was performed with respect to a reference frame which moved in the z

direction along with the vortex ring. Inflow and outflow boundary conditions were used at the $z = L_z/2$ and $z = -L_z/2$ boundaries.

An integral-proportional controller was used to determine the velocity of the reference frame at each timestep ($W_{ref}(t)$) required to maintain the vortex ring close to the centre of the reference frame. The location of the vortex ring along the z-axis with respect to the origin of the comoving reference frame was calculated as

$$Z(t) = \frac{1}{2\Omega} \int_V z\omega^2 \mathrm{d}V \tag{4.1}$$

where $\Omega = \frac{1}{2}\int_V \omega^2 \mathrm{d}V$ is the total enstrophy. The integral-proportional controller was used to maintain $Z(t)$ close to the target location $Z_c = 0$, ensuring that the vortex ring remained close to the center of the comoving reference frame. The time-dependent velocity of the co-moving frame is given by

$$W_{ref}(t) = 2c_1(Z(t) - Z_c) + c_2^2 \int_0^t (Z(t') - Z_c)\mathrm{d}t', \tag{4.2}$$

where c_1 and c_2 are damping and oscillation timescales. The values adopted for the damping and oscillation timescales in the integral-proportional controller are $c_1 = 2\Gamma_0/R_0^2$ and $c_2 = 4\Gamma_0/R_0^2$ as used in Archer et al. (2008).

Since the calculations were performed with respect to the reference frame, the inflow boundary condition at the inlet boundary was given by $w(x, y, L_z/2) = -W_{ref}(t)$ (assuming L_z is large enough that the velocity induced by the vortex ring at the inlet boundary is negligible). Irrotationality of the inlet flow was enforced by applying the boundary conditions $\partial u/\partial z = \partial v/\partial z = 0$ at the inlet $z = L_z/2$. At the outlet boundary $z = -L_z/2$, linear gradient conditions, $\partial u/\partial z = \partial v/\partial z = \partial w/\partial z = 0$ were imposed.

The numerical approach described above is the same as that used by Archer (2008).

4.1.2 Vortex ring initialisation

For a chosen initial core azimuthal vorticity profile the axisymmetric vorticity field was used to obtain the initial velocity field using the vector stream function method outlined below.

For a given initial vorticity field $\boldsymbol{\omega}_i$, the velocity stream function $\boldsymbol{\Psi}$ is obtained by solving

$$\nabla^2 \vec{\boldsymbol{\Psi}} = -\vec{\boldsymbol{\omega}}_i \tag{4.3}$$

and the velocity field is given by

$$\vec{\boldsymbol{u}} = \nabla \times \vec{\boldsymbol{\Psi}}. \tag{4.4}$$

If the initial vorticity field is not exactly divergence-free, then it differs from the final divergence-free vorticity field $\vec{\boldsymbol{\omega}}_f = \nabla \times \vec{\boldsymbol{u}}$. The initialisation method effectively applies a correction that renders the vorticity field divergence-free.

4.1.3 Simulation details

For all the simulations in this chapter, a domain size of $L_x = L_y = L_z = 8R_0$ was used with $N_x = 512, N_y = 512, N_z = 512$ uniformly spaced grid points along the x, y, z directions respectively. The timestep was chosen such that the maximum value across the domain of the Courant-Freidrichs-Lewy (CFL) number based on the local velocity and grid size remained below 0.20 throughout the simulation to ensure numerical stability.

Archer (2008) who had used the same numerical approach, showed that increasing the domain size beyond $8R_0 \times 8R_0 \times 8R_0$ had a negligible effect on the evolution of the characteristics of a vortex ring with an initial radius of R_0. The adequacy of the numerical resolution is demonstrated in section 4.3.

Simulations of vortex rings with a range of different initial azimuthal vorticity profiles were performed. In addition, the Reynolds number at which the simulations were performed was also varied. Table 4.1 lists the different profiles used and the values of the parameters used. In addition to the analytically defined profiles, a solution to the steady state, axisymmetric Euler equations was used as the initial condition for case ES. The solution satisfies the condition $\omega_\theta/r = g(\psi)$ where ψ is the Stokes streamfunction in a reference frame in which the vortex ring is steady. The solution was computed using the numerical Euler solver described in appendix A. The swirl free vortex rings computed using this method are solutions for the functional form $\omega_\theta/r = \beta\psi_+^\zeta/2$.

4.2 Tracking vortex core structure

The shape of the core vorticity profile was tracked using the instantaneous values of the translation parameter C given by

$$C = \frac{4\pi RU}{\Gamma} - \log\left(\frac{8R}{\delta}\right). \tag{4.5}$$

The velocity of the vortex ring in the simulation with respect to a stationary reference frame is $W_{\mathrm{ref}}(t) + \mathrm{d}Z/\mathrm{d}t$ where $W_{\mathrm{ref}}(t)$ is the velocity of the comoving reference frame.

Archer (2008) determined that the axial velocity induced by the infinite periodic square array of vortex rings with $L_x = L_y = \lambda$ is given by

$$\widetilde{w} \approx -9.032 \frac{\Gamma R^2}{4\lambda^3} \,. \tag{4.6}$$

Therefore the velocity of the vortex ring in unbounded fluid, U, is given by

$$U = W_{ref}(t) + \mathrm{d}Z/\mathrm{d}t - \widetilde{w} \,. \tag{4.7}$$

The parameters of the vortex ring in (4.5) were defined as integral quantities on a radial plane as in Archer et al. (2008). The circulation is defined as

$$\Gamma = \iint \omega_\theta \mathrm{d}r\mathrm{d}z \,. \tag{4.8}$$

The first and second radial moments of the azimuthal vorticity,

$$\begin{aligned} R_1 &= \frac{1}{\Gamma} \iint r\omega_\theta \mathrm{d}r\mathrm{d}z \\ R_2^2 &= \frac{1}{\Gamma} \iint r^2\omega_\theta \mathrm{d}r\mathrm{d}z \,, \end{aligned}$$

are used to define the ring radius R and core radius δ with

$$R = R_1 \tag{4.9}$$

$$\delta = \sqrt{2(R_2^2 - R^2)} \,. \tag{4.10}$$

If the integration is performed over the entire computational domain, the presence of a trailing wake affects the tracking of the vortex ring characteristics. Therefore the integration is only performed over a logging domain attached to the comoving frame defined by $-2R_0 < z < 2R_0$ (Shaded region in figure 4.1).

4.3 Assessment of numerical approach

The accuracy of the results obtained using the numerical approach is demonstrated in this section.

Case	Core profile	$\omega_\theta(r,z)$	Parameters
G1	Gaussian	$\dfrac{\Gamma_0}{\pi\delta_0^2}\exp\left(-\dfrac{\rho^2}{\delta_0^2}\right)$	$\delta_0/R_0 = 0.14$, $\Gamma_0/\nu = 3000$
G2	Gaussian		$\delta_0/R_0 = 0.20$, $\Gamma_0/\nu = 1500$
G3	Gaussian		$\delta_0/R_0 = 0.32$, $\Gamma_0/\nu = 4500$
G4	Gaussian		$\delta_0/R_0 = 0.40$, $\Gamma_0/\nu = 1500$
E1	Elliptical	$\dfrac{\Gamma_0}{\pi ab\delta_0^2}\exp\left(-\dfrac{(r-R_0)^2/a^2 + z^2/b^2}{\delta_0^2}\right)$	$\delta_0/R_0 = 0.3$, $a = 1.0, b = 0.6$, $\Gamma_0/\nu = 1500$
E2	Elliptical		$\delta_0/R_0 = 0.3$, $a = 0.6, b = 1.0$, $\Gamma_0/\nu = 1500$
ST	Smoothed top-hat	$\dfrac{\Gamma_s}{\pi\delta_0^2}$ $\quad \dfrac{\rho}{\delta_0} < 0.9$ $\dfrac{\Gamma_s}{\pi\delta_0^2}\left(\dfrac{1-\cos(10\pi(1-\rho/\delta_0))}{2}\right)$ $\quad 0.9 < \dfrac{\rho}{\delta_0} < 1$ 0 $\quad 1 < \dfrac{\rho}{\delta_0}$	$\delta_0/R_0 = 0.3$ $\Gamma_s/\Gamma_0 = 1.108$ $\Gamma_0/\nu = 1500$
SE	Steady Euler solution	$\dfrac{\beta r}{2}\psi_+^\zeta$ $\psi_+ = \max(\psi, 0)$	$\beta = 350$, $\zeta = 1.5$, $\Gamma_0/\nu = 1500$

Table 4.1: Initial core azimuthal vorticity profiles. The radial distance from the circumferential core axis is $\rho = \sqrt{(r-R_0)^2 + z^2}$.

4.3.1 Grid resolution test

The adequacy of the spatial resolution was checked by tracking the volume integrated kinetic energy per unit mass with respect to the co-moving reference frame (K) given by

$$K = \frac{1}{2}\iiint_V (u^2 + v^2 + w^2 - W_{ref}^2)\mathrm{d}V\,. \tag{4.11}$$

The integration was performed over the entire computational domain. In the absence of spatial discretisation error, the rate of change of K would be exactly balanced by the volume integrated rate of kinetic energy dissipation (ϵ_K) after accounting for the volume integrated kinetic energy flux out of the domain (F_K). The energy balance is given by

$$-\frac{\mathrm{d}K}{\mathrm{d}t} = \epsilon_K + F_K \tag{4.12}$$

The difference between the left and right hand sides of this equation is a measure of the spatial discretisation error in computing the flow.

Figure 4.2 shows the histories of the left and right hand sides of the energy balance equation for the simulation of case G3 which was performed at $Re = 4500$. The difference between the two sides of the energy balance equation remains less than $1 \times 10^{-5}\Gamma_0^3/R_0$ throughout the simulation. This shows that the error due to the spatial discretisation remains negligibly small throughout the entire simulation.

4.3.2 Comparison with case from Archer et al. (2008)

Case G1 was defined using the same initial parameters as case C1 from Archer et al. (2008). The values of the integral ring parameters for this case are available at $t = 15R_0^2/\Gamma_0$ from their study. The values of the integral parameters at $t = 15R_0^2/\Gamma_0$ for case G1 from the present work are listed in table 4.2 and found to match the corresponding values from Archer et al. (2008) nearly exactly. This further demonstrates the accuracy of the present simulations.

4.4 Effect of initial vorticity profile

In this section, the evolution of the vortex rings from table 4.1 with a wide range of initial core vorticity profiles is discussed. The changing structure of the vortex core was tracked using the method described in section 4.2. The instantaneous values of the

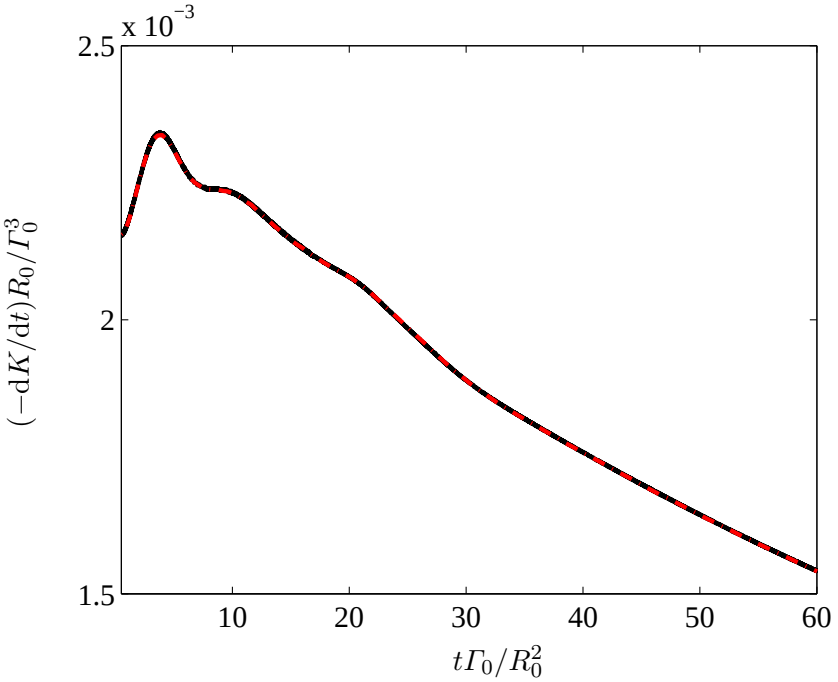

Figure 4.2: Comparison of histories of ——— Rate of decrease of volume-integrated kinetic energy $(-\mathrm{d}K/\mathrm{d}t)$ and - - - - Sum of volume-integrated rate of dissipation and energy flux $(\epsilon_K + F_K)$ for case G3. The two curves are practically overlapping.

Case	$t\Gamma_0/R_0^2$	$\Gamma(t)/\Gamma_0$	$R(t)/R_0$	$\delta(t)/R_0$
G1 from present study	15.0	0.9995	0.996	0.202
C1 from Archer et al. (2008)	15.0	0.999	0.995	0.203

Table 4.2: Comparison of integral ring parameters at $t = 15R_0^2/\Gamma_0$ for the cases G1 from the present study and C1 from Archer et al. (2008) defined using the same initial parameters.

translation parameter C were computed from (4.5) and plotted against the corresponding slenderness ratio ϵ.

Figure 4.3 shows the variation of C with ϵ for the Gaussian initialised vortex rings. In all cases, the vortex rings undergo a rapid readjustment after initialisation, shedding some amount of circulation into the wake. The plots of C vs. ϵ are attracted onto and collapse into a single curve. Table 4.3 shows the approximate time at which the vortex rings join the single-parameter family (t_{eq}) and the values of the integral parameters at that time. The loss of circulation associated with the readjustment of Gaussian initialised vortex

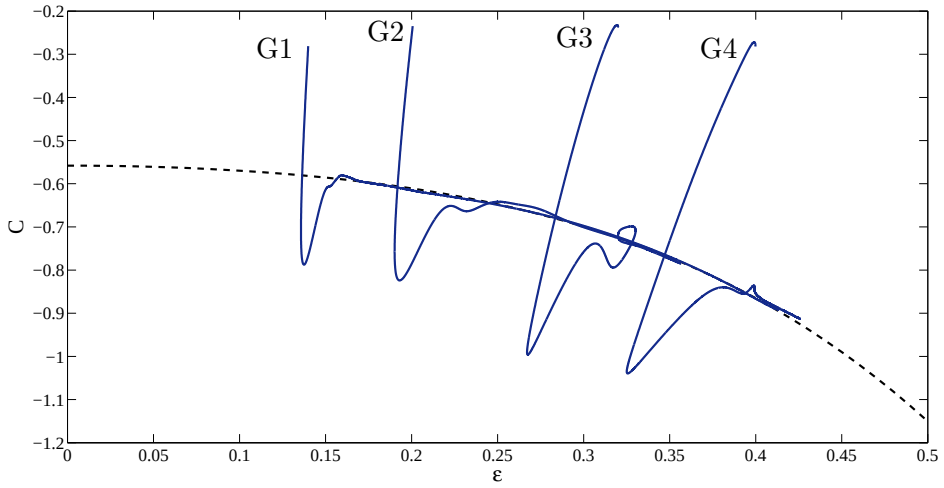

Figure 4.3: Translation parameter C plotted against the slenderness ratio ϵ for cases G1, G2, G3 and G4 involving Gaussian initialised vortex rings (identified by the initial slenderness ratios). The dashed line corresponds to equation (4.13) from Archer et al. (2008).

rings increases with initial core size as noted by Archer et al. (2008). Archer et al. (2008) used the equation

$$C = -1.12\epsilon^2 - 5.0\epsilon^4 - 0.558 \tag{4.13}$$

to represent the variation of C for the equilibrium vortex rings in their study in which the slenderness ratio varied up to approximately 0.38. The equation is seen to closely match the common C vs. ϵ curve from the present work (within the same range of slenderness ratios).

Figure 4.4 shows the variation of C with ϵ for the vortex rings initialised with the different non-Gaussian profiles, which are also found to readjust to the equilibrium state identified by Archer et al. (2008). Both the elliptical profiles relax to the equilibrium state within $t \simeq 26R_0^2/\Gamma_0$. The smoothed top-hat vortex ring reaches the equilibrium state after a substantially longer time period of readjustment of approximately $63R_0^2/\Gamma_0$.

The initial location of the C vs. ϵ plot for case SE, initialised with an inviscid steady Euler solution, is found to be close to the curve defined by (4.13). The vortex ring undergoes readjustment within $t \simeq 24R_0^2/\Gamma_0$ shedding only 0.2% of its initial circulation. Figure 4.4 indicates that the core vorticity profile for the inviscid solution generated using the power law function $\omega_\theta/r = 175\psi_+^{1.5}$ is close to the vorticity profile of a viscous equilibrium state vortex ring with the same slenderness ratio.

Vortex rings with a range of initial core vorticity profiles are thus seen to readjust into a common equilibrium state. The shape of the core vorticity profile of the readjusted vortex rings is determined by the slenderness ratio alone. Since the slenderness ratio

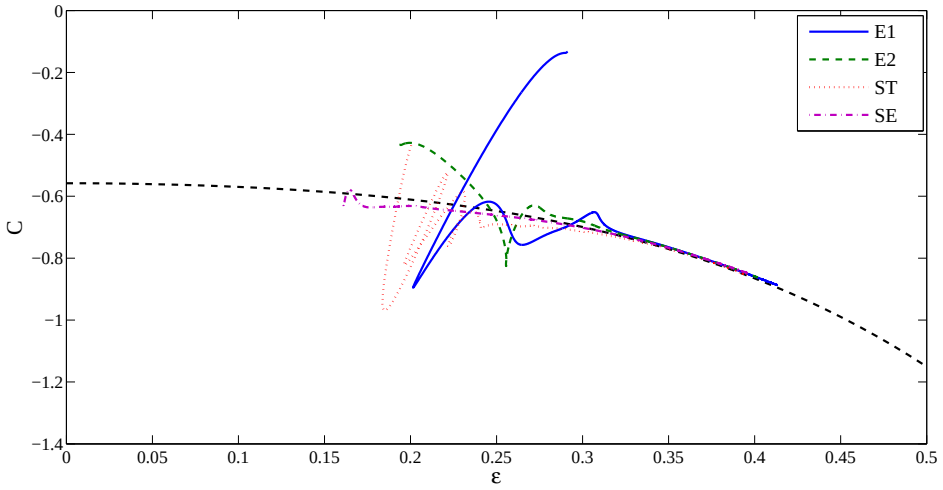

Figure 4.4: Translation parameter C plotted against the slenderness ratio ϵ for cases E1, E2, ST and SE involving non-Gaussian vortex rings. The black dashed line corresponds to equation (4.13) from Archer et al. (2008).

Case	$t_{eq}\Gamma_0/R_0^2$	Γ_{eq}/Γ_0	R_{eq}/R_0	δ_{eq}/R_0
G1	15.0	0.9995	0.996	0.202
G2	20.0	0.991	0.991	0.302
G3	32.0	0.952	1.016	0.330
G4	40.0	0.887	1.035	0.420
E1	26.0	0.960	1.010	0.329
E2	22.0	0.987	0.989	0.316
ST	63.0	0.971	0.993	0.350
SE	24.0	0.998	0.985	0.298

Table 4.3: Approximate time taken for the different vortex rings to relax to the equilibrium state and the values of the integral ring parameters at that time.

changes during the evolution of the vortex ring, the equilibrium state is not strictly self-similar.

4.5 Structure of the equilibrium vortex rings

An axisymmetric, steady vortex ring (in a co-moving reference frame) in inviscid flow satisfies the condition that the quantity ω_θ/r is a function of the streamfunction alone. At high Reynolds numbers, the core vorticity profile of an equilibrium vortex ring in viscous flow should nearly satisfy this condition.

The Stokes streamfunction (ψ) field was obtained for a readjusted equilibrium vortex ring in a reference frame translating with the ring. Figure 4.5a shows that the contours of ψ and ω_θ/r are nearly overlapping. The scatter plot of ω_θ/r vs. ψ for points on a radial plane is found to collapse onto a single curve (Figure 4.5b). The function $g(\psi) = \omega_\theta/r$ is well represented by a power-law ψ_+^ζ with $\zeta = 1.8$ except for values of ψ close to 0 where the viscous diffusion effects are important.

Figure 4.6 shows scatter plots of ω_θ/r vs. ψ for equilibrium vortex rings at different slenderness ratios and the exponents of the power law ζ used to represent them. The exponent ζ is found to decrease with increasing slenderness ratio of the equilibrium vortex ring. The extent of the regions where the power law does not hold well (near $\psi = 0$) increases with the slenderness ratio.

Archer et al. (2008) described the process of detrainment of vorticity into the wake in viscous flow. Fluid with vorticity is diffused across the $\psi = 0$ streamline (the $\psi = 0$ stream-surface is the entrainment bubble) and a part of it passes into the wake. The diffusion of vorticity across the $\psi = 0$ streamline increases with the slenderness ratio. For the thick-cored vortex ring in figure 4.6 with $\epsilon = 0.42$, the azimuthal vorticity is non-zero for $-0.2 \lesssim \psi < 0$. The width of the scatter plots also increases with ϵ and for the thick-cored equilibrium vortex ring at $\epsilon = 0.42$, the scatter plot is considerably wide. Figure 4.7 shows that the contours of ψ and ω_θ/r for this ring do not overlap very well away from the center of the core.

These results indicate the possibility of a core size limit above which the behaviour of the equilibrium vortex rings is qualitatively different.

4.6 Vortex ring evolution at large times

In this section the continuation of the common equilibrium state at large times and the existence of a core size limit is investigated. Simulations were performed using Gaussian

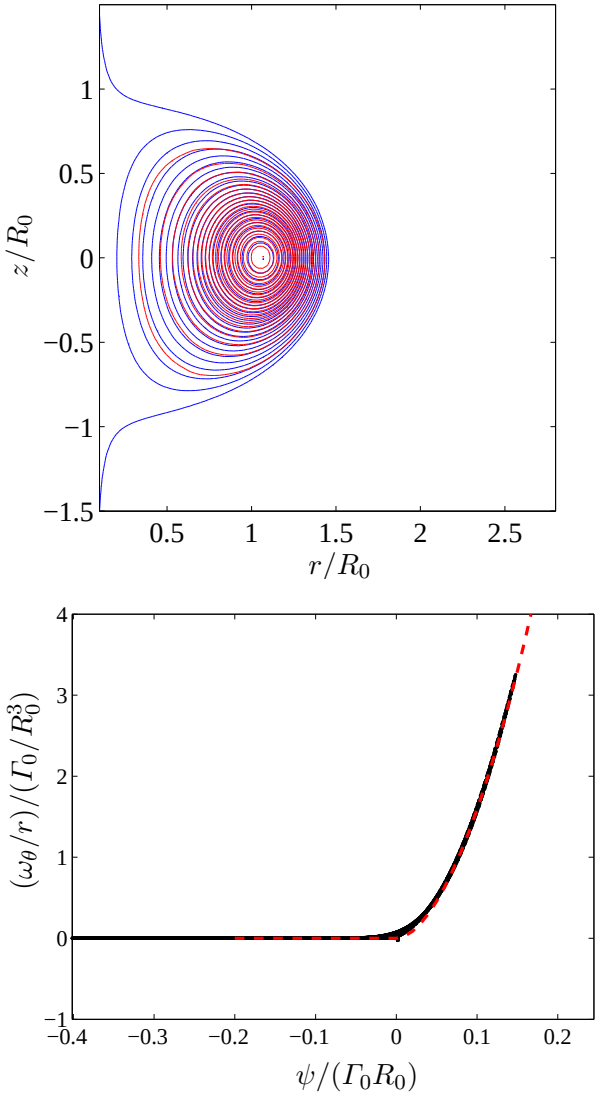

Figure 4.5: (a) Overlapping contours of ψ (blue) and ω_θ/r (red) on a radial plane (b) Plot of ω_θ/r vs. ψ for all points on a radial plane for a readjusted vortex ring with $\epsilon = 0.30$. Red dashed line corresponds to $k\psi_+^{1.8}$.

initialised vortex rings with initial slenderness ratios of $\epsilon = 0.2$, 0.3, 0.3 and 0.4 at Reynolds numbers $\Gamma_0/\nu = 1500$, 1150, 1500 and 1850 respectively.

Figure 4.8 shows plots of C vs. ϵ for the four cases. All the vortex rings underwent a readjustment to the equilibrium state. As described in section 4.4, the plots of C vs. ϵ attract onto a common curve. As the vortex rings propagate their slenderness ratios increase with time due to core diffusion. The equation 4.13 from Archer et al. (2008) was used to represent equilibrium vortex rings with $\epsilon \lesssim 0.38$. As ϵ increases above $\simeq$0.4, the common attractor curve shifts slightly away from this equation.

The different equilibrium rings continue to follow a common path up to a turning point at $\epsilon \simeq 0.47$. As indicated by the results in section 4.5, above $\epsilon \simeq 0.47$ equilibrium

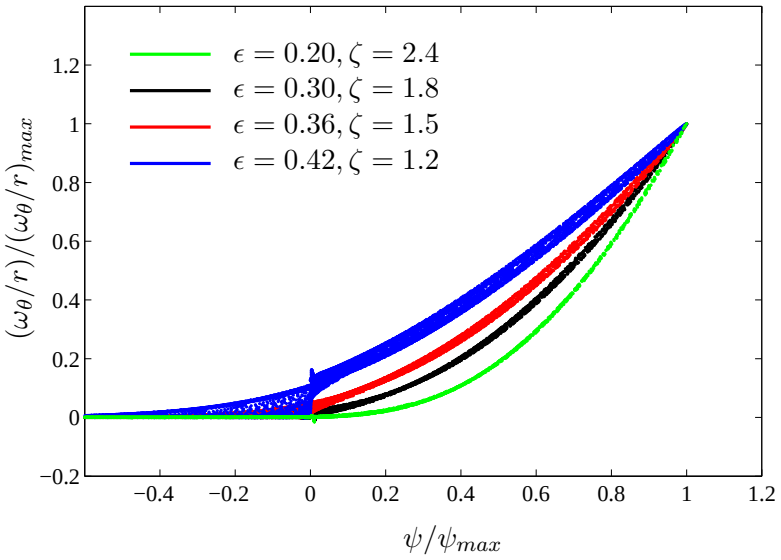

Figure 4.6: Plots of ω_θ/r vs. ψ for all points on a radial plane for equilibrium vortex rings with differing slenderness ratios. The values of ζ for the best-fit power laws for each case are as indicated.

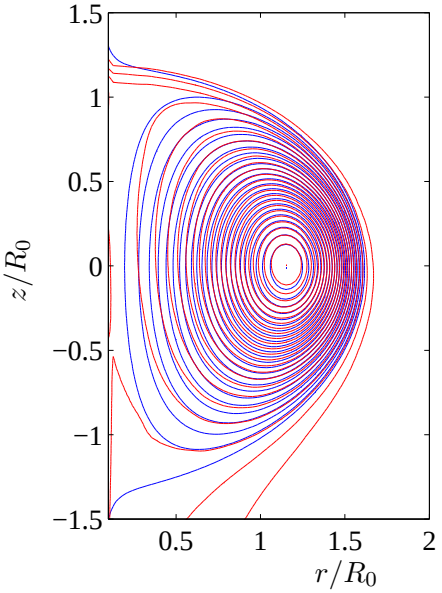

Figure 4.7: Contours of ψ (blue) and ω_θ/r (red) on a radial plane for thick cored vortex ring with $\epsilon = 0.42, \zeta = 1.2$.

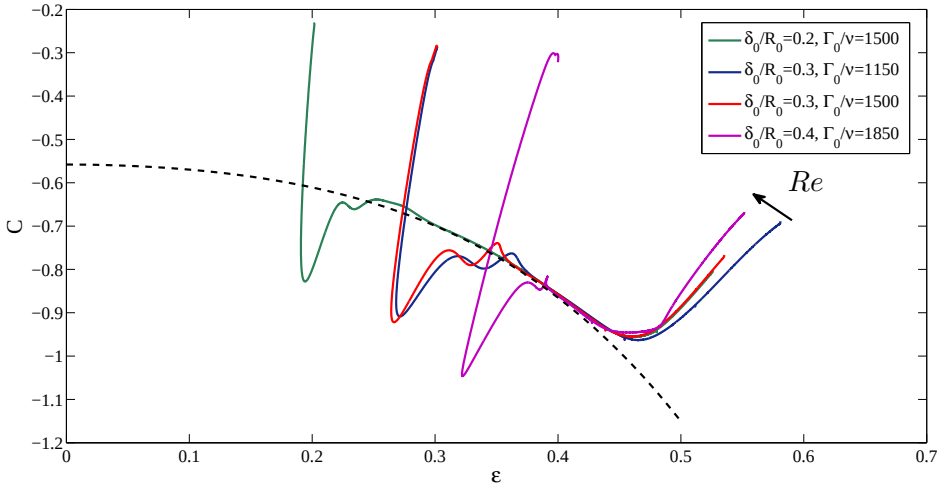

Figure 4.8: Core profile parameter C plotted against the slenderness ratio ϵ for Gaussian initialised vortex rings with initial slenderness ratios of $\epsilon = 0.2$, 0.3, 0.3 and 0.4 at Reynolds numbers $\Gamma_0/\nu = 1500$, 1150, 1500 and 1850 respectively. The dotted line corresponds to equation (4.13) from Archer et al. (2008).

vortex rings at different Reynolds numbers do not continue to follow a common path. For greater values of ϵ the paths instead, diverge dependent on Reynolds number. In figure 4.8, the two vortex rings at $Re = 1500$ are seen to continue to follow a common path for $\epsilon > 0.47$.

4.6.1 Comparison with experiment

An analytical solution is known for the asymptotic drift velocity of a vortex ring at large times (Cantwell and Rott (1988)).

$$\begin{aligned} U &= k\frac{I}{\rho}(\nu t)^{-1.5} \\ k &= 3.7038 \times 10^{-3} \end{aligned} \tag{4.14}$$

The asymptotic state corresponds to a slowly decaying, fat vortex ring governed by the Stokes equations. In this section, the departure of the equilibrium vortex rings from the common path is understood in the context of the known behaviour of vortex rings at large times.

Weigand and Gharib (1997) generated vortex rings in a water tank using a piston-cylinder mechanism at different Reynolds numbers and tracked their propagation speeds from their formation up to large times and showed that the propagation velocity approached the exact asymptotic solution for the drift velocity given by Cantwell and Rott

(1988). A comparison is performed with one of the vortex rings from their experimental study.

Weigand and Gharib (1997) used Laser Doppler Anemometry (LDA) and Digital Particle Image Velocimetry (DPIV) to map the vorticity field at a location where the vortex rings had completed the formation process and reached a fully developed state. The case for which the Reynolds number based on the circulation at the mapping location was 1150 was chosen for the comparison simulation. They fit a Gaussian profile to the core vorticity profiles of the vortex rings and the slenderness ratio at this location for the chosen case was 0.338. The present simulation used a readjusted vortex ring with the same parameters as the chosen case as the initial condition.

A preliminary DNS was performed using a Gaussian initialised vortex ring with a radius R_0, circulation Γ_0 and an initial slenderness ratio of 0.2 at a Reynolds number of $\Gamma_0/\nu = 1150$. The vortex ring was allowed to evolve in time until a readjusted vortex ring with the target slenderness ratio of 0.338 was obtained. This readjusted vortex ring was used as the initial condition for the main DNS of the comparison case from the experimental study. A subscript i is used to refer to the parameters defining the vortex ring at this new initial condition. The kinematic viscosity was reset such that the Reynolds number based on the circulation of the readjusted vortex ring (Γ_i/ν) was 1150.

Weigand and Gharib (1997) used Saffman's (1970) model for the propagation velocity of the vortex rings

$$U_V^* = \frac{16\pi}{k}(R_0^2 + k't^*)^{-3/2}, \tag{4.15}$$

$$\text{where } U_V^* = 4\pi U R_i/\Gamma_i,\ t^* = \nu t/(16R_i^2)\,.$$

The best fit for the model was obtained with their data for $k = 14.4$ and $k' = 7.8$. The value of t^* in the experiment at the initial condition for this simulation is 1.79×10^{-3}. Figure 4.9a shows the plot from Weigand and Gharib (1997) comparing the best-fit model of U_V^* vs. t^* with the numerical simulation of Stanaway et al. (1988). At large times, the model tends to the exact asymptotic solution ($t \to \infty$) for the drift velocity given by Cantwell and Rott (1988), which is dependent only on the initial impulse of the vortex ring and the kinematic viscosity of the fluid.

Figure 4.9b shows that the data from the present simulation matches the best-fit model very well both at moderate values of the slenderness ratio and at large times when the slenderness ratio is large. Figure 4.10 shows the variation of C vs. ϵ for this simulation. The turning point $\epsilon \simeq 0.47$ occurs at $t^* \simeq 1.18 \times 10^{-2}$. From figure 4.9b it is seen that

this time approximately corresponds to the time period in which the vortex ring velocity begins to approach the large time asymptotic solution.

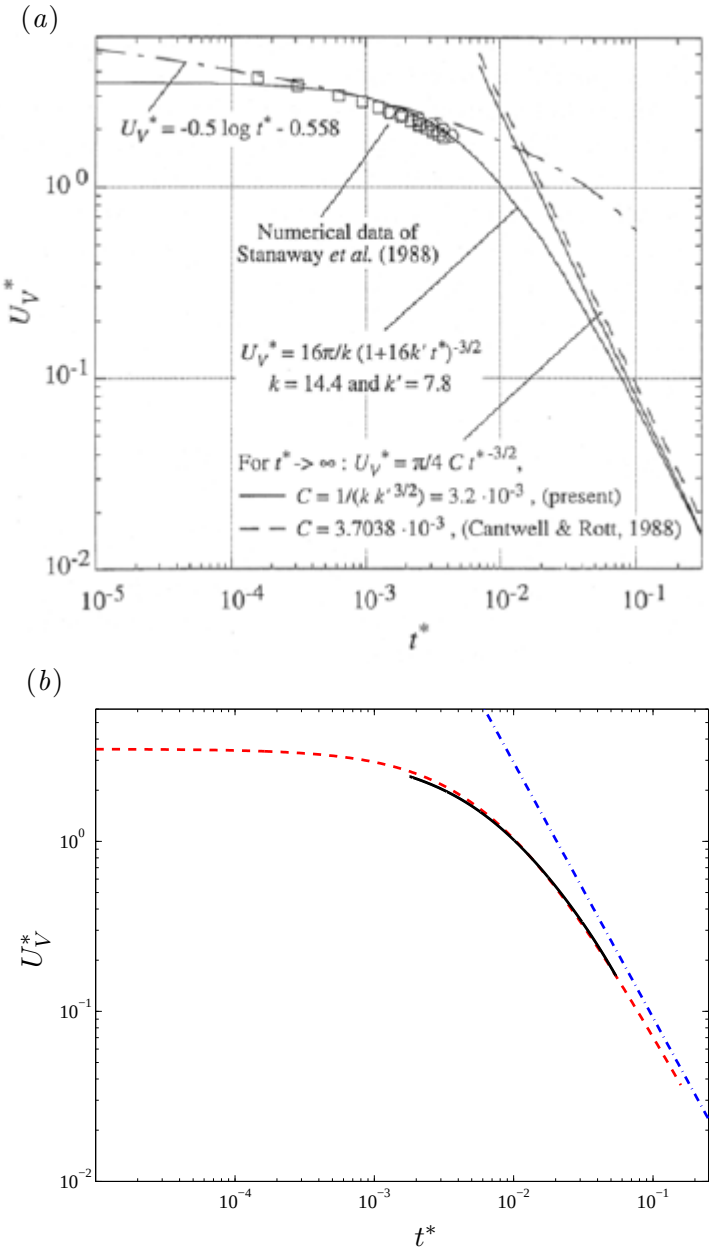

Figure 4.9: (*a*) Plot of U_V^* vs. t^* from Weigand and Gharib (1997) (*b*) Comparison of plots of U_V^* vs. t^* from ——— the present simulation, - - - - Best fit model (4.15) from Weigand and Gharib (1997) and - . - . - the asymptotic solution (4.14) from Cantwell and Rott (1988).

The divergence of the vortex rings from the common path described in section 4.4 can now be explained. As the slenderness ratio of the vortex ring grows with time, a turning point is reached ($\epsilon \simeq 0.47$) at which the growth of the vortex core begins to be constrained by the entrainment bubble and significant amounts of circulation are shed

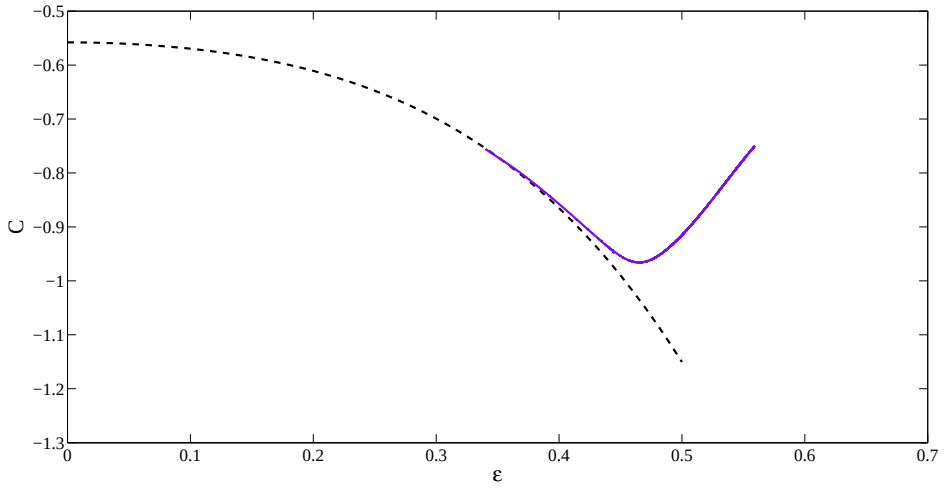

Figure 4.10: Core profile parameter C plotted against the slenderness ratio ϵ for the numerical simulation of the case from Weigand and Gharib (1997). The dotted line corresponds to equation (4.13) from Archer et al. (2008).

into the wake. The vortex ring slows down rapidly and the viscous terms in the Navier-Stokes equations become dominant. The shape of the core vorticity profile begins to be influenced by the viscosity and the paths of the vortex rings on the C vs. ϵ plot begin to diverge into separate paths based on the viscosity. At large times, the velocity of the vortex ring can be expected to asymptotically decay as $(\nu t)^{-3/2}$ according to the solution given by Cantwell and Rott (1988) (see figure 4.9b).

4.7 Conclusions

Vortex rings with different initial core vorticity profiles undergo a readjustment, shedding circulation and relaxing to a common equilibrium state. This equilibrium state is a single parameter family in which the shape of the core vorticity profile is uniquely determined by the slenderness ratio of the vortex ring. The structure of the equilibrium vortex rings was found to be close to a solution of the inviscid, steady, Euler equations with the quantity ω_θ/r represented by a power law ψ_+^ζ.

A turning point is reached by the equilibrium vortex rings when the slenderness ratio grows to ∼0.47. After the turning point is reached, viscosity begins to determine the shape of the core vorticity profile. The common path followed by the equilibrium vortex rings diverges into multiple paths dependent on Reynolds number. The velocity of the vortex rings after the turning point begins to approach the behaviour of the large time asymptotic solution given by Cantwell and Rott (1988).

Chapter 5

Vortex reconnection: Preliminary simulations

The problem of a vortex ring impinging on a non-deformable, free-slip surface at an oblique angle of incidence is equivalent to an oblique-angle collision of two vortex rings with the interaction plane coinciding with the surface. To validate the numerical approach used in this report for studying vortex ring reconnection, a comparison is performed with the numerical simulation of colliding vortex rings performed by Kida et al. (1991).

Kida et al. (1991) used a spectral method on a grid with 64^3 collocation points in a cubic domain. They performed numerical simulations for varying values of Reynolds number and angle of collision. This study was chosen for the validation of the numerical method since the quantitative history of the maximum vorticity in the interacting vortex cores is available. During vortex reconnection, the vortex cores undergo significant stretching. So the evolution of the maximum vorticity within the cores provides an ideal sensitive measure for performing a comparison.

In section 5.1, the initial setup used for the simulations discussed in this chapter is outlined. In section 5.2 the results of the validation study are presented. The conclusions from the chapter are summarised in section 5.3.

5.1 Simulation setup

The initial setup consists of two vortex rings of radius R_0 and circulation Γ_0 in a cubic domain of dimensions L^3 with their centres located at $\left(\frac{d}{2}\cos(\pi/4), \frac{d}{2}\sin(\pi/4), 0\right)$ and $\left(-\frac{d}{2}\cos(\pi/4), -\frac{d}{2}\sin(\pi/4), 0\right)$ with respect to the Cartesian coordinates (x, y, z) where

d is the initial separation between the ring centres. The axes of the vortex rings are aligned with the z-axis direction (figure 5.1).

The plane at which the vortex rings collide, $x = -y$ is referred to as the 'collision plane' and the plane $x = y$ as the 'symmetry plane'.

Case I from Kida et al. (1991) was chosen for the validation study. The parameter values for the selected case are: $\delta/R_0 = 0.399, d/R_0 = 1.86, Re = \Gamma_0/\nu = 1153$. The length of the sides of the cubic domain is $L = 6.40R_0$. Periodic boundary conditions are used along all three co-ordinate directions. The core of the vortex ring was initialised with a Gaussian distribution of vorticity. The initial velocity field was obtained using the procedure outlined in section 4.1.2.

The plots of the evolution of the maximum vorticity on the symmetry and collision planes with time were found to be nearly overlapping for flows computed using 384^3 and 512^3 uniformly spaced grid points. The difference remained less than 3% even at the peak values of the maximum vorticity proving the adequacy of the numerical resolution with 384^3 grid points. A constant timestep was chosen such that the maximum value across the domain of the Courant-Freidrichs-Lewy (CFL) number based on the local velocity and grid size remained below 0.20 throughout the simulation.

5.2 Results

5.2.1 Comparison with Kida et al. (1991)

The evolution of the vortex rings in the present simulation is qualitatively similar to the results of Kida et al. (1991). The vortex rings initially travelled along the z-axis due to their self-induced velocity. Due to the mutually induced velocity, the inner parts of the vortex rings are retarded leading the rings to turn towards each other resulting in a collision. The initially nearly circular vortex cores are flattened along the direction normal to the collision plane, stretched along the z-axis direction and deformed into a head-tail shape. The vortex filaments are stretched in the direction normal to the symmetry plane leading to a rapid growth of maximum vorticity on the symmetry plane. The oppositely signed vortex lines from the two rings undergo cancellation due to viscous decay. Simultaneously the disconnected vortex filaments from the two rings undergo cross-linking. This is accompanied by creation of vorticity on the collision plane. This process is described in detail in section 6.3.

For a quantitative comparison, the histories of the maximum vorticity on the symmetry plane and the collision plane are compared with the results of Kida et al. (1991) in figure 5.2.

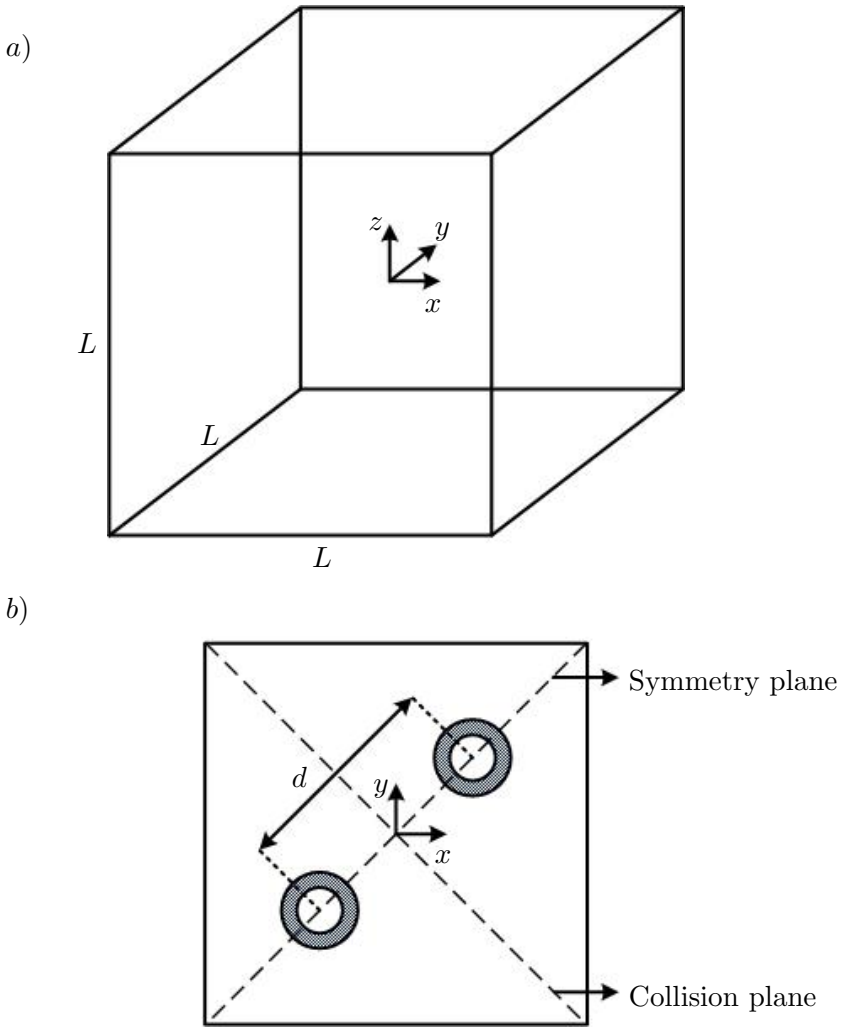

Figure 5.1: a) Schematic of the computational domain b) Section of the computational domain $z = 0$ for the validation study at initial time.

The maximum vorticity on the symmetry plane initially increases during the initial readjustment of the vortex ring. Subsequently it decreases due to viscous diffusion until the rings collide initiating the reconnection process at $t \simeq 30R_0^2/\Gamma_0$. During the reconnection the vorticity on the symmetry plane increases sharply due to the stretching of the vortex filaments and vorticity is created on the collision plane (along the direction normal to the collision plane) due to the cross-linking between the vortex rings.

There are significant differences between the maximum vorticity histories from the present simulation and from Kida et al. (1991). The plots of maximum vorticity on the symmetry plane roughly overlap until $t \sim 40R_0^2/\Gamma_0$ at which the peak value of $\sim \omega_0$ is reached for the case from Kida et al. (1991). The maximum vorticity continues to rise and reaches a higher peak value of $\sim 1.3\omega_0$ in the CGLES simulation. The evolution of maximum vorticity on the collision plane is similar for both cases except for a shift in

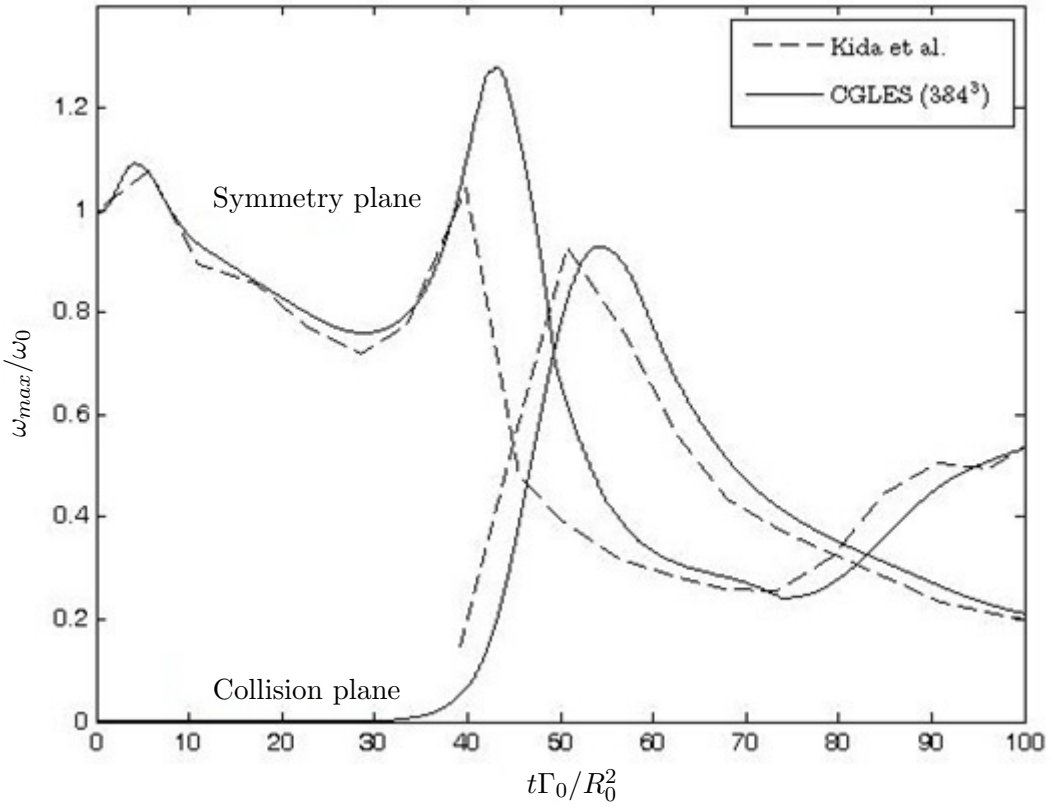

Figure 5.2: Comparison of the histories of maximum vorticity on the symmetry and collision planes (normal to the planes) normalized by the initial maximum on the symmetry plane from the present simulation (solid) and from Kida et al. (1991) (dashed).

time with the creation of vorticity on the collision plane beginning earlier for the case from Kida et al. (1991).

Due to the differences in the quantitative results in the two cases, an alternate method was used for the validation study. A simulation of the same problem was performed using a spectral DNS code and the results were compared with the results of the simulation performed with the finite difference code CGLES.

5.2.2 Comparison with the spectral DNS code simulation of vortex ring collision

The spectral DNS code has been previously used in other numerical studies (Redford et al., 2012). It uses a standard fully spectral Fourier spatial discretisation. The viscous terms are advanced in time using an analytic integration factor and the non-linear terms by a low-storage third-order Runge-Kutta method.

The same simulation setup described in section 5.1 was used for the spectral DNS. The plots of the evolution of the maximum vorticity on the symmetry and collision planes with time were found to be nearly overlapping for flows computed with the spectral

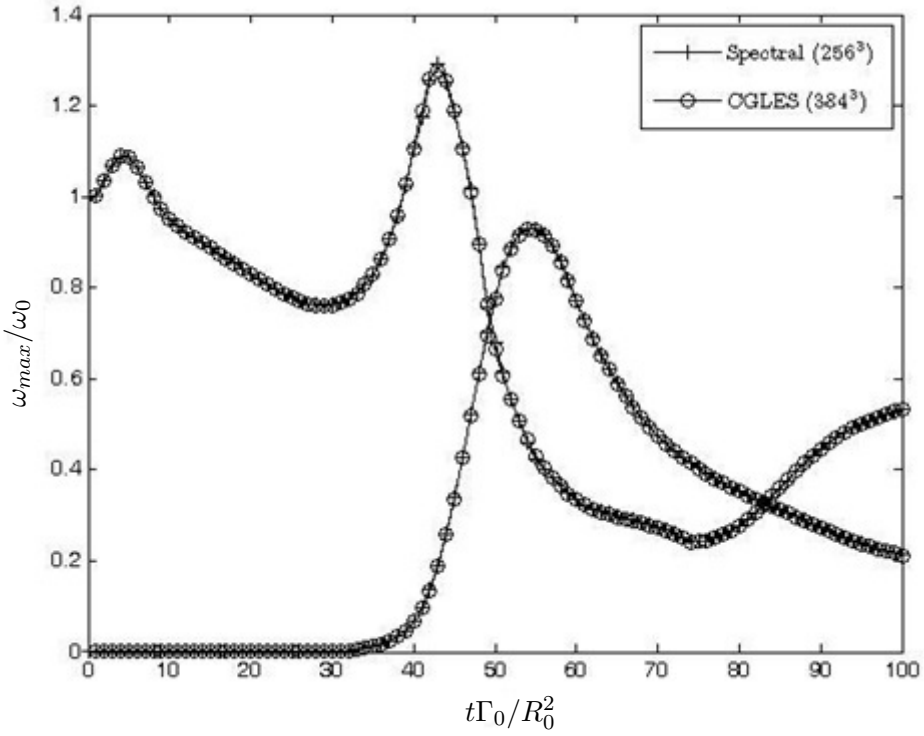

Figure 5.3: Histories of maximum vorticity on the symmetry and collision planes (normal to the planes) normalized by the initial maximum on the symmetry plane using the finite-difference code CGLES and the spectral DNS code.

code using 256^3 and 384^3 collocation points with the magnitude difference remaining less than 3% even at the peak values. The converged results obtained using the grid with 256^3 points were then compared with the results from the simulation performed with CGLES. The maximum vorticity evolution plots on the symmetry and collision planes from the two computed flows were found to overlap nearly exactly (figure 5.3). The strong agreement between the results of the simulations performed with different numerical codes based on a spectral method and a finite-difference method provides a strong validation of the numerical approach used for simulating vortex ring reconnection in this report.

5.2.3 Investigation of discrepancy with Kida et al. (1991)

The discrepancy between the histories of the maximum vorticity from Kida et al. (1991) and from the simulations performed with CGLES and the alternate spectral DNS code is investigated further. The fully resolved simulation using the alternate spectral DNS code used 256^3 collocation points. However, the simulation from Kida et al. (1991) was performed with a spectral method using 64^3 collocation points. This indicates the possibility that the simulation from Kida et al. (1991) was under-resolved with respect to the spatial discretisation. To test this possibility, an under-resolved simulation with 64^3

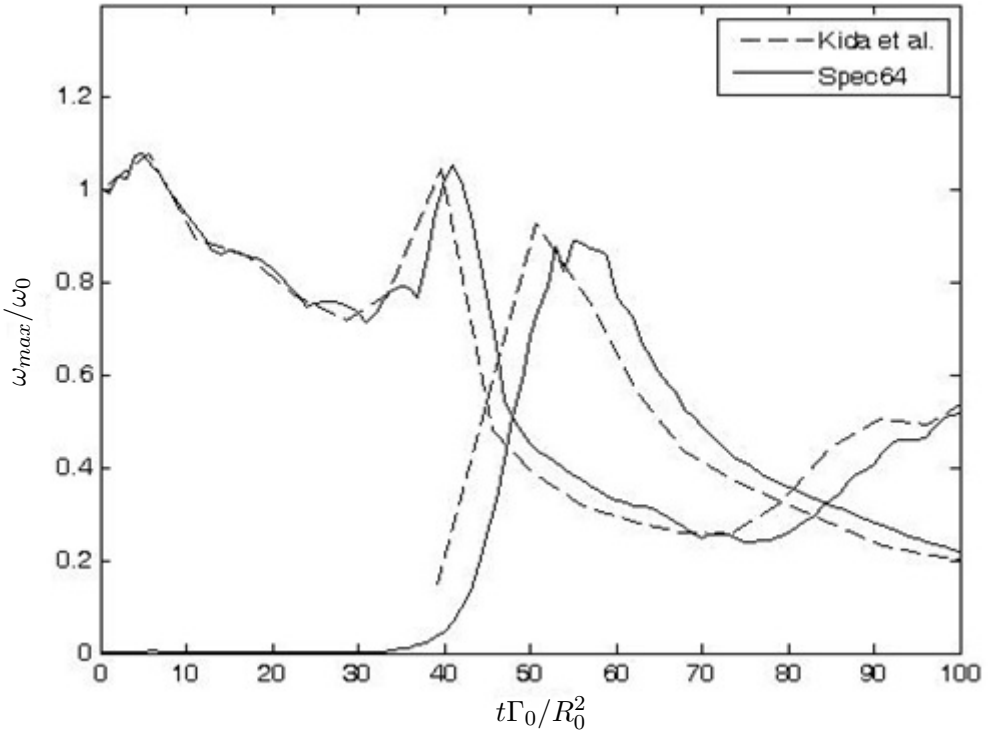

Figure 5.4: Histories of maximum vorticity on the symmetry and collision planes (normal to the planes) normalized by the initial maximum on the symmetry plane using the alternate spectral DNS code and from the results of Kida et al. (1991).

collocation points was also performed for the same problem using the alternate spectral DNS code.

Figure 5.4 shows that the maximum vorticity evolution plots obtained from the under-resolved simulation and from Kida et al. (1991) are roughly similar. The peak value attained by the maximum vorticity on the symmetry plane during the reconnection is lower for the under-resolved simulation compared to the fully resolved simulation and approximately same as that for the case from Kida et al. (1991). However a shift in time between the two plots still remains.

Contour plots of vorticity magnitude on the symmetry plane at various times from Kida et al. (top) and the under-resolved simulation using the spectral code (bottom) are presented in figure 5.5. Up to figure 5.5(c) the contour plots from both the results match closely. After this time the contour plots from the two simulations, although qualitatively similar begin to differ slightly from each other. In 5.5(e) the contour plot from Kida et al. (1991) contains some jagged contour lines and spurious vorticity away from the vortex rings indicating possible aliasing errors.

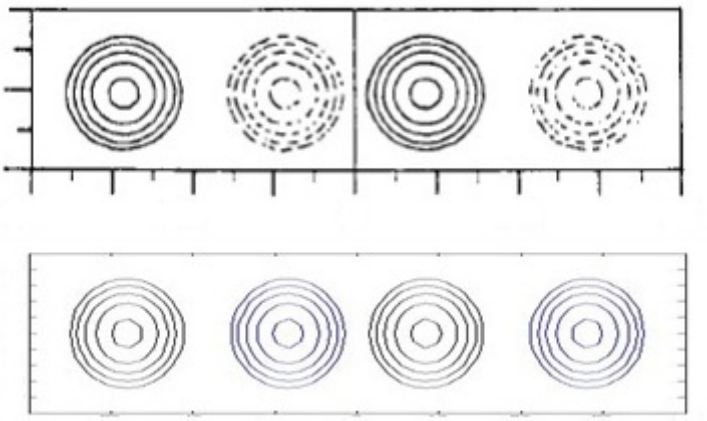

Figure 5.5: (a) $t = 0.0R_0^2/\Gamma_0$

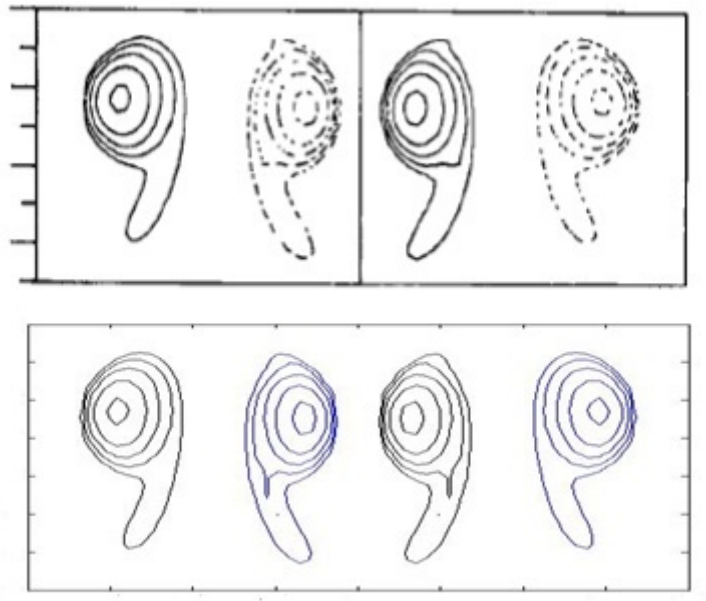

Figure 5.5: (b) $t = 11.96R_0^2/\Gamma_0$

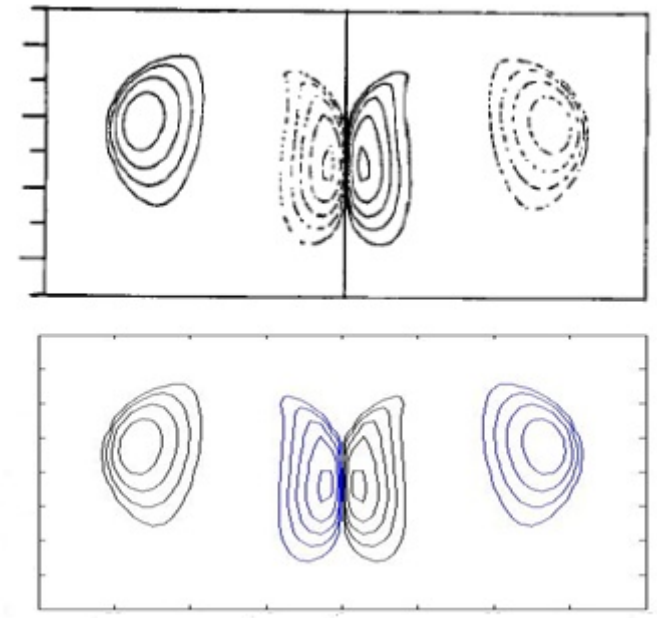

Figure 5.5: (c) $t = 35.87R_0^2/\Gamma_0$

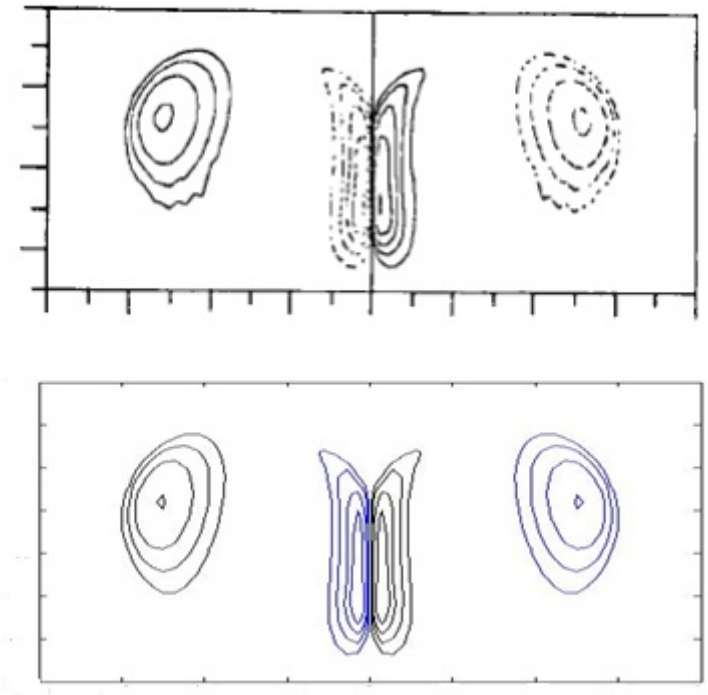

Figure 5.5: (d) $t = 41.85R_0^2/\Gamma_0$

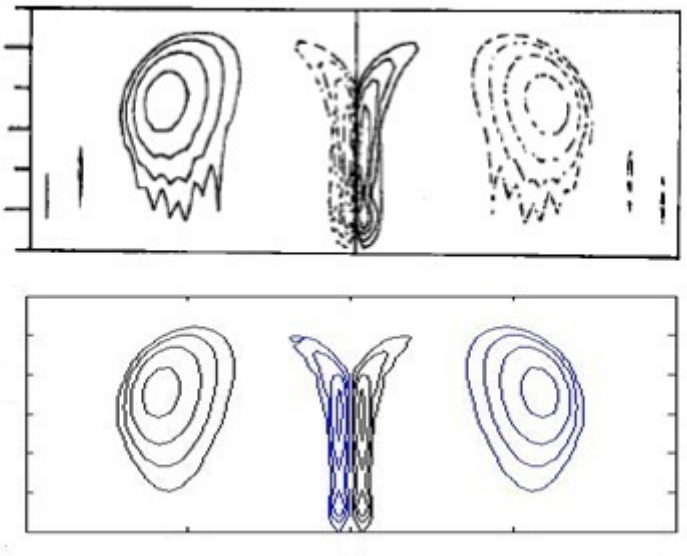

Figure 5.5: (e) $t = 47.83R_0^2/\Gamma_0$

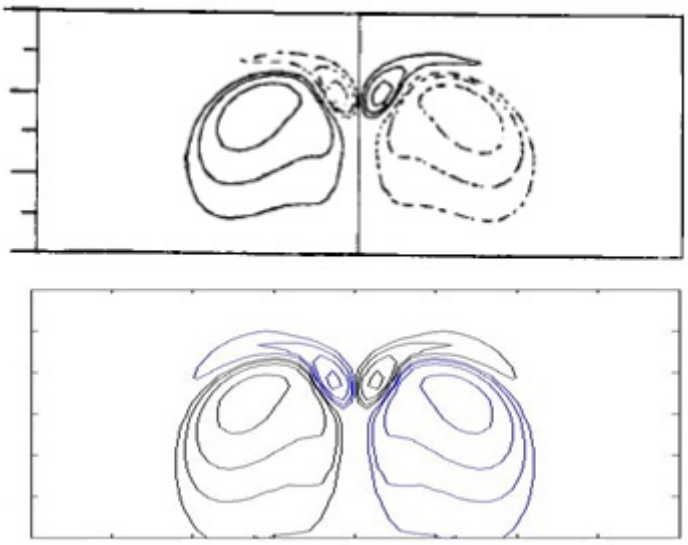

Figure 5.5: (f) $t = 71.74R_0^2/\Gamma_0$

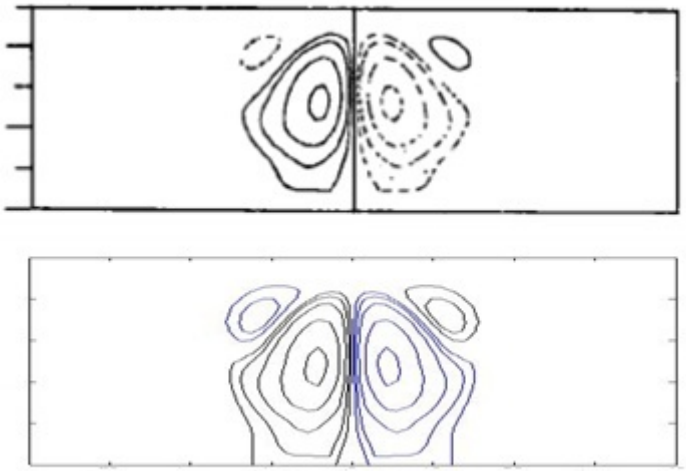

Figure 5.5: (g) $t = 89.67R_0^2/\Gamma_0$

Figure 5.5: Contours of vorticity on the symmetry plane from Kida et al. (1991) (top, solid and dashed lines are used to denote positive and negative vorticity) and the under-resolved alternate spectral code simulation (bottom, black and blue lines are used to denote positive and negative vorticity) at different times. The contour levels used are 5, 10, 20, 40 and 80 % of the maximum vorticity at the time.

5.3 Conclusions

The numerical study of vortex ring collision and reconnection performed by Kida et al. (1991) was used for a validation study. Although qualitatively similar, there are quantitative differences between the simulation performed using the finite difference code CGLES and Kida et al. (1991).

A simulation of the same vortex ring collision problem was performed using a spectral DNS code. The histories of the maximum vorticity on the symmetry and collision planes were found to be in excellent agreement with the simulation performed using CGLES proving a strong validation of the numerical approach used for simulating vortex ring reconnection.

A spatially under-resolved simulation using the same number of collocation points as in Kida et al. (1991) was performed using the spectral DNS code. The histories of the maximum vorticity on the symmetry and collision planes were in reasonable agreement with Kida et al. (1991). The main reason for the discrepancy between Kida et al. (1991) and the fully resolved simulations using CGLES and the spectral DNS code was therefore shown to be the under-resolution of the former set of simulations.

Chapter 6

Vortex ring reconnection with non-deformable surface

DNS of impingement of a vortex ring on a non-deformable, free-slip surface at an oblique angle of incidence leading to vortex reconnection is presented in this chapter. In section 6.1, the numerical approach used and the initial setup used in this chapter is outlined. In section 6.2 an assessment of the numerical approach is provided. In section 6.3, the results of the simulation of a vortex ring reconnection at $Re = 2000$ capturing the characteristic features discussed in the literature are presented. The effect of viscosity on the reconnection process is investigated in section 6.4. The special features of vortex reconnection occurring at high Reynolds numbers are described in section 6.5. In section 6.6, a simulation of vortex ring interaction with a free-slip surface at $Re = 7500$ leading to reconnection and subsequent breakdown of the reconnected vortex ring structure into a turbulent-like flow is presented. The conclusions from the chapter are summarised in section 6.7.

6.1 Numerical approach

The simulations were carried out in a cuboidal domain with dimensions $L_x \times L_y \times L_z$ along the Cartesian coordinate directions x, y, and z respectively. The initial setup consisted of a vortex ring of radius R_0 and circulation Γ_0 with its centre located at $(0, 0, -h)$ where h is the initial depth of the vortex ring below the surface, $z = 0$ (Figure 6.1). The axis of the vortex ring was initially directed at an angle γ to the horizontal. It moves under its self-induced velocity towards the surface and interacts with it at an oblique angle of incidence. A free-slip boundary condition was imposed on the $z = 0$ and $z = -L_z$ surfaces. A periodic boundary condition was used in the y-axis direction.

Using a periodic boundary condition in the x direction would lead the vortex ring to encounter its own wake. To avoid this the numerical approach used in the study of classical vortex rings in unbounded flow (section 4.1), of performing the computations with respect to a comoving reference frame, is used here as well. In the present case however, the reference frame moves only along the x direction along with the vortex ring.

The location of the vortex ring along the x-axis with respect to the comoving reference frame was calculated as

$$X(t) = \frac{1}{2\Omega} \int_V x\omega^2 \mathrm{d}V \tag{6.1}$$

where Ω is the total enstrophy. The integral-proportional controller described in section 4.1.1 was used to compute the time-dependent velocity of the comoving reference frame required to maintain $X(t)$ close to the target location $X_c = 0$, ensuring that the vortex ring remained close to the center of the reference frame. The velocity of the reference frame was used to set uniform inflow boundary condition at the $x = L_x/2$ boundary.

Irrotationality of the inlet flow was enforced by applying the boundary conditions $\partial v/\partial x = \partial w/\partial x = 0$ at the inlet $x = L_x/2$. At the outlet boundary $x = -L_x/2$, linear gradient conditions, $\partial u/\partial x = \partial v/\partial x = \partial w/\partial x = 0$ were imposed.

The core of the vortex ring was initialised with a Gaussian distribution of vorticity and the initial velocity field was obtained using the vector stream function method outlined in section 4.1.2.

6.1.1 Simulation parameters

Three sets of numerical simulations of the reconnection of vortex rings with a free-slip surface were performed using the initial setup outlined in section 6.1.

In set I, the reconnection of a thin cored, Gaussian initialised vortex ring with an initial slenderness ratio $\delta_0/R_0 = 0.2$, an initial inclination $\gamma = 5°$ and located at an initial depth of $h = 2.0R_0$ was considered. A thin cored vortex ring propagating at a shallow angle of inclination towards the surface was chosen so that the initial readjustment of the ring is complete before the interaction with the surface begins. The simulations were performed at varying Reynolds numbers 500, 1000, 2000, 3000, 4000, 5000, 6000, 8000 and 10000 in order to study the effect of viscosity on reconnection. The domain side lengths were $L_x = 8R_0$, $L_y = 8R_0$ and $L_z = 4R_0$. The numerical resolution of the grids in which the simulations at each Reynolds number were performed are listed in table 6.1. At $Re = 3000$ and 6000, the simulations were performed on two different grids.

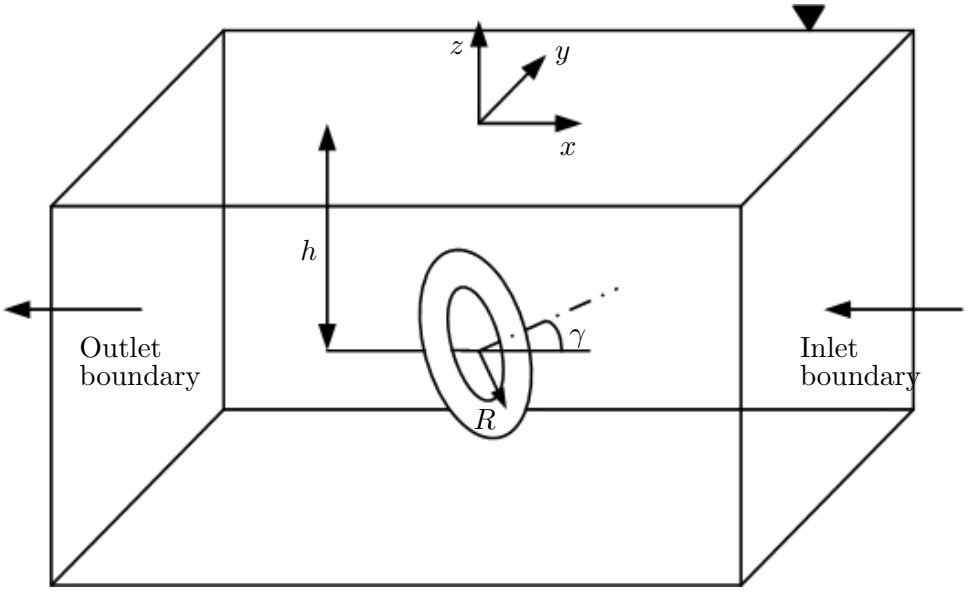

Figure 6.1: Schematic of the computational domain with the initial setup for the simulation of vortex ring reconnection with the surface ($z = 0$).

In set II, simulations of three Gaussian initialised rings initially located at an initial depth of $h/R_0 = 2.0$ with an initial inclination $\gamma = 5°$ with different initial slenderness ratios δ/R_0 =0.2, 0.3 and 0.4 were performed at $Re = 3000$. The results from this set were used to obtain the dependence of the rate of the circulation transfer process that occurs during the reconnection (described in section 6.3) on the core size of the vortex ring at a constant Reynolds number. This defined the scaling for the reconnection time.

In set III, the simulation of a Gaussian initialised vortex ring with an initial slenderness ratio $\delta_0/R_0 = 0.3$, located at an initial depth $h/R_0 = 3.0$ and initial inclination of $\gamma = 7°$ was performed at $Re = 7500$. The purpose of this simulation was to study the long time evolution of the flow after the completion of the initial reconnection of the vortex ring with the surface. The bridges of surface-normal vorticity formed during the first reconnection (described in section 6.3) propagate away from the symmetry plane. So in order to allow the flow evolution for a long time after the first reconnection, the width of the computational domain along the $y-$axis direction needs to be large enough that the vortex ring is sufficiently far away from the periodic boundaries throughout the simulation. Therefore a domain size of $12R_0 \times 12R_0 \times 6R_0$ (along x, y, z directions) was used for this simulation with $1152 \times 1152 \times 576$ grid points.

For all the simulations discussed in this chapter, the timestep was chosen, such that the maximum value of the Courant-Freidrichs-Lewy (CFL) number across the grid remained below 0.20 throughout.

	Number of cells	
Re	Grid 1	Grid 2
500	$768 \times 768 \times 384$	–
1000	$768 \times 768 \times 384$	–
2000	$768 \times 768 \times 384$	–
3000	$768 \times 768 \times 384$	$1024 \times 1024 \times 512$
4000	$1024 \times 1024 \times 512$	–
5000	$1024 \times 1024 \times 512$	–
6000	$1024 \times 1024 \times 512$	$1280 \times 1280 \times 640$
8000	$1280 \times 1280 \times 640$	–
10000	$1280 \times 1280 \times 640$	–

Table 6.1: Grid resolutions used for the simulations at different Reynolds numbers from set I.

6.2 Assessment of numerical approach

6.2.1 Domain size

To study the influence of the periodic side boundaries at $y = \pm L_y/2$ and the free slip boundary at $z = -L_z$, additional simulations for the case from set I at $Re = 3000$ were performed in two different domains with dimensions $8R_0 \times 12R_0 \times 4R_0$ (wider along y direction) and $8R_0 \times 8R_0 \times 6R_0$ (deeper).

For the wider domain, the trajectory of the vortex ring (measured by the enstrophy averaged location of the vortex ring on the z-axis) and the history of the circulation of the interacting vortex core were nearly identical to the standard domain. However the vortex ring in the deeper domain simulation had a slightly different trajectory reaching the surface earlier (figure 6.2a). This is due to the fact that the surface at $z = -4R_0$

Domain depth (L_z)	$t_1\Gamma_0/R_0^2$	Γ_r/Γ_0	δ_r/R_0	$A_{\max}R_0^2/\Gamma_0^2$	T_R^*
$4R_0$	23.08	0.993	0.268	0.240	1.449
$6R_0$	19.92	0.993	0.260	0.254	1.455

Table 6.2: Vortex ring parameters at the beginning of circulation transfer and non-dimensional reconnection time (T_R^*) for $Re = 3000$ from set I at the two different domain depths. The two values of T_R^* differ by less than 0.4%.

in the standard domain influences the early trajectory of the vortex ring causing it to propagate towards the surface at a shallower angle.

The focus of the present work is the rate of transfer of the circulation of the interacting vortex core to a direction normal to the surface during vortex reconnection (section 6.5, figure 6.6). Specifically the effect of Reynolds number on the reconnection timescale (defined based on the inverse of the peak value of the circulation transfer rate) is investigated in section 6.4. The decay of the circulation of the interacting vortex core during reconnection for the two domains is seen in figure 6.2(b). Since the vortex ring reaches the surface earlier in the deeper domain, the circulation transfer begins earlier for that case. As a result the vortex ring parameters at the beginning of the circulation transfer is slightly different for the two domains.

In section 6.4.1, a non-dimensional reconnection time T_R^* (6.9) which accounts for the variable ring geometry at the beginning of the circulation transfer is introduced. In table 6.2 the times at which the circulation transfer begins (t_1), the circulation (Γ_r) and core radius (δ_r) at t_1 and the peak values of the circulation transfer rate ($A_{\max}$) for the simulations using the two domain sizes are listed (see section 6.4.1 for details on determining these quantities). The values of the non-dimensional reconnection times (T_R^*) computed using these values for the two domains are also listed and found to differ by less than 0.4%.

Thus it is shown that increasing the domain depth has a negligible effect on the non-dimensional reconnection time which is the quantity of interest for this study.

6.2.2 Numerical resolution

The adequacy of the numerical resolution was checked for the case from set I with $Re = 5000$ by tracking the energy balance between the volume integrated kinetic energy per unit mass with respect to the co-moving reference frame K, the volume integrated rate of kinetic energy dissipation ϵ_K and the total volume integrated kinetic energy flux out of the domain F_K (see section 4.3.1 for details) given by

$$-\frac{\mathrm{d}K}{\mathrm{d}t} = \epsilon_K + F_K$$

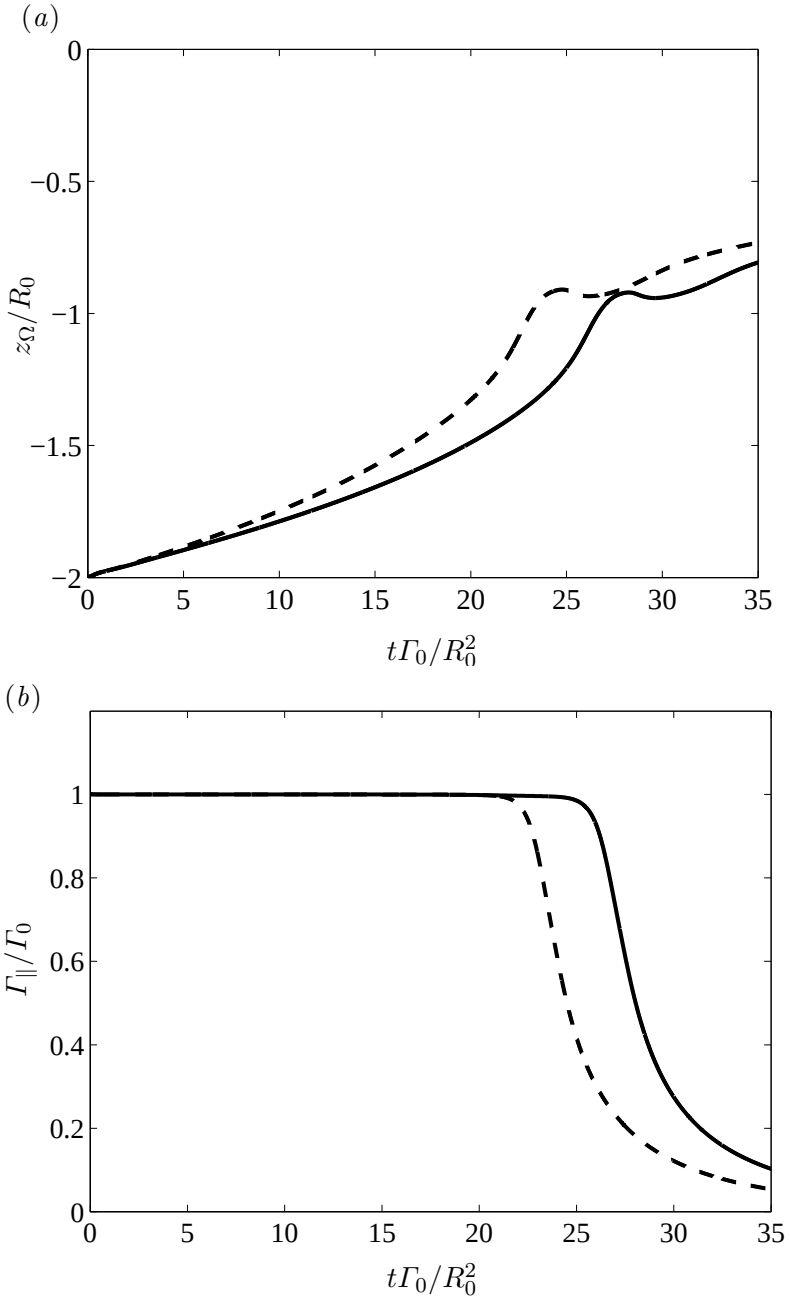

Figure 6.2: (a) Trajectories of the vortex rings (b) History of the magnitude of the circulation of the interacting vortex core on the symmetry plane $y = 0$ for the case from set I with $Re = 3000$ in the standard domain (solid) and deep domain (dashed).

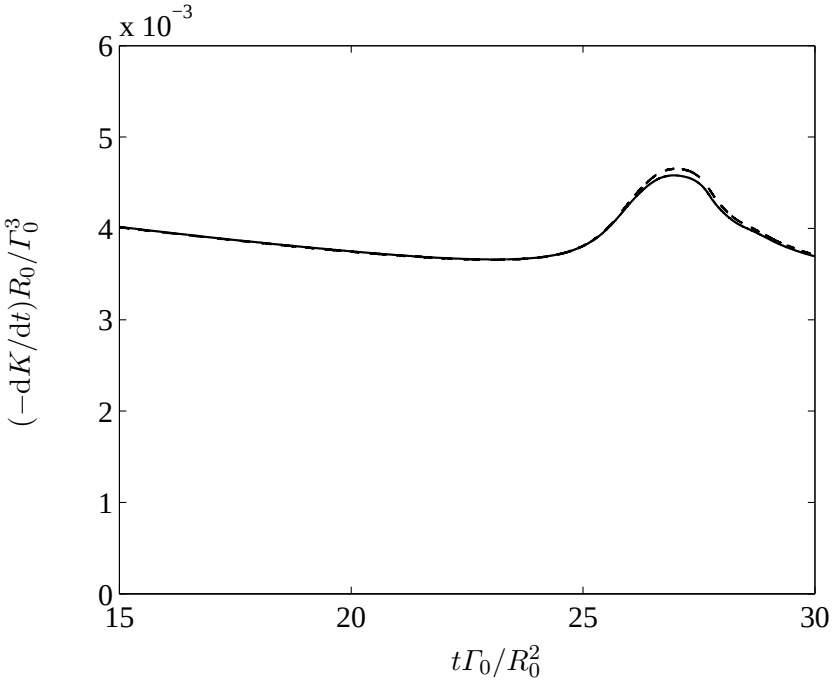

Figure 6.3: Comparison of histories of - - - - Rate of decrease of volume-integrated kinetic energy $(-\mathrm{d}K/\mathrm{d}t)$ and ——— Sum of volume-integrated rate of dissipation and energy flux $(\epsilon_K + F_K)$ for the case from set I with $Re = 5000$.

The volume integrated enstrophy, Ω, given by

$$\Omega = \frac{1}{2}\iiint_V |\omega|^2 \mathrm{d}V \tag{6.2}$$

is related to the dissipation according to $2\nu\Omega \simeq \epsilon_K$ (Bobyleff-Forsythe formula, Serrin 1959). The peaks of ϵ_K correspond to times when intense stretching of vortex filaments occurs leading to a rapid growth of enstrophy and dissipation and generation of fine scale structures testing the spatial resolution of the grid. Therefore the resolution needs to be sufficiently fine to keep the difference between the two sides of the energy balance equation negligibly small at the enstrophy peaks.

Figure 6.3 compares the histories of the quantities represented by left and right hand sides of (6.2) for the case from set I with $Re = 5000$. The difference between the two sides is less than $8 \times 10^{-5}\Gamma_0^3/R_0$ over the entire simulation reaching the maximum value at the dissipation peak demonstrating that the spatial discretisation error is negligible throughout. For all the simulations in this chapter, the difference between the two sides of the energy balance equation remained at most 4% at the dissipation peaks but usually significantly less.

The simulations from set I at $Re = 3000$ and 6000 were performed on two different grids. As an additional test of the spatial resolution, the histories of the maximum vorticity on the symmetry plane $(y = 0)$ associated with the interacting vortex core obtained from

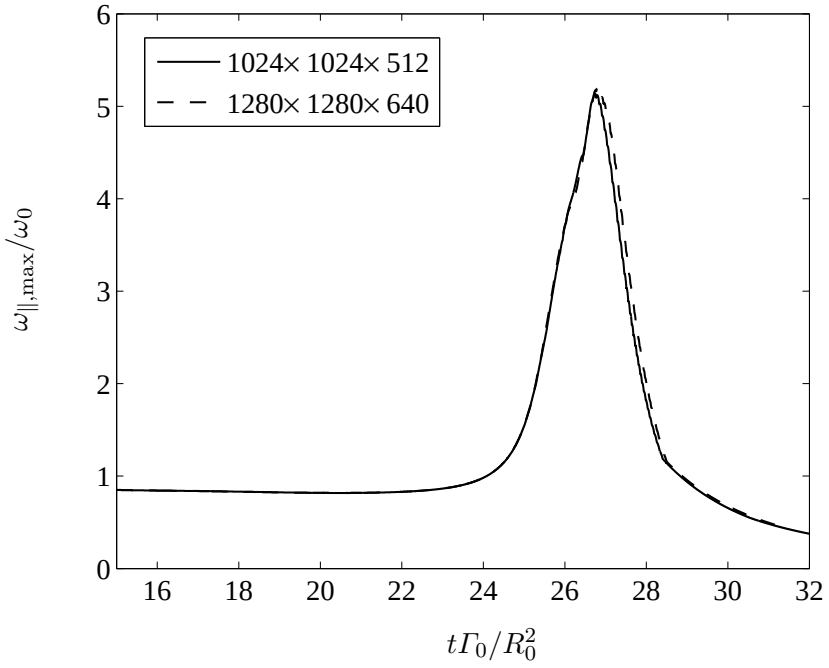

Figure 6.4: Comparison of the histories of the maximum vorticity on the symmetry plane ($\omega_{\parallel,\max}$) normalised by the maximum value at $t = 0$ (ω_0) for the case from set I with $Re = 6000$ obtained using grids with $1024 \times 1024 \times 512$ (solid) and $1280 \times 1280 \times 640$ (dashed) points.

simulations performed on the two grids were compared (at both Reynolds numbers). Figure 6.4 shows the comparison for $Re = 6000$. The intensification of vorticity occurs due to the out-of-plane stretching of the vortex core during reconnection. The histories of the maximum vorticity nearly overlap until the peak of the vortex stretching process is reached on the coarser grid. On the finer grid, the stretching proceeds slightly longer before the peak value is reached. The difference between the peak values on the two grids is approximately 1.2% of the value on the finer grid. The difference between the peak values for the two grids on which the case with $Re = 3000$ was performed is less than 1%. Note that the maximum vorticity on the symmetry plane is a sensitive measure of the grid resolution.

6.3 Vortex ring reconnection at Re=2000

The simulation of the case from set I with $Re = 2000$ is used to describe the characteristic features of vortex ring reconnection.

After initialisation, the vortex ring translates under its self-induced velocity towards the surface (figure 6.5(a)). Since a Gaussian vorticity profile is used as the initial condition, the vortex ring undergoes a readjustment. For the Gaussian initialised vortex ring with an initial slenderness ratio of $\delta_0/R_0 = 0.2$ in unbounded flow, the time required for the

completion of the initial readjustment was determined to be approximately $18R_0^2/\Gamma_0$ in a separate simulation using the numerical approach outlined in chapter 4.

The ring reaches close to the surface at $t \simeq 25R_0^2/\Gamma_0$ and begins to be influenced by the image vortex ring implied by the free-slip boundary condition. The influence of the image vortex ring causes the section of the vortex ring close to the surface to bend back. As the vortex ring collides with the surface, the vortex core is flattened against it (figures 6.5(b),(c)). The near-surface vortex filaments disconnect from each other and simultaneously reconnect with the surface. The reconnected vortex filaments accumulate to form two vortices on either side of the symmetry plane, $y = 0$ (see figure 6.5(d)) referred to as 'bridges' (Melander and Hussain, 1989). The non-reconnected vortex filaments directed along the y-axis direction are referred to as 'threads' (see figure 6.5(d)). The bridges of surface-normal vorticity move parallel to the surface away from the symmetry plane due to their self-induced velocity (figure 6.5(e)). The threads are continuously wound at either end around the bridges.

Within $t \simeq 45R_0^2/\Gamma_0$, 95% of the circulation of the upper limb of the vortex ring is transferred to the surface normal direction. However, the reconnection process does not go to completion and a small remnant of the original circulation is present in the form of a vortex sheet even in the late stage of the reconnection. Simultaneously the bottom part of the vortex ring also advects towards the surface and when it collides with the surface a second vortex reconnection begins. In this section the first reconnection is the focus of the discussion.

The interaction of the vortex ring with the non-deformable free-slip surface can be understood as an interaction with an image vortex ring leading to reconnection. The topology of this reconnection process is depicted in figure 6.6(a). As the filaments of the vortex ring and its image with oppositely-signed vorticity overlap in the region of interaction, viscous diffusion leads to their annihilation. The disconnected filaments simultaneously reconnect with the disconnected filaments from the image vortex ring. The evolution of the circulation of the filaments from the vortex ring undergoing disconnection which are directed parallel to the surface ($\Gamma_\parallel$) and the circulation of the reconnected filaments directed normal to the surface ($\Gamma_\perp$) is shown in figure 6.6(b). The magnitude of the former decreases with time and the latter increases with time while the sum is conserved (neglecting the small amount of circulation shed into the wake). This circulation transfer to an orthogonal direction is the key characteristic of the phenomenon of vortex reconnection.

$$\Gamma_\parallel + \Gamma_\perp = \Gamma_0' \tag{6.3}$$

where $\Gamma_\parallel$ is the circulation (absolute value) associated with the interacting vortex core on the symmetry plane $y = 0$, $\Gamma_\perp$ the circulation (absolute value) at the surface ($z = 0$)

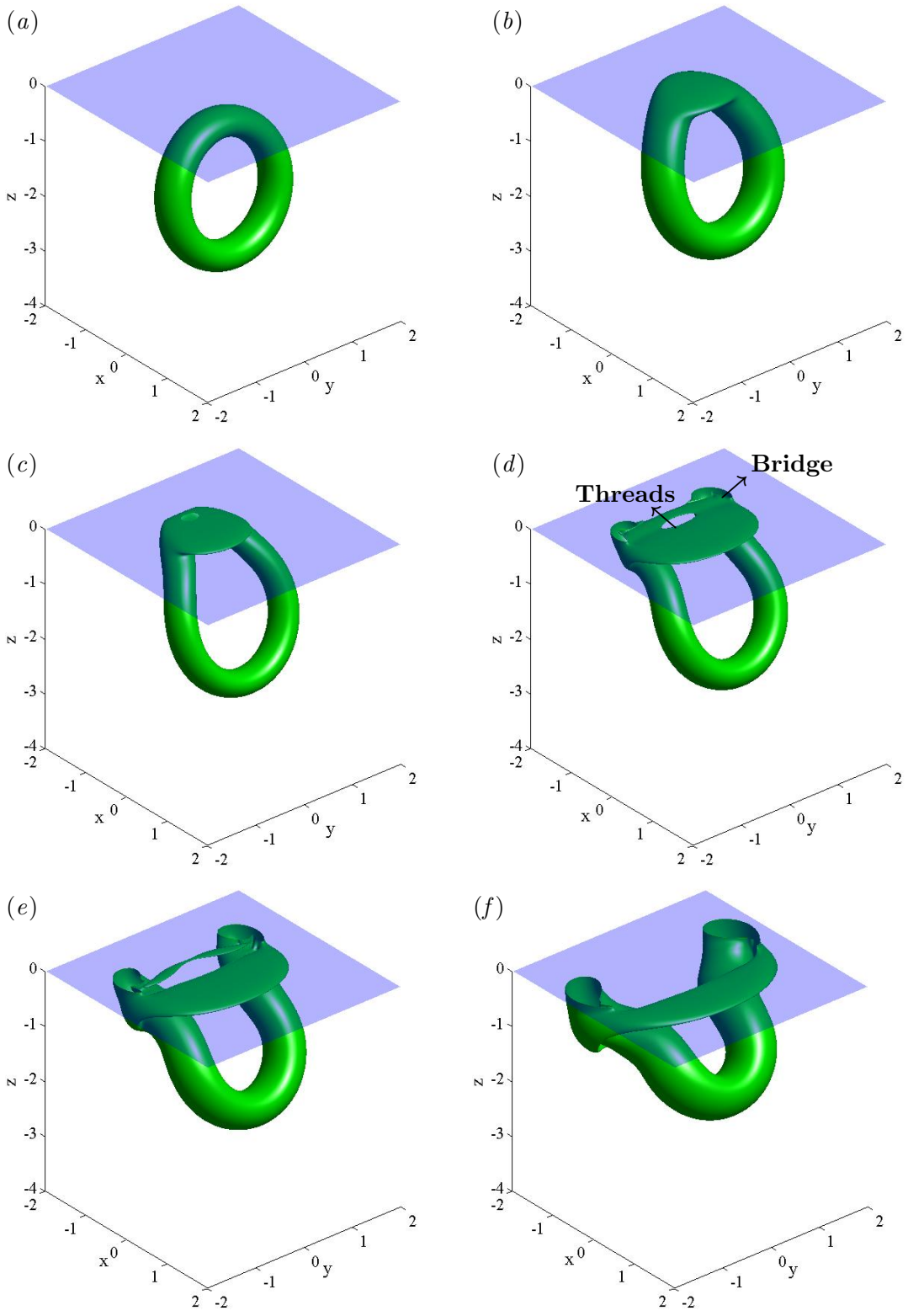

Figure 6.5: Isosurfaces of vorticity magnitude ($|\omega| = 0.3|\omega_{\max}|$) showing the different stages of vortex reconnection for the case from set I with $Re = 2000$ at $t =$ (a) 15.0 (b) 25.5 (c) 27.0 and (d) 30.0 (e) 32.0 (f) 34.0 R_0^2/Γ_0.

on the half-plane $y > 0$ and Γ_0' the circulation of the vortex ring after its readjustment after initialisation. The evolution of $\Gamma_\parallel$ and $\Gamma_\perp$ with time during the reconnection is shown in figure 6.6(c). The rate of transfer of circulation can be derived as follows.

The Helmholtz equation for the surface-parallel vorticity on the symmetry plane $\omega_y(x, y = 0, z)$ is written as (since $\omega_x = \omega_z = 0$ on the symmetry plane)

$$\begin{aligned}
\frac{\partial \omega_y}{\partial t} + u\frac{\partial \omega_y}{\partial x} + v\frac{\partial \omega_y}{\partial y} + w\frac{\partial \omega_y}{\partial z} &= \omega_y\frac{\partial v}{\partial y} + \nu\nabla^2\omega_y \\
\implies \frac{\partial \omega_y}{\partial t} + \frac{\partial (u\omega_y)}{\partial x} + \frac{\partial (v\omega_y)}{\partial y} + \frac{\partial (w\omega_y)}{\partial z} &= \omega_y\frac{\partial v}{\partial y} + \nu\nabla^2\omega_y \ (\because \nabla.\boldsymbol{u} = 0) \\
\implies \frac{\partial \omega_y}{\partial t} + \frac{\partial (u\omega_y)}{\partial x} + \cancel{v\frac{\partial \omega_y}{\partial y}} + \frac{\partial (w\omega_y)}{\partial z} &= \nu\nabla^2\omega_y \ (\because v|_{y=0} = 0)
\end{aligned}$$

Integrating over the entire symmetry plane $x : -\infty$ to ∞, $z : -L_z$ to 0

$$\begin{aligned}
\iint \frac{\partial \omega_y}{\partial t} dxdz \ + \ \iint \frac{\partial (u\omega_y)}{\partial x} dxdz + \iint \frac{\partial (w\omega_y)}{\partial z} dxdz &= \iint \nu\nabla^2\omega_y dxdz \\
\implies \frac{\mathrm{d}\Gamma_\parallel}{\mathrm{d}t} \ + \ \cancel{\int (u\omega_y)\Big|_{-\infty}^{\infty}} dz + \cancel{\int (w\omega_y)\Big|_{-L_z}^{0}} dx &= \iint \nu\nabla^2\omega_y dxdz \\
\implies \frac{\mathrm{d}\Gamma_\parallel}{\mathrm{d}t} &= \iint \nu\left(\frac{\partial^2\omega_y}{\partial x^2} + \frac{\partial^2\omega_y}{\partial z^2}\right) dxdz \ \left(\because \left.\frac{\partial^2\omega_y}{\partial y^2}\right|_{y=0} = 0\right) \\
\implies \frac{\mathrm{d}\Gamma_\parallel}{\mathrm{d}t} &= \nu\cancel{\int \frac{\partial \omega_y}{\partial x}\Big|_{-\infty}^{\infty}} dz + \nu\int \left.\frac{\partial \omega_y}{\partial z}\right|_{-L_z}^{0} dx \\
\implies \frac{\mathrm{d}\Gamma_\parallel}{\mathrm{d}t} &= \nu\int \left.\frac{\partial \omega_y}{\partial z}\right|_{y=0,z=0} dx \ (\because \text{ ring away from } z = -L_z)
\end{aligned}$$

Also,

$$\begin{aligned}
\implies \frac{\mathrm{d}\Gamma_\parallel}{\mathrm{d}t} &= \nu\left[\int \left.\frac{\partial^2 u}{\partial z^2}\right|_{y=0,z=0} dx - \cancel{\frac{\partial w}{\partial z}\Big|_{-\infty}^{\infty}}\right] \\
\implies \frac{\mathrm{d}\Gamma_\parallel}{\mathrm{d}t} &= \nu\int \left.\frac{\partial^2 u}{\partial z^2}\right|_{y=0,z=0} dx \qquad (6.4)
\end{aligned}$$

Similarly by writing the Helmholtz equation for the surface-normal vorticity on the free-slip surface $\omega_z(x, y, z = 0)$ and integrating over the half-plane $x : -\infty$ to ∞, $y : 0$ to $L_y/2$, $z = 0$ it can be shown that

$$\frac{\mathrm{d}\Gamma_\perp}{\mathrm{d}t} = \nu \iint \left.\frac{\partial^2 \omega_z}{\partial z^2}\right|_{z=0} dxdy$$

$$\implies \frac{\mathrm{d}\Gamma_\perp}{\mathrm{d}t} = \nu \int \left.\frac{\partial^2 u}{\partial z^2}\right|_{y=0,z=0} dx \tag{6.5}$$

Therefore from (6.4) and (6.5) the absolute rate of change of the two circulation quantities is shown to be equal. The rate of transfer of circulation is given by a line-integral along the projection of the symmetry plane ($y = 0$) at the surface ($z = 0$).

$$\frac{\mathrm{d}\Gamma_\parallel}{\mathrm{d}t} = -A, \frac{\mathrm{d}\Gamma_\perp}{\mathrm{d}t} = A$$

$$A = \nu \int_x \left.\frac{\partial \omega_y}{\partial z}\right|_{z=0,y=0} \mathrm{d}x \tag{6.6}$$

The contours of ω_y (vorticity along surface-parallel direction) on the symmetry plane $y = 0$ (figures 6.7(a)–6.7(d)) show the evolution of the interacting vortex core during reconnection. Figure 6.8 shows the evolution of the maximum vorticity on the symmetry plane. The simultaneous evolution of the rate of transfer of circulation, A is shown in figure 6.9.

The vorticity maximum decreases during the translation of the vortex ring towards the surface due to the diffusion of the vortex core. When the vortex ring encounters the surface, the interacting vortex core gets deformed. The vorticity gradient exposed at the surface causes the beginning of the circulation transfer (figure 6.7(b)). Due to the induced velocity of the image vortex ring, the interacting vortex core propagates in the $-x$ direction as the upper part of vortex ring bends backwards. The strain-field acting on the vortex core due to the influence of the vortex ring and its image compresses it along the z-direction and extends it along the x-direction. During this process, the vortex core deforms into the 'head-tail' structure described in the literature (Kida et al., 1991). The in-plane strains along the x and z directions ($\partial u/\partial x$, $\partial w/\partial z$) are balanced by an out-of-plane strain normal to the symmetry plane ($\partial v/\partial y$) stretching the vortex filaments (directed along the y-direction) and intensifying the vorticity within the vortex core.

Due to the flattening of the vortex core and the stretching of the vortex filaments, the vorticity gradient at the surface and consequently the circulation transfer rate rise sharply. The vorticity maximum on the symmetry plane and the circulation transfer rate reach peak values at $t \simeq 28.0 R_0^2/\Gamma_0$. Subsequently, viscous diffusion becomes dominant

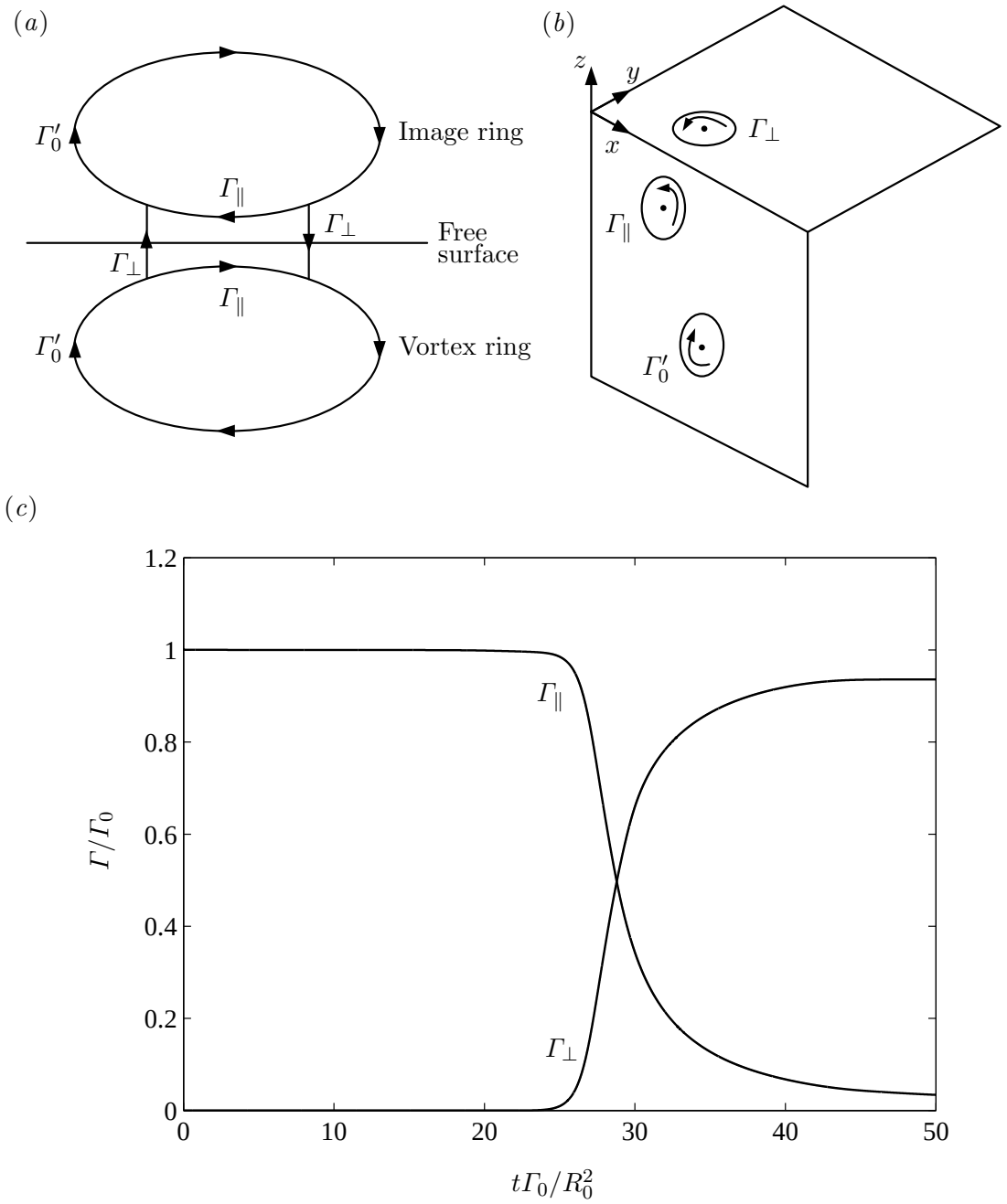

Figure 6.6: (a) Topology of the reconnection due to the collision of a vortex ring with its image. (b) Symmetry plane ($y = 0$) and half-plane at the surface ($z = 0, y > 0$) showing the two measured circulations. (c) Evolution of the surface-parallel and surface-normal circulations (normalized by Γ_0) with non-dimensional time for the case from set I with $Re = 2000$.

limiting the flattening of the vortex core and the vorticity maximum and the circulation transfer rates begin to decline. It is due to this process of flattening and stretching that the circulation transfer occurs within a time period much shorter than a viscous timescale (δ^2/ν). It also indicates the possibility that, as the Reynolds number increases, the core stretching and flattening process could intensify, effectively keeping the reconnection timescale roughly constant. The dependence of the reconnection timescale on the Reynolds number is investigated in section 6.4.

The period of rapid enstrophy growth in figure 6.3 (corresponding to the rapid growth of dissipation) is associated with this process of vortex core stretching. In the present case, the maximum vorticity within the core increases to nearly 1.6 times its initial maximum (figure 6.8). The peak value attained by the vorticity maximum on the symmetry plane provides a measure of the fineness of the vortex core at the peak of the vortex core flattening. Therefore the convergence of the peak value provides a sensitive measure for the adequacy of the grid resolution (as used in section 6.2).

6.4 Effect of viscosity on vortex ring reconnection

Viscous diffusion plays an essential part in effecting the circulation transfer during vortex reconnection. In this section, all the simulations from set I (section 6.1.1), with Reynolds number varying from 500 to 10000, are considered to investigate the effect of viscosity on the rate of the circulation transfer.

The reconnection time is a representative timescale within which the circulation transfer occurs. A reconnection time based on the inverse of the maximum value attained by the circulation transfer rate ($A_{\max}$) can be defined as

$$T_{R0} = \frac{\Gamma_0}{A_{\max}} \,. \tag{6.7}$$

However, since the vortex rings need to propagate over some distance before the interaction with the surface begins, both the circulation and the core size at the time when the reconnection begins are different from their initial values. Therefore the ring parameters at the beginning of the reconnection would be different for the different simulations in set I performed at varying Reynolds numbers. To study the variation of the reconnection time with Reynolds number alone its dependence on the changing ring parameters needs to be determined. The results of the simulations from set II (section 6.1.1) are used to determine this.

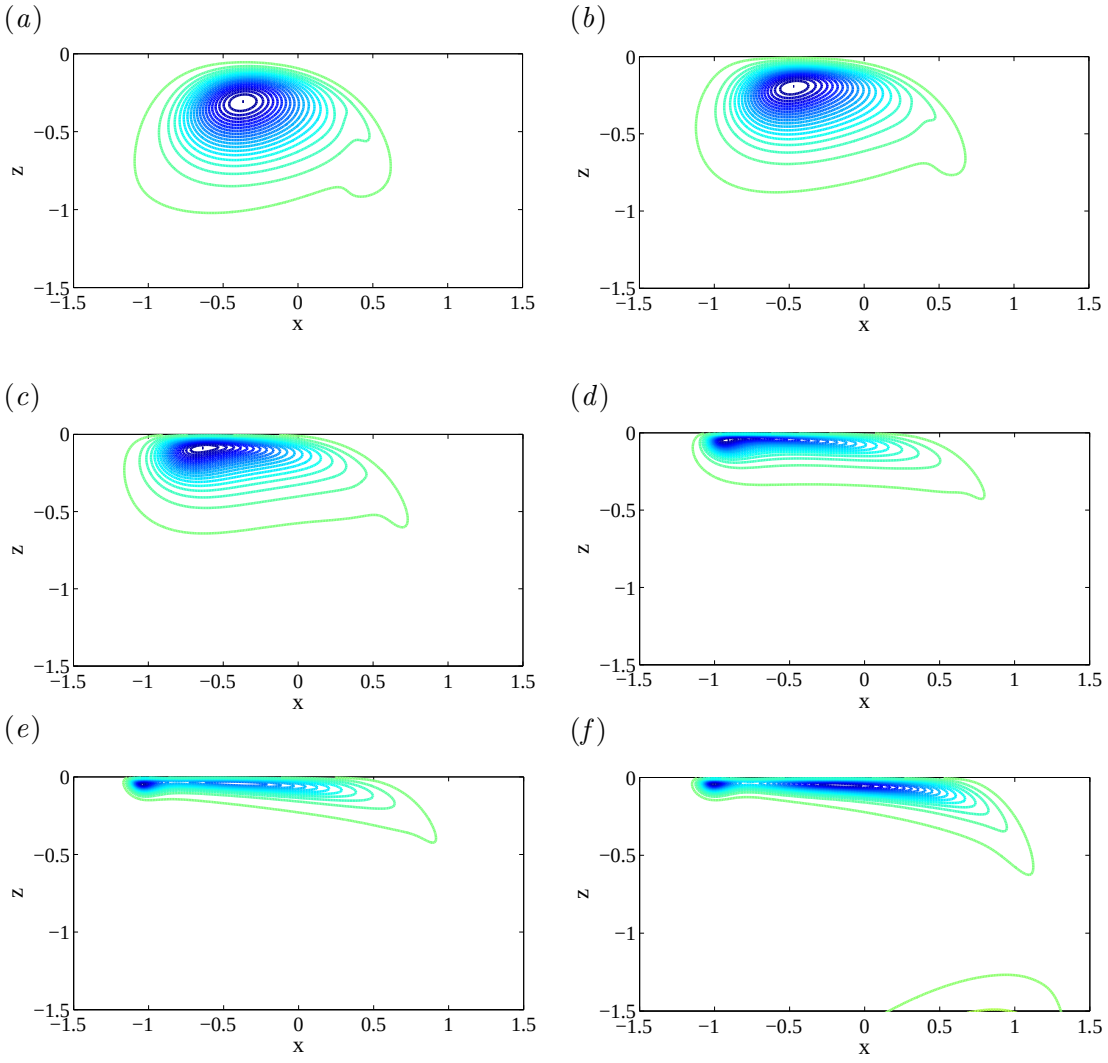

Figure 6.7: Contours of vorticity ($|\omega_y|$) on the symmetry plane ($y = 0$) for the case from set I with $Re = 2000$ at $t =$ (a) 20.0 (b) 23.0 (c) 25.5 (d) 27.0 (e) 28.5 and (f) 30.0 R_0^2/Γ_0. A lowest contour level of $|\omega_y|_{\max}/40$ and an equal spacing of $|\omega_y|_{\max}/20$ was used.

6.4.1 Effect of ring parameters on reconnection time at constant Re

All the simulations in set II were performed at a constant Reynolds number, $Re = 3000$. The vortex rings had different initial core sizes and would therefore also have different ring parameters at the beginning of the reconnection process. To account for this, the basic scaling law for the reconnection time is determined.

To determine the ring parameters appropriate for the beginning of reconnection the following method was used. For each simulation, an approximate beginning time for the circulation transfer process $t = t_1$ was defined as the time at which $\Gamma_\perp$ reaches an arbitrary value of $0.0001\Gamma_0$. The circulation, Γ_r and core radius, δ_r of the vortex ring at $t = t_1$ were obtained for a simulation of a vortex ring with the same initial

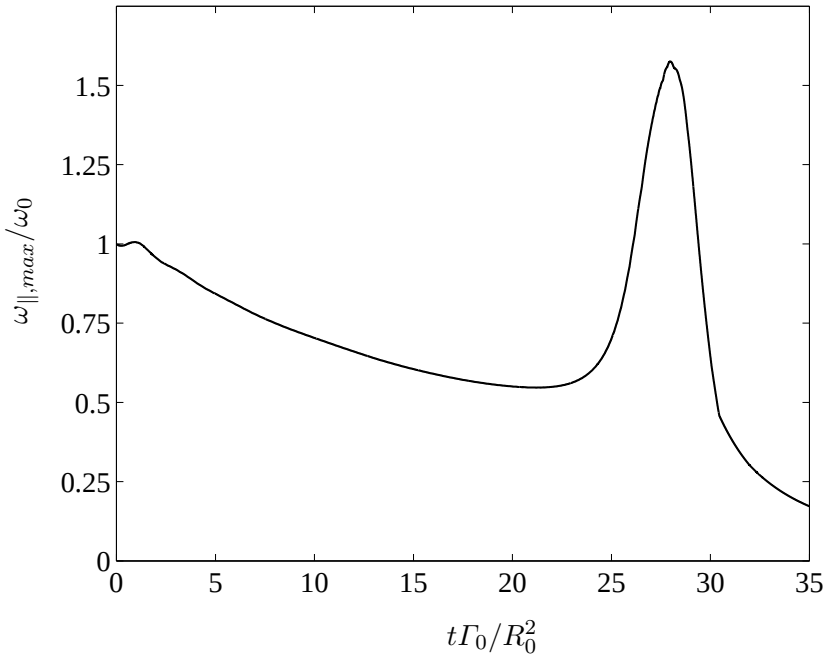

Figure 6.8: Evolution of the maximum vorticity on the symmetry plane ($\omega_{\parallel,max}$) normalised by the maximum value at $t = 0$ (ω_0) with non-dimensional time for the case from set I with $Re = 2000$.

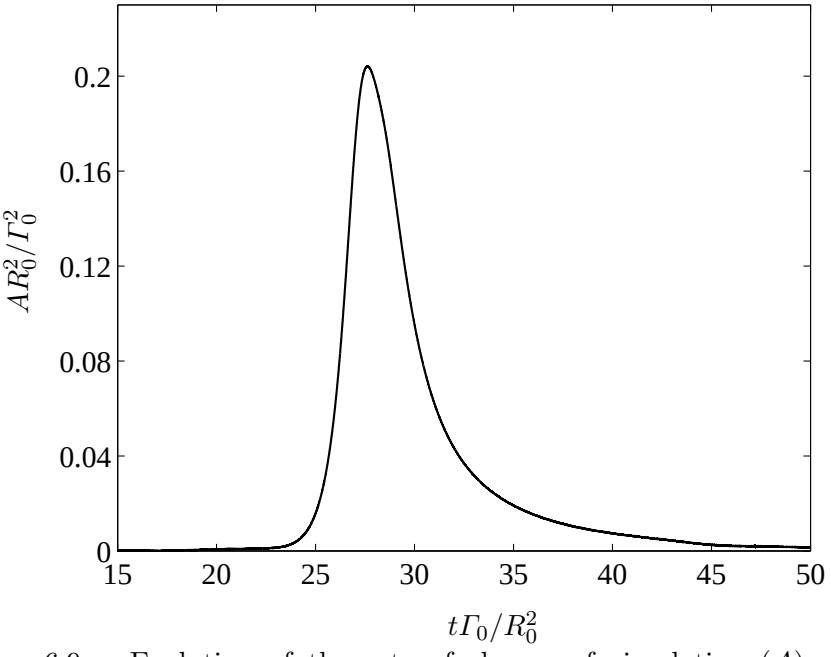

Figure 6.9: Evolution of the rate of change of circulation (A) with non-dimensional time for the case from set I with $Re = 2000$.

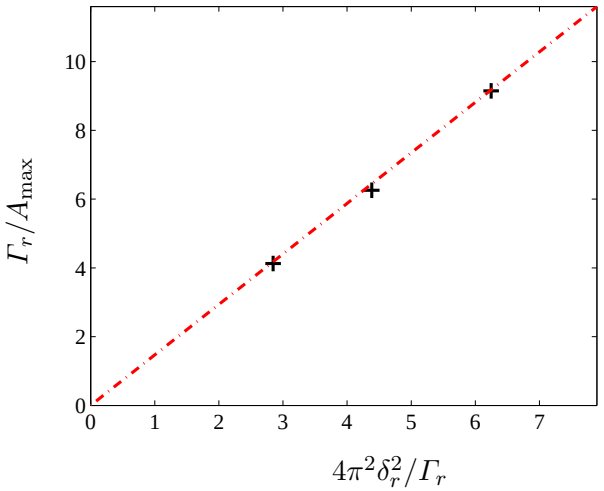

Figure 6.10: Scaling of reconnection time with inviscid timescale based on core radius and circulation. Red dashed line corresponds to the scaling $\Gamma_r/A_{\max} = 1.47(4\pi^2\delta_r^2/\Gamma_r)$

parameters translating in unbounded flow at the same Reynolds number. The numerical approach from chapter 4 was used for this simulation in unbounded flow. These values of circulation and core radius were used as the ring parameters at the beginning of the circulation transfer. Although the presence of the surface would affect the evolution of the vortex rings, Γ_r and δ_r provide reasonable estimates of the actual values.

The basic scaling law for the reconnection time is determined in the following way. For the three simulations in set II, the reconnection timescale $\Gamma_r/A_{\max}$ is plotted against an inviscid timescale $4\pi^2\delta_r^2/\Gamma_r$, based on the circulation and core radius. This inviscid timescale is the approximate time taken for the vortex ring core to rotate about its centre. From figure 6.10 it is seen that the scaling is approximately linear according to

$$\frac{\Gamma_r}{A_{\max}} = 1.47\left(\frac{4\pi^2\delta_r^2}{\Gamma_r}\right), \tag{6.8}$$

showing that the reconnection time scales on δ_r^2/Γ_r. This result is used to control the effect of different ring parameters at the beginning of reconnection and hence define a non-dimensional reconnection time

$$T_R^* = \frac{1}{A_{max}}\left(\frac{\Gamma_r^2}{4\pi^2\delta_r^2}\right), \tag{6.9}$$

appropriate for the ring geometry at the time of reconnection.

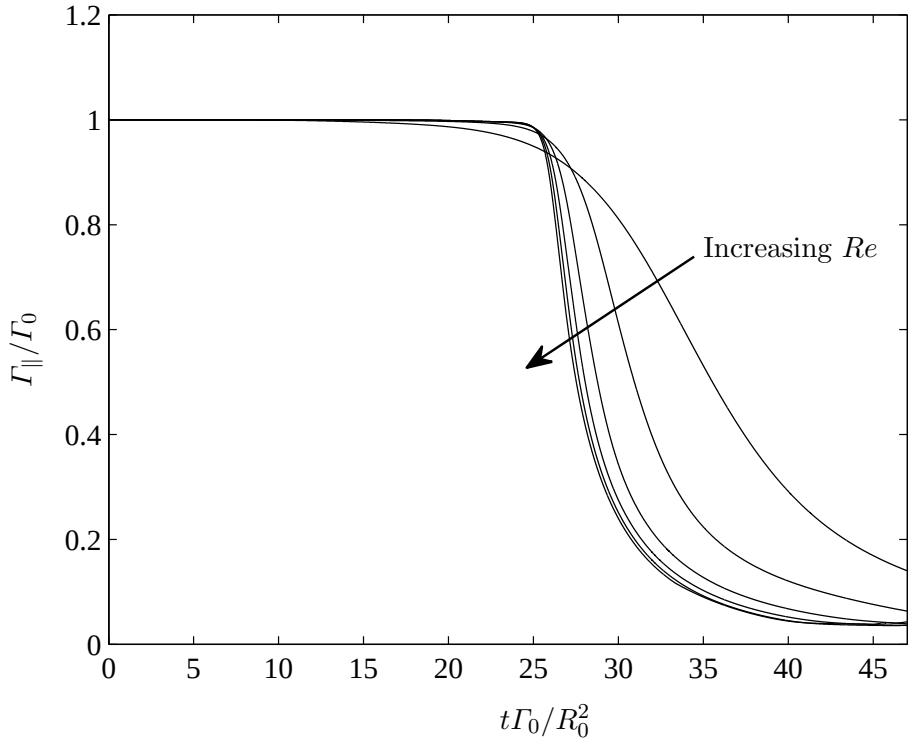

Figure 6.11: Evolution of the surface-parallel circulation on the symmetry plane (normalized by Γ_0) at $Re = 500, 1000, 2000, 3000, 40000, 5000$ for set I.

6.4.2 Effect of Re on reconnection time

The simulations from set I performed at varying Reynolds numbers are now considered. Figure 6.11 shows the variation of the circulation of the interacting vortex core on the symmetry plane for $Re = 500, 1000, 2000, 3000, 4000, 5000$. At lower Reynolds numbers the core size of the vortex ring grows faster due to viscous diffusion. Although this results in a slightly smaller propagation speed, the diffused core interacts with the surface earlier. The time at which the circulation transfer begins, increases with Reynolds number. The circulation transfer curves appear to nearly saturate for $Re \gtrsim 2000$.

To study the effect of Reynolds number on the circulation transfer rate, the non-dimensional reconnection time T_R^* was computed for each case using the procedure outlined in section 6.4.1. Table 6.3 lists the values of t_1, Γ_r and δ_r for the cases at the different Reynolds numbers.

Since the time before reconnection is different for the different cases in set I, the inclination of the vortex ring axis to the surface at the beginning of reconnection is also slightly different. The scaling (6.8) does not account for the effect of the inclination of the vortex ring axis to the surface. But since the initial inclination of the vortex rings is the same ($\gamma = 5°$) for all the cases in set I, the variation in inclination at the beginning of reconnection would be small, especially for the cases with $Re \gtrsim 1000$ for which the values of t_1 vary little.

Re	$t_1\Gamma_0/R_0^2$	Γ_r/Γ_0	δ_r/R_0
500	14.62	0.989	0.368
1000	20.12	0.988	0.335
2000	22.51	0.991	0.291
3000	23.08	0.993	0.268
4000	23.40	0.993	0.254
5000	23.52	0.993	0.244
6000	23.59	0.993	0.238
8000	23.67	0.993	0.229
10000	23.67	0.993	0.229

Table 6.3: Vortex ring parameters at the beginning of reconnection at different Re for set I.

Figure 6.12 shows the variation of the normalised reconnection time with Reynolds number. T_R^* decreases with Re at the low Reynolds numbers and reaches a minimum value for $Re \simeq 2000$. For $Re \gtrsim 2000$, the normalised reconnection time increases very slowly with increasing Reynolds number remaining nearly constant. The variation of the reconnection time T_{R0}, obtained from (6.7) without correcting for the ring parameters at the beginning of reconnection, is also shown for comparison. The effect of the non-dimensionalisation with respect to the ring parameters is to reduce the variation of the reconnection time at low Reynolds numbers. At high Reynolds numbers, since the values of Γ_r and δ_r do not vary much (from table 6.3), the correction does not alter the scaling greatly. The trend of the reconnection time remaining nearly constant at high Re obtains independent of whether the correction is applied.

The values of the non-dimensional reconnection time are $\mathcal{O}(1)$ at all the Reynolds numbers showing that the reconnection time is of the order of the time taken for the interacting vortex core to perform a rotation about its centre.

The near-saturation of the maximum of circulation transfer rate with increasing Reynolds number for $Re \gtrsim 2000$ implies that for high Reynolds numbers,

$$\begin{aligned} T_R^* &\sim \mathcal{O}(1) \\ \implies A = \nu \int_x \left(\left.\frac{\partial \omega_y}{\partial z}\right|_{z=0,y=0} dx \right) &\sim \mathcal{O}(1) \\ \implies \int_x \left(\left.\frac{\partial \omega_y}{\partial z}\right|_{z=0,y=0} dx \right) &\sim \frac{1}{\nu} \\ \implies \left.\frac{\partial \omega_y}{\partial z}\right|_{z=0,y=0} &\sim \frac{1}{\nu} \end{aligned} \tag{6.10}$$

Therefore at high Re for increasing Reynolds numbers, the vortex core flattening and filament stretching process intensifies such that $\nu\partial\omega_y/\partial z$ remains roughly constant.

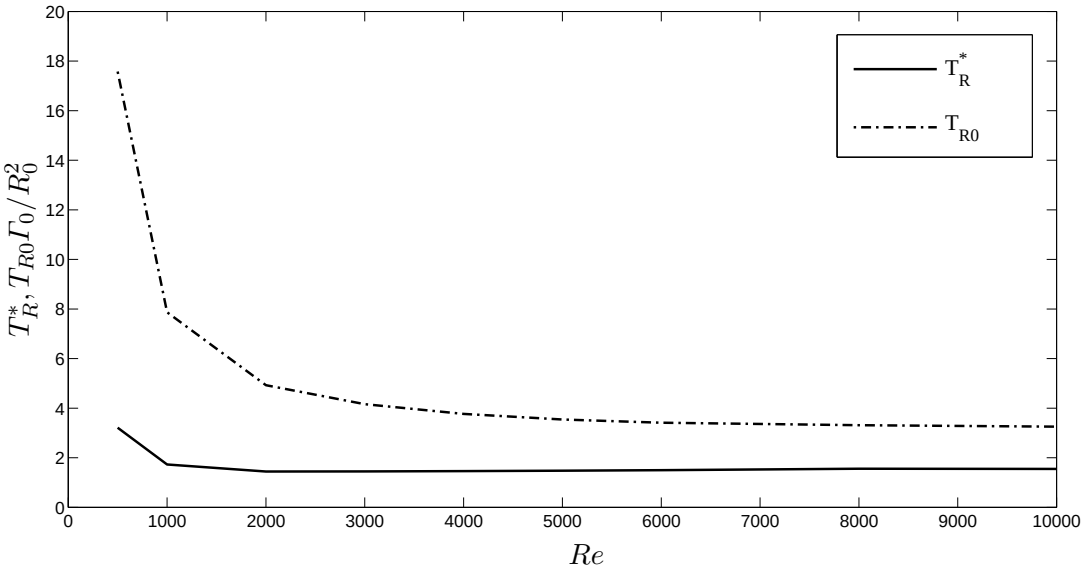

Figure 6.12: Variation with Re of ——— Normalised reconnection time T_R^* which accounts for the variable circulation and core radius at the beginning of reconnection using scaling rule (6.8) and - - - - Reconnection time T_{R0} given by (6.7) normalised by initial parameters of the vortex ring.

The contours of vorticity on the symmetry plane at the time of maximum rate of circulation transfer Re =500, 1000, 2000 and 3000 in figure 6.13 shows the intensification of the vortex core flattening with increasing Reynolds number. The histories of the maximum vorticity on the symmetry plane at different Reynolds numbers in figure 6.14 shows the intensification of the vortex stretching with Reynolds number.

6.4.3 Comparison with reconnection of vortex tubes

The previous studies in the literature on the variation of the reconnection time with Reynolds number pertain to studies of the reconnection of two vortex tubes, a different problem but one that is nevertheless very similar. Hussain and Duraisamy (2011) performed numerical simulations of two antiparallel vortex tubes with sinusoidal perturbations which grow in time leading to collision and reconnection (see figure 2.11 for a typical case at $Re = 2000$). As in the present work, they also considered a set of fixed initial parameters and varied the Reynolds number alone from 250 to 9000. The scaling of the reconnection time with Reynolds number is compared with their results.

Hussain and Duraisamy (2011) used an initial configuration in which the separation between the interacting vortex cores is of the order of the core size. Therefore the time before the initiation of the circulation transfer does not vary much for the cases at the different Reynolds numbers in their study. Therefore their results need not be corrected for changes in core size due to Re as in the present case. Figure 6.15 shows the variation of the peak value of the circulation transfer rate (which is proportional to the inverse of

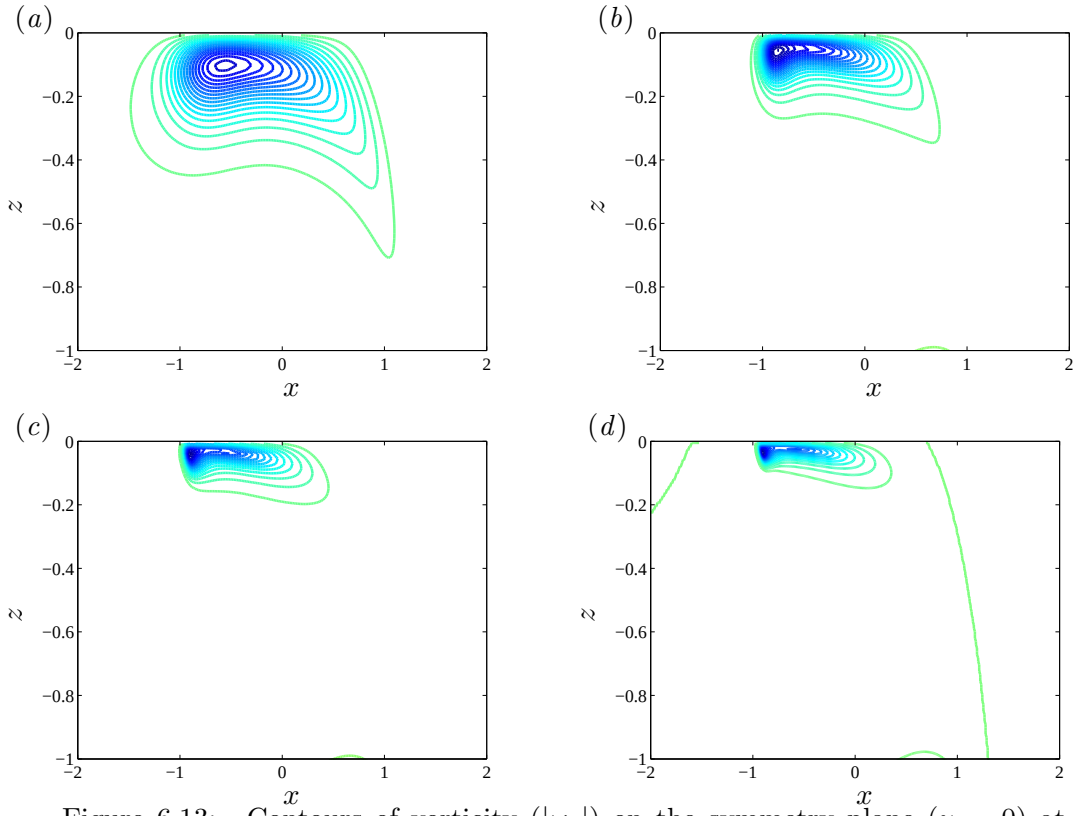

Figure 6.13: Contours of vorticity ($|\omega_y|$) on the symmetry plane ($y = 0$) at the time of maximum circulation transfer rate for the vortex rings from set I with $Re =$ (a) 500 (b) 1000 (c) 2000 and (d) 3000. A lowest contour level of $|\omega_y|_{\max}/40$ and an equal spacing of $|\omega_y|_{\max}/20$ was used.

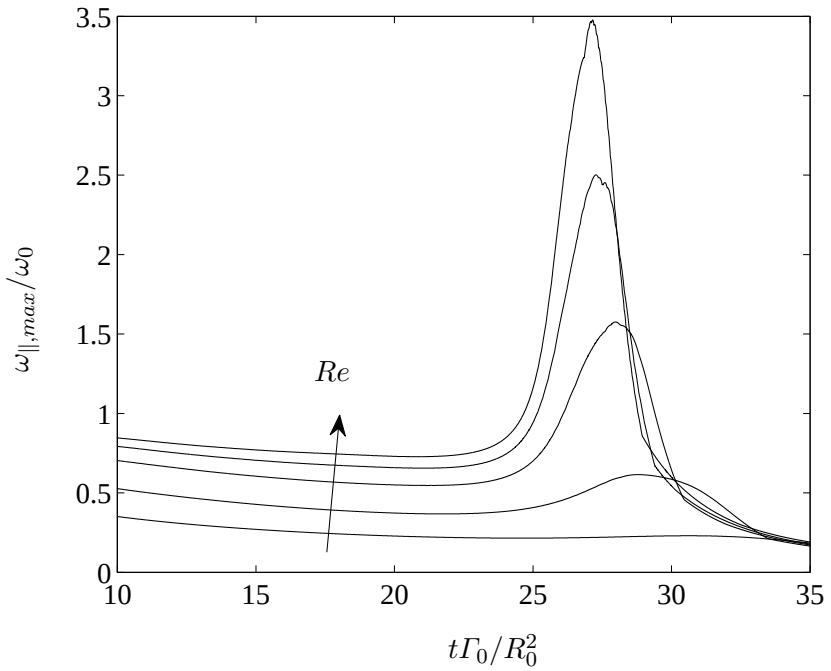

Figure 6.14: Evolution of the maximum vorticity on the symmetry plane normalised by the maximum value at $t = 0$ with non-dimensional time for the vortex rings in set I at $Re = 500, 1000, 2000, 3000, 4000$.

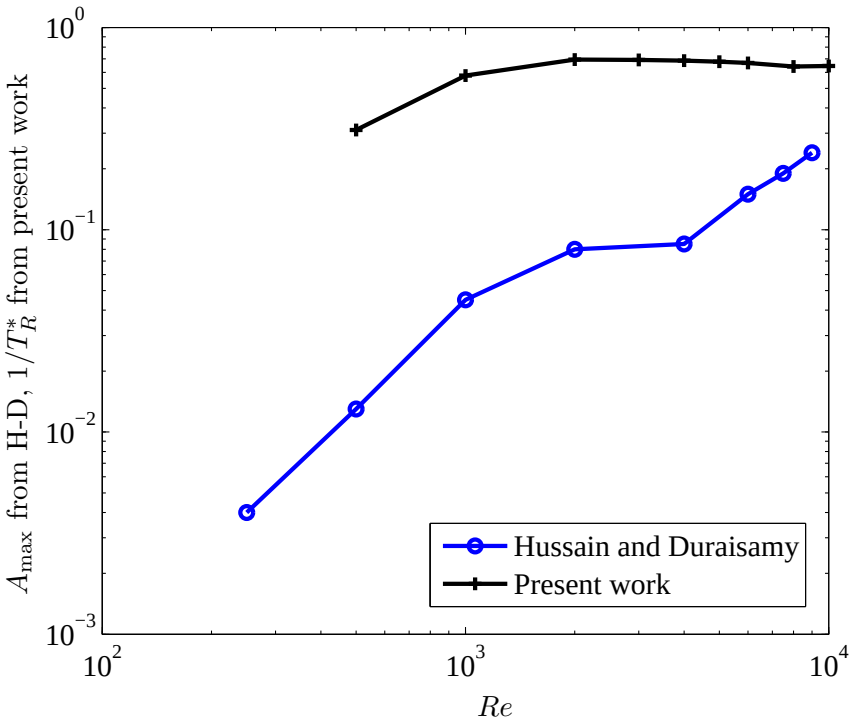

Figure 6.15: Variation of maximum circulation transfer rate from Hussain and Duraisamy (2011) (H-D) and $1/T_R^*$ from present work with Reynolds number.

T_R^*) with Reynolds number from their study (data obtained from figure 4a from Hussain and Duraisamy (2011)) and compares it with the variation of $1/T_R^*$ from the present work. In this figure there is an arbitrary scaling constant before the two sets of results.

Although figure 6.15 shows distinct regions at different Re, Hussain and Duraisamy (2011) fitted a single curve over the entire range of Reynolds numbers and reported a Re^n power variation with $n = 1.0$. However different trends can be observed within their data. In both cases, peak circulation transfer rates increase with Re at low Reynolds numbers. At moderate Reynolds numbers the peak circulation rates remain nearly constant. The values for the peak transfer rates is noted to be nearly constant in the range $2000 \lesssim Re \lesssim 4000$ in the data from Hussain and Duraisamy (2011). At high Reynolds numbers, the peak transfer rates continue to remain nearly constant in the present work. However, in the case of the reconnecting vortex pair, they begin to rise sharply with Re.

In section 6.5, the effects of high Reynolds number on vortex ring reconnection with a free-slip surface is investigated and the results are compared with Hussain and Duraisamy (2011).

6.5 High Reynolds number effects

In this section the simulation from set I with $Re = 8000$ is considered in order to study the effect of high Reynolds number on vortex ring reconnection.

The contours of ω_y (vorticity along surface-parallel direction) on the symmetry plane $y = 0$ (figure 6.16) show the evolution of the interacting vortex core during reconnection. Figure 6.17 shows the evolution of the maximum vorticity on the symmetry plane. The vortex core is flattened against the surface and transforms into a head-tail structure as described in section 6.3 (figure 6.16(b)). The flattened vortex core, then splits into two with the head detaching from the tail (figure 6.16(d)).

In section 6.4, the effect of increasing Reynolds number was found to be an intensification of the vortex stretching and flattening process such that the quantity $\nu\partial\omega_y/\partial z|_{z=0,y=0}$ remains roughly constant. In the present $Re = 8000$ simulation, due to the high Reynolds number the vortex core is flattened significantly and the maximum vorticity on the symmetry plane increases to $\simeq 7\omega_0$ at the peak of the vortex core flattening. As a result, the vortex core behaves like a strong vortex sheet and the splitting can be understood as occurring due to the tendency of a vortex sheet to roll-up at its edge. Subsequent to the detachment of the head, the vortex sheet-like core rolls up again at its head edge (figure 6.16(e),(f)). The rolling up process can occur only on one of the edges due to the presence of the surface.

Figure 6.18 from Hussain and Duraisamy (2011) shows the evolution of the interacting vortex cores during the reconnection of two antiparallel vortex tubes at a high Reynolds number, $Re = 6000$. The vortex cores are initially flattened and stretched into head-tail shaped structures and subsequently, the head detaches from the tail. The vortex sheet-like structure rolls up on its end again and splits up. Hussain and Duraisamy (2011) described the phenomenon as a Kelvin-Helmholtz instability. Unlike in the present case however, their flow develops antisymmetric features.

Therefore both in the case of the reconnection of a vortex ring with a free-slip surface and the reconnection of two colliding vortex tubes at high Reynolds numbers, due to the intense flattening and stretching the vortex core behaves like a vortex sheet and rolls up at its head edge and detaches to form vortex tubes (pairs of vortex tubes in the case of the reconnecting vortex pair). In the latter case, this instability occurs along with antisymmetric features.

The antisymmetric mode of the instability cannot occur in the present case of vortex ring reconnection due to the constraint imposed by the free-slip surface. To test whether the antisymmetric mode occurs in the absence of the surface, simulations of the collision of the vortex ring from set I with its image was performed without the presence of a free-slip surface. The initial setup used for this simulation of colliding vortex rings is a linear combination of the setup from figure 6.1 and its image about the $z = 0$ plane.

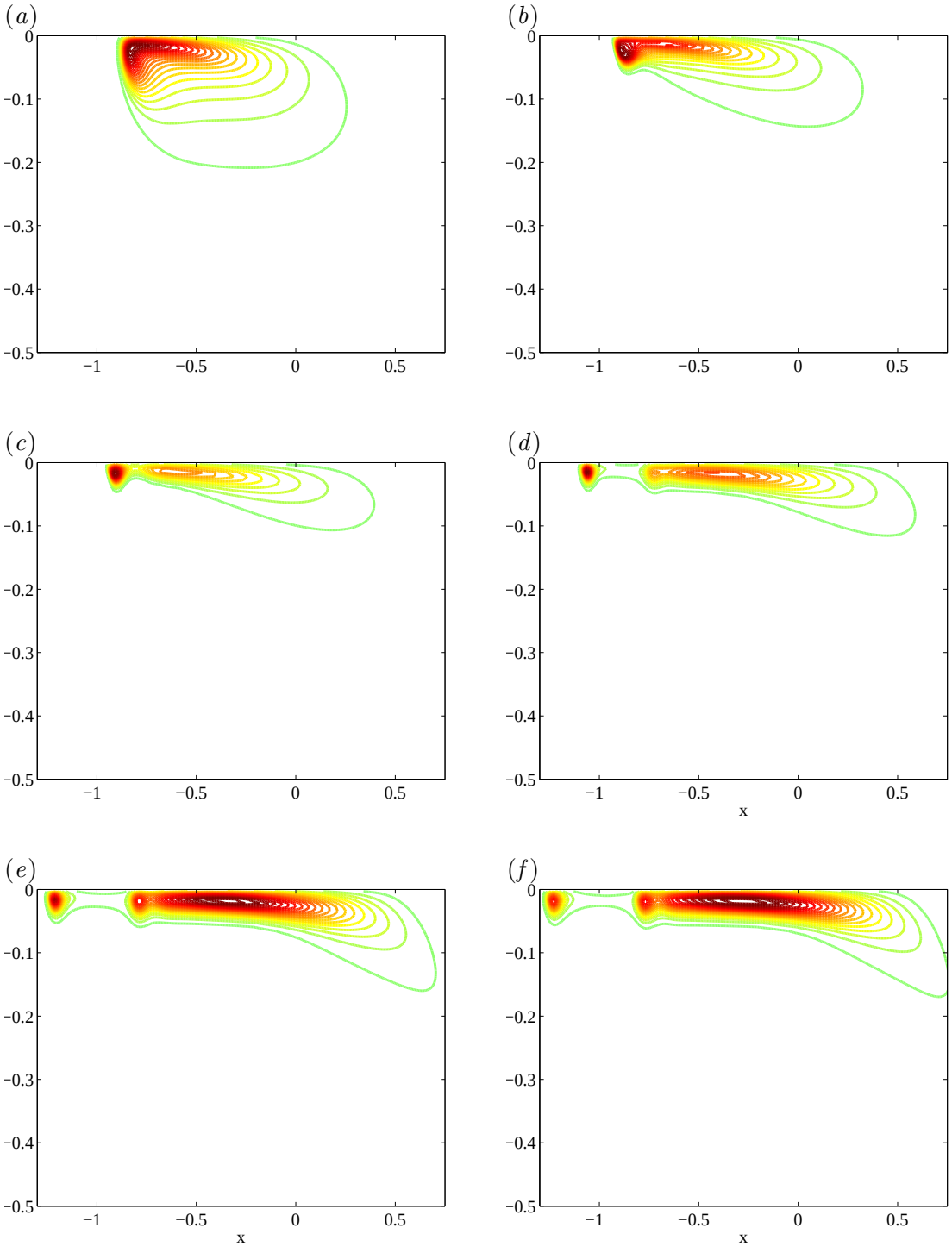

Figure 6.16: Contours of vorticity ($|\omega_y|$) on the symmetry plane $y = 0$ for $Re = 8000$ from set I at $t =$ (a) 25.5 (b) 26.0 (c) 26.5 (d) 27.5 (e) 28.5 and (f) 29.0 R_0^2/Γ_0. A lowest contour level of $|\omega_y|_{\max}/40$ and an equal spacing of $|\omega_y|_{\max}/20$ was used.

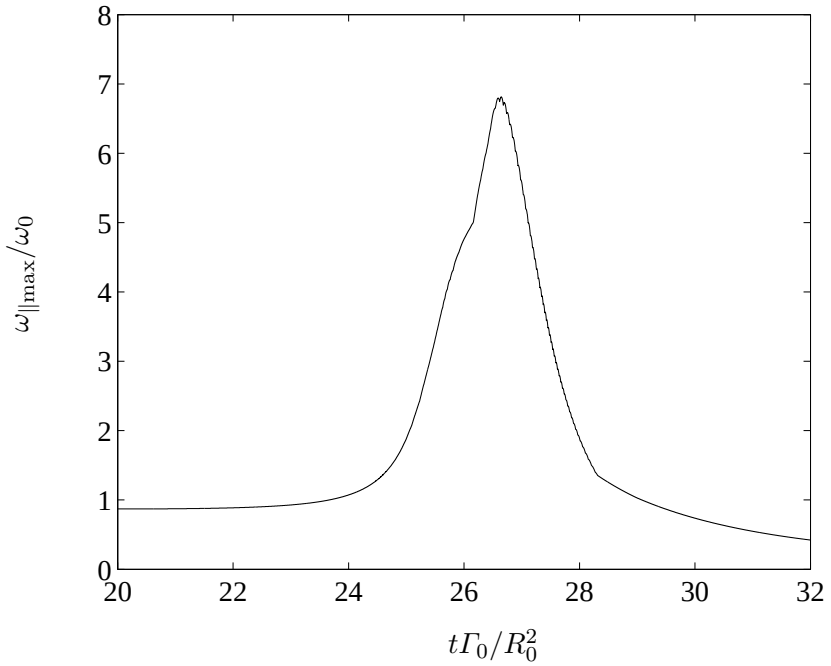

Figure 6.17: Evolution of the maximum vorticity on the symmetry plane ($\omega_{\parallel \max}$) normalised by the maximum value at $t = 0$ (ω_0) with non-dimensional time for $Re = 8000$ from set I.

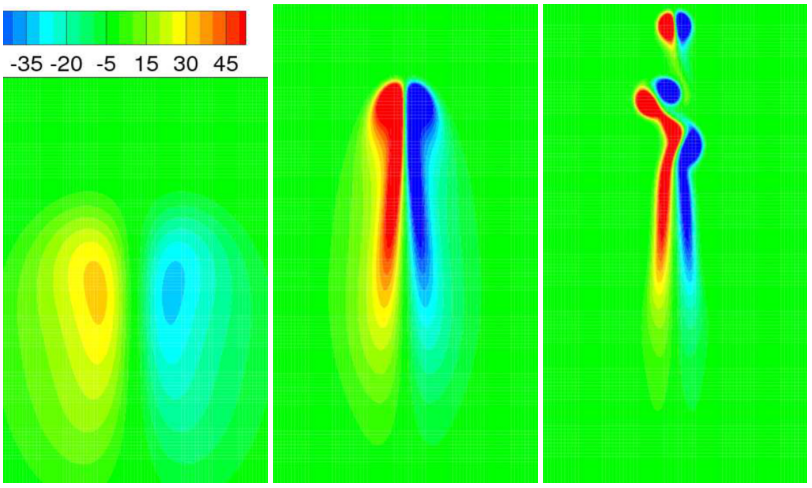

Figure 6.18: Evolution (from left to right) of contours of vorticity on the symmetry plane during the reconnection of two colliding vortex tubes at $Re = 6000$ from Hussain and Duraisamy (2011).

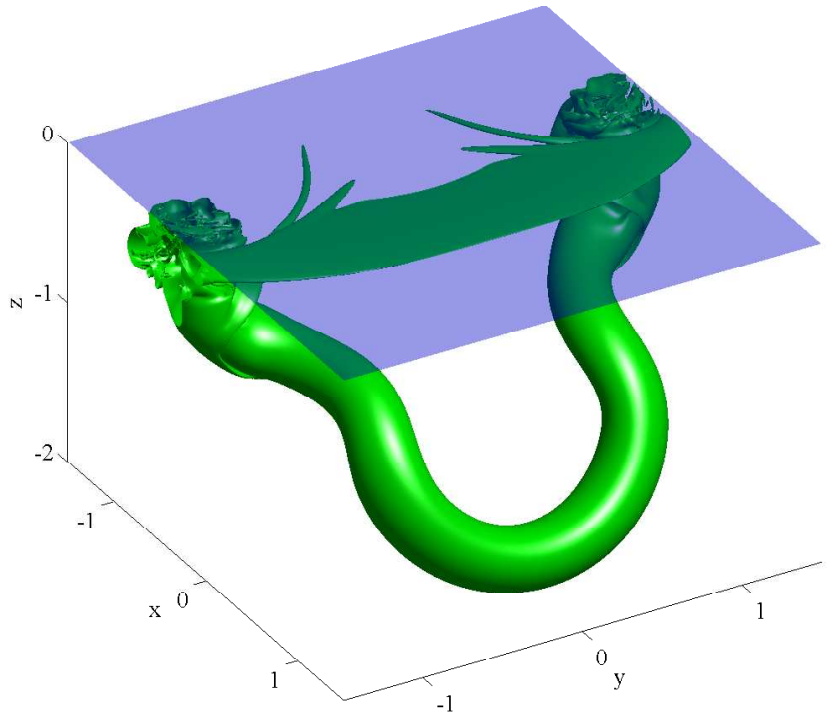

Figure 6.19: Isosurface of vorticity magnitude ($|\omega| = 0.04|\omega|_{\max}$) showing a late stage of the reconnection for the case from set I with $Re = 8000$ at $t = 32R_0^2/\Gamma_0$.

The analogous vortex ring collision problems to the cases from set I at $Re = 6000$ and $Re = 8000$ were performed. The results of the simulations were found to be identical to the results of the simulations of free-slip surface interactions at both Reynolds numbers. The antisymmetric mode of the instability did not occur even at $Re = 8000$. This may be due to the stabilising influence of the lower part of the vortex ring which advects the interacting vortex sheet away from the surface.

6.5.1 Late stages of reconnection at high Re

Figure 6.19 shows an isosurface of vorticity at the late stage of the reconnection at $Re = 8000$, showing the detached head-tail structure of the surface sheet. The detached head is visible in the form of a rolled-up vortex and the tail as a thin vortex sheet. Both become wrapped around the two bridges of reconnected surface-normal vorticity. As the bridges rotate under their self-induced velocity, the vortex sheet gets further stretched and wrapped around the bridges.

As the thin vortex sheet and the rolled up vortex tubes get wrapped around the bridges, they are able to contact the surface away from the symmetry plane and undergo additional disconnection and reconnection events. The main type of reconnection discussed in this chapter and in the literature involves disconnection of vortex filaments at the symmetry plane and simultaneous reconnection to the surface on either side of the symmetry plane (figure 6.6a). Figure 6.20(a) shows a schematic of vortex filaments

undergoing these additional reconnections occurring at high Reynolds numbers. The resulting reconnected vortex filaments with opposing signs of surface-normal vorticity lie on the same side of the symmetry plane and interact with each other adding to the flow complexity at high Reynolds numbers. The circulation associated with this additional reconnection is denoted by $\Gamma_{\perp 2}$) and plotted in figure 6.20(b) for the high Reynolds number case Re =8000. The maximum value attained by $\Gamma_{\perp 2}$) during the reconnection is less than 0.01 Γ_0 at $Re = 2000$. The maximum value increases with increasing Reynolds number and reaches up to $\simeq 0.2\Gamma_0$ at Re =8000 (figure 6.20(b)).

6.6 Breakdown of bridges after reconnection at high Reynolds numbers

In this section, the evolution of the flow after the first reconnection of a vortex ring with a free-slip surface at a high Reynolds number is studied. The results of the simulation from set III with initial slenderness ratio $\delta_0/R_0 = 0.3$, initial depth $h/R_0 = 3.0$ and initial inclination of $\gamma = 7^\circ$ at $Re = 7500$ is presented.

Figure 6.21 shows the variation of the total enstrophy, Ω, with time for this case. The first local peak at $t \simeq 60R_0^2/\Gamma_0$ corresponds to the vortex stretching during the first reconnection. As in the case of the simulations from set I at high Reynolds numbers, the thin vortex sheet and the rolled up vortex tube are both wrapped around the two bridges of reconnected vorticity (figure 6.22(a)). The vortex sheet and the vortex tube are progressively wrapped around the bridges. This destabilises the flow around the site of the bridges and leads to a rapid generation of small-scale vortical structures (figure 6.22(b)). At the end of the first reconnection there is a rapid rise in the total enstrophy associated with this small-scale structure generation mechanism.

Simultaneous with the first reconnection, the lower part of the vortex ring continues to advect towards the surface under its self-induced velocity and begins a second reconnection with the surface. The interacting vortex core again gets deformed into a head-tail structure (oriented in the opposite direction to the first reconnection). The disconnection of vortex filaments, reconnection with the surface and accumulation of reconnected vortex filaments in the form of two bridges occurs similar to the first reconnection.

The vortex core flattened into a thin sheet rolls up at its edge forming a vortex which splits away. This process repeats twice leading to three distinct vortex tubes wrapped around the reconnected bridges at their ends. The distinct co-rotating vortices roll-up together and merge into a single vortex. The remnant vorticity in the tail also rolls up into a separate vortex tube (Figures 6.23 (a),(b),(c),(d)).

The repeated roll-up and detachment of the newly formed heads of the vortex sheet generating multiple vortex strands during the second reconnection is visualised using an

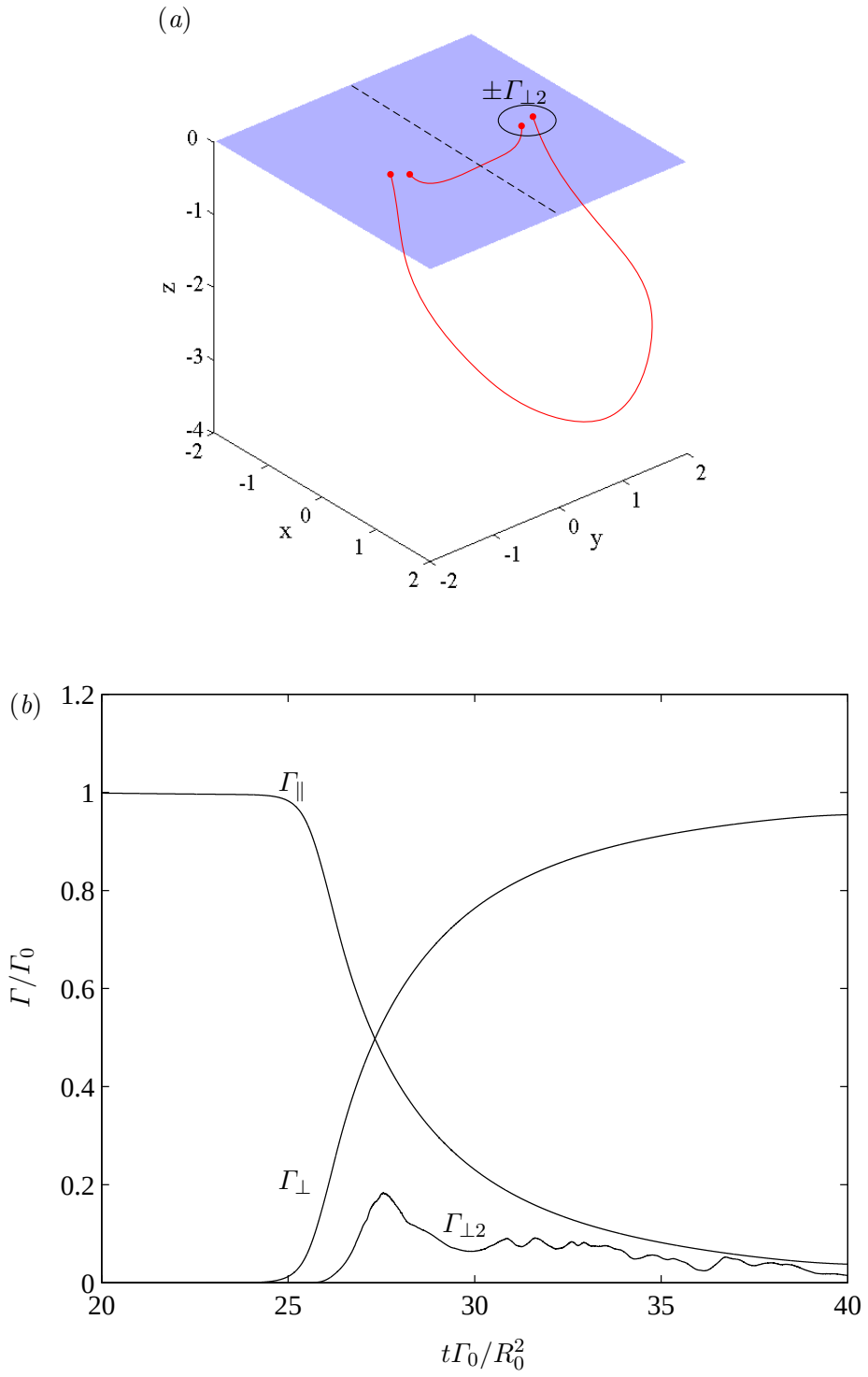

Figure 6.20: (a) Schematic of the additional reconnection at high Reynolds number (b) Evolution of the surface-parallel, surface-normal circulations and the circulation associated with the additional reconnection (normalized by Γ_0) with time for the case from set I at $Re = 8000$.

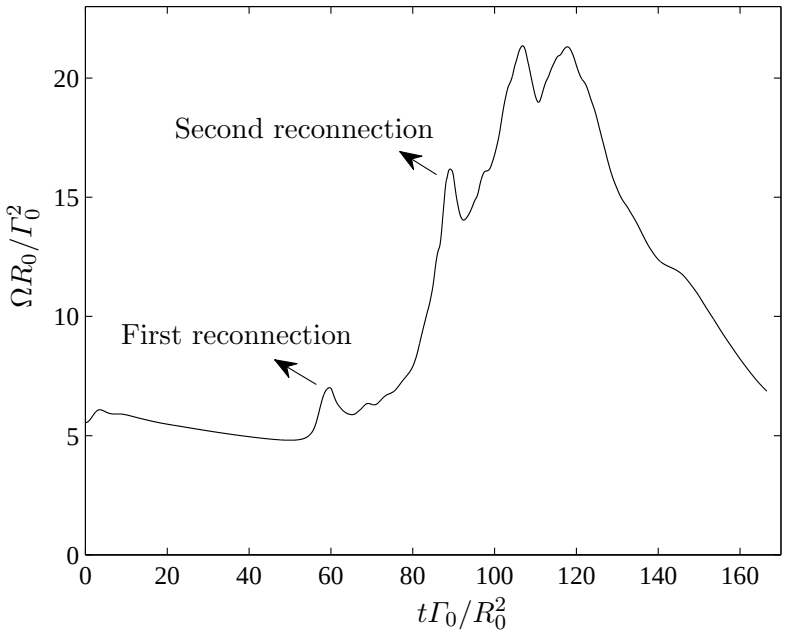

Figure 6.21: Evolution of total enstrophy Ω with time for the case from set III.

isosurface of the second invariant of the velocity gradient tensor $Q = -(1/2)(\partial u_i/\partial x_j)(\partial u_j/\partial x_i)$ in figure 6.24. Since Q represents the balance between the rotation and shear strain rates, an isosurface of Q is a useful marker of vortical structure (J. Jeong and Hussain, 1995).

At the end of the second reconnection, the flow is dominated by several thin vortex tubes. These are progressively stretched and wrapped around the two pairs of bridges formed as a result of the two reconnections. This process leads to a rapid generation of smaller scale vortical structures from the entire doubly-connected vortex ring structure extending into its wake. Figure 6.25 uses isosurfaces of the second invariant of the velocity gradient tensor to highlight the vortical structure of the flow at the late stages of the second reconnection.

Figure 6.26 shows the circulations of the interacting vortex core (along the surface-parallel direction) and the reconnected vortex filaments (along the surface-normal direction) during the second reconnection. The circulation transfer proceeds until $\Gamma_{\parallel} \simeq 0.4\Gamma_0$ before it is interrupted by the roll-up of the vortex sheet.

A local peak in the total enstrophy, occurs at $t \simeq 90R_0^2/\Gamma_0$ due to the second reconnection. The enstrophy continues to rise after the second reconnection as well reaching a maximum at $t \sim 110R_0^2/\Gamma_0$. Therefore the small-scale structure generation mechanism is sufficiently strong to produce an approximately four-fold increase in the overall enstrophy of the flow compared to the state at the end of the first reconnection.

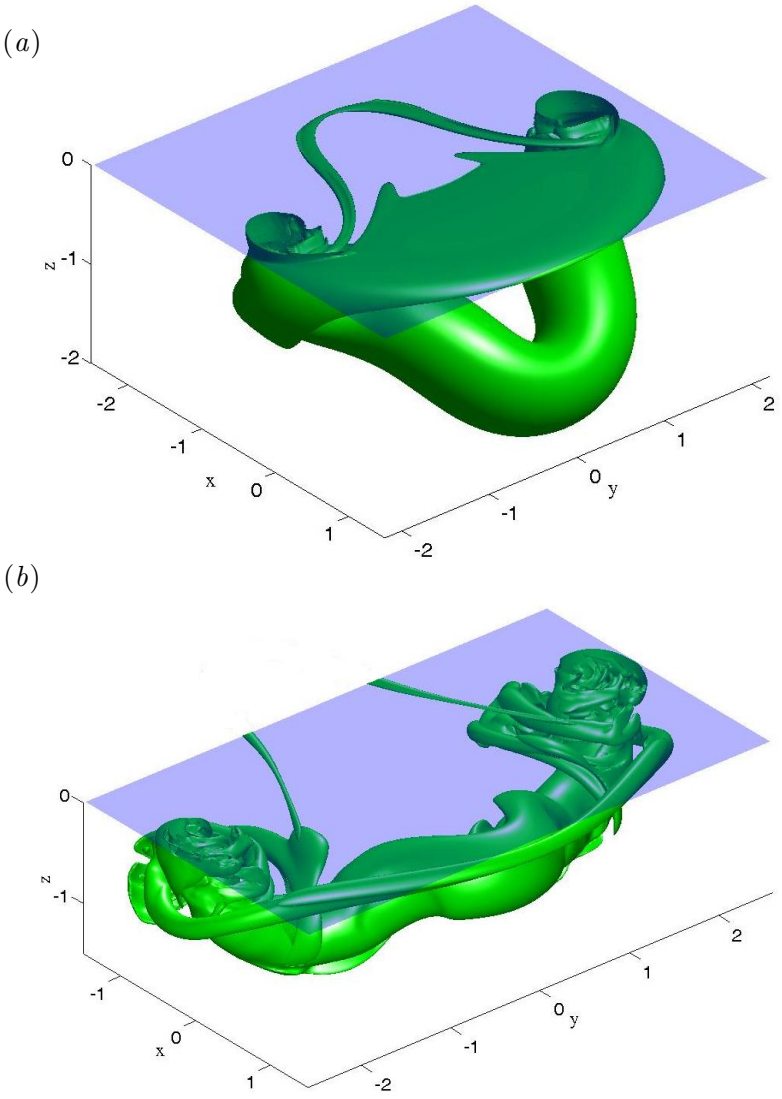

Figure 6.22: Isosurfaces of vorticity magnitude ($|\omega| = 0.1|\omega|_{\max}$) showing late stages of the first reconnection for the case in set III at $t =$ (a) 68 and (b) 76 R_0^2/Γ_0.

6.6.1 Small-scale structure generation mechanism

Thus the following is the description of the mechanism of small-scale structure generation: The vortex core interacting with the surface is flattened into a vortex sheet whose thickness decreases and strength increases with increasing Re. The vortex sheet is wrapped around the bridges of reconnected vortex filaments on either side, and is continuously stretched and wound by them. The head edge of the vortex sheet rolls up and detaches itself from the sheet, creating a new edge which can then undergo the same process again ultimately producing multiple strands of vorticity. Both the vortex sheet and the rolled up vortex tubes are progressively wound around the bridges of reconnected vorticity. This leads eventually to a rapid production of small-scale structures around

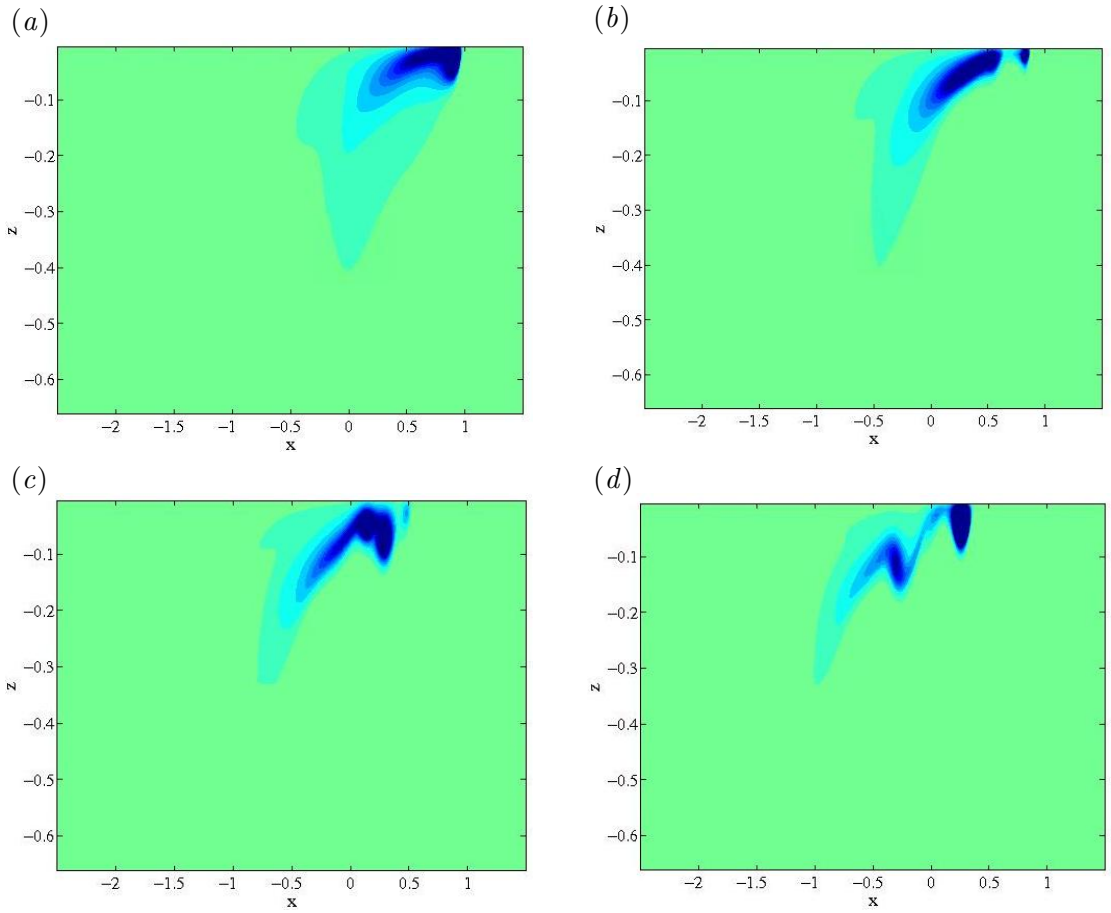

Figure 6.23: Contours of vorticity (ω_y) on the symmetry plane $y = 0$ at $t = (a)$ 82 (b) 84 (c) 86 and (d) 88 R_0^2/Γ_0 for the case in set III.

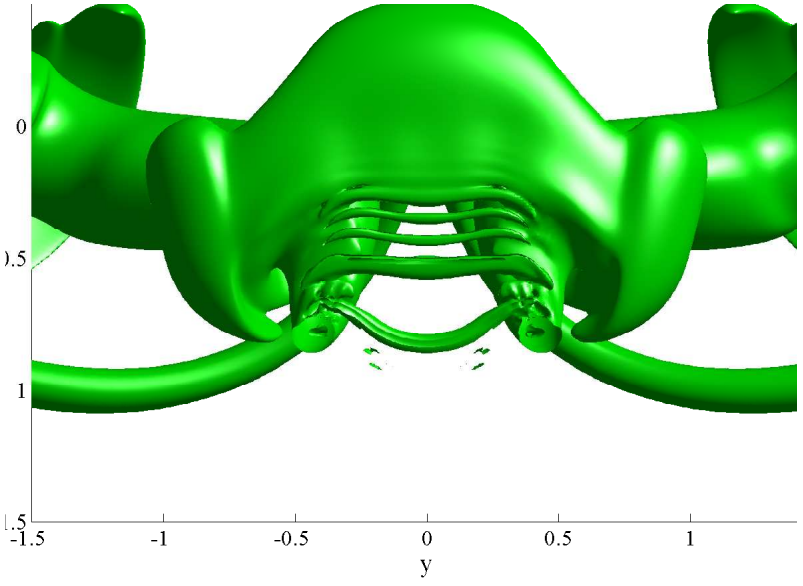

Figure 6.24: Close-up view from above the free-slip surface of isosurface of Q ($QR_0^4/\Gamma_0^2 = -0.025$) showing the multiple roll-ups of the newly formed heads of the vortex sheet during the second reconnection for the case in set III at $t = 84R_0^2/\Gamma_0$. The entire vortex ring structure is seen in figure 6.25(a).

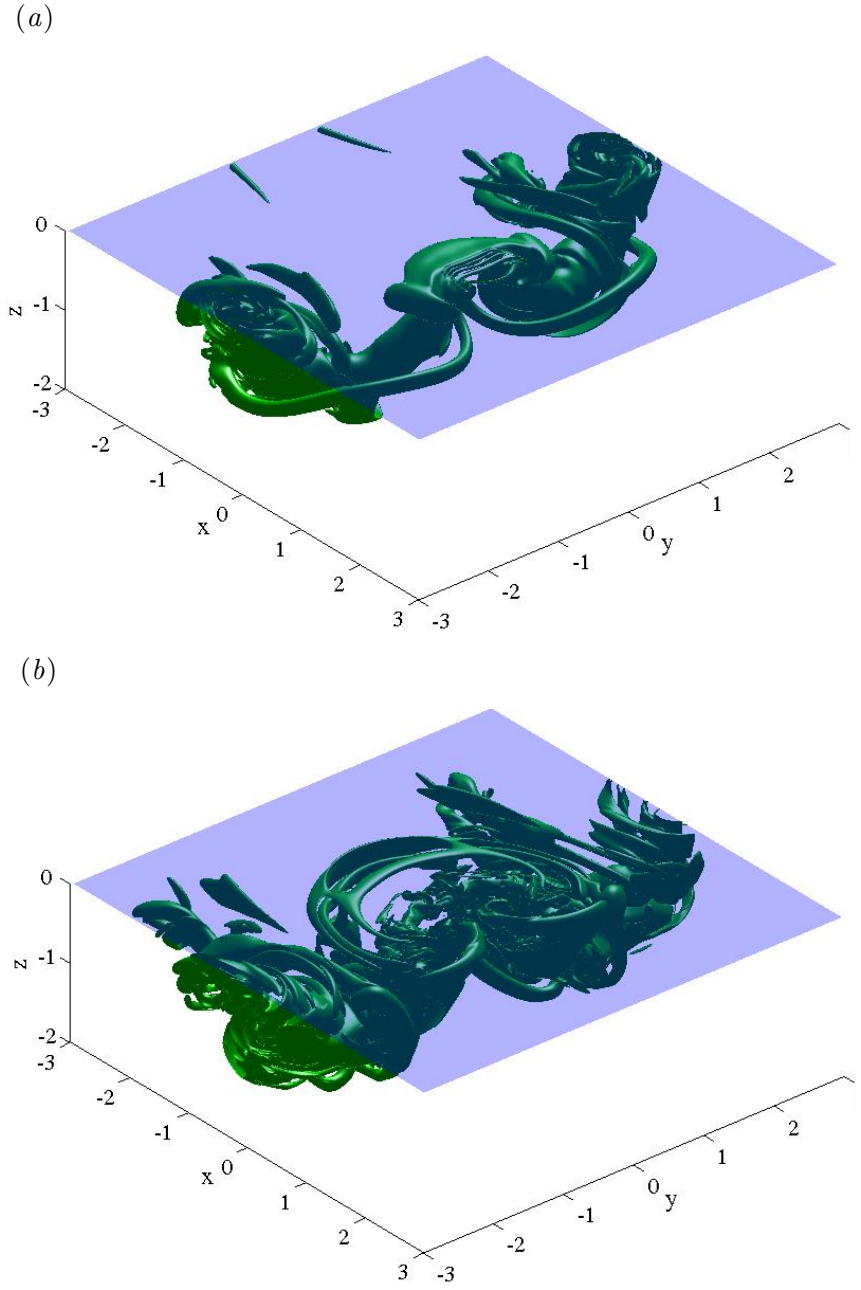

Figure 6.25: (a)–(b) See following page for caption.

the bridges. These strands of vorticity also roll-up together and become intertwined. The flowfield is dominated by a profusion of tangled vortex tubes which develops into a more substantial breakdown of the remaining ring structure.

6.6.2 Energy spectrum

The flow after the breakdown of the vortex ring closely resembles a typical turbulent flow showing irregularity, intermittency and high rates of dissipation and enstrophy.

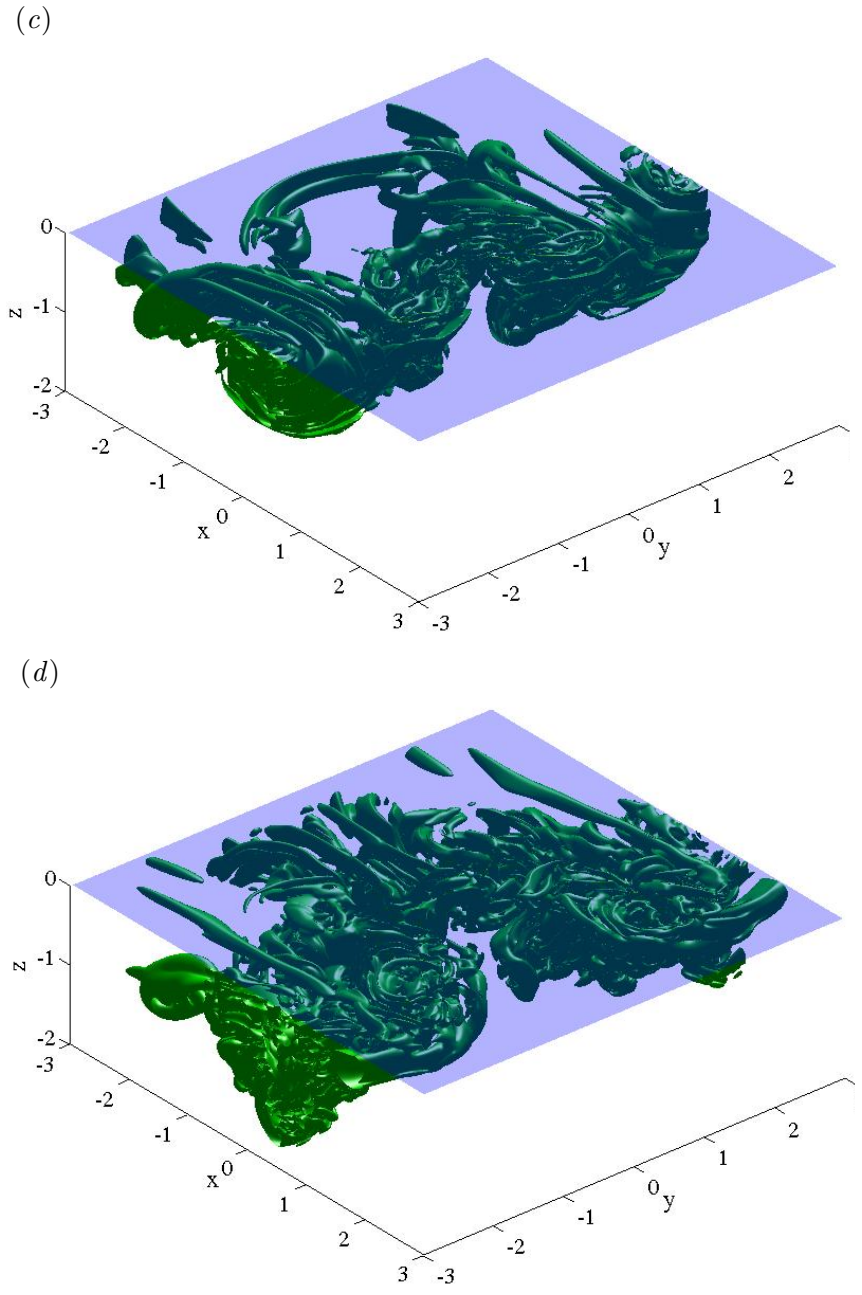

Figure 6.25: Isosurfaces of Q ($QR_0^4/\Gamma_0^2 = -0.025$) highlighting the vortical structure at $t =$ (a) 84 (b) 96 (c) 104 and (d) 140 R_0^2/Γ_0.

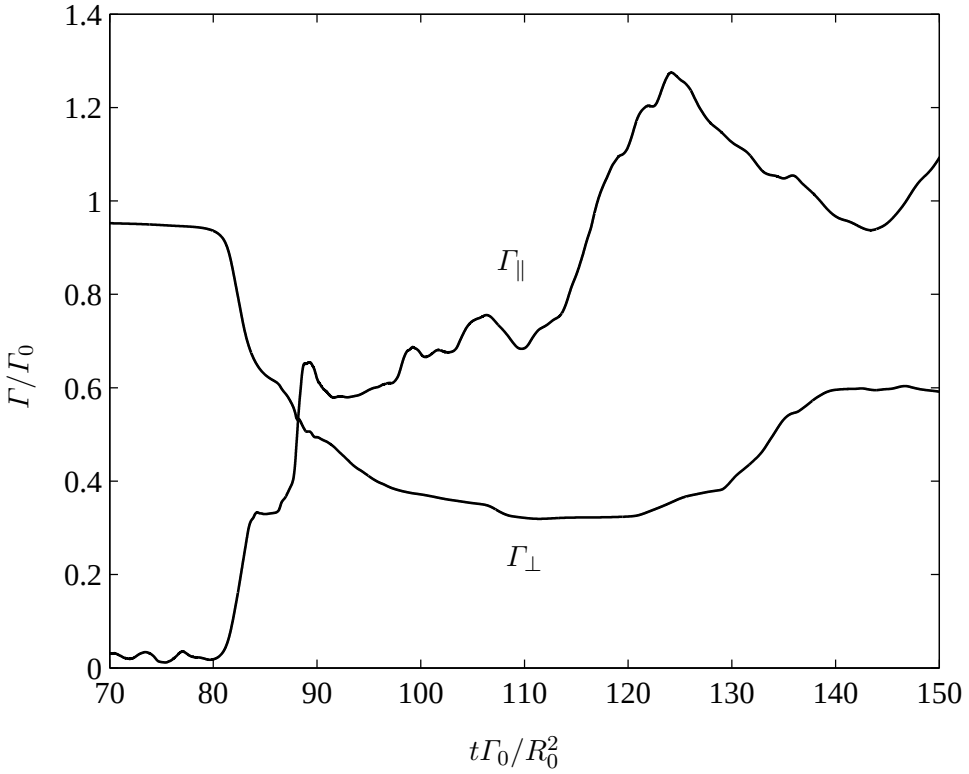

Figure 6.26: Evolution of the surface-parallel and surface-normal circulations associated with the (normalized by Γ_0) with non-dimensional time.

(a) (b)

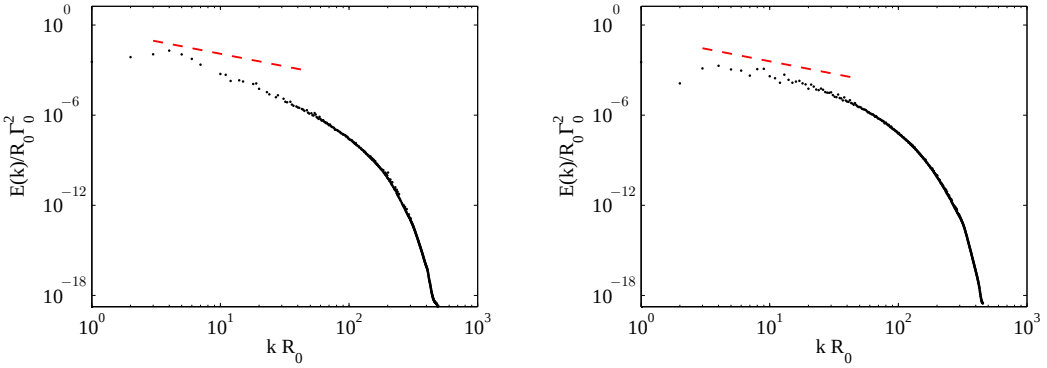

Figure 6.27: Log-log plot of wavenumber and energy present at that wavenumber at $t =$ (a) 80 and (b) 140 R_0^2/Γ_0 for the case from set III with $\gamma = 7°$. Dashed line corresponds to $k^{-5/3}$ behaviour.

The energy spectrum for this complex flow was computed and compared with the $-5/3$ power law.

The energy spectrum in a windowed three-dimensional region enclosing the reconnected vortex ring is plotted at t =80 R_0^2/Γ_0 (figure 6.27a) and t =140 R_0^2/Γ_0 (figure 6.27b). As expected the energy distribution shifts with time towards the higher wavenumbers (k) and begins to approximate the $-5/3$ inertial range behaviour at the lower wavenumbers. At high k it falls off under the influence of viscous dissipation.

6.7 Conclusions

Numerical simulations of the interaction of a vortex ring with a free-slip surface were performed capturing the characteristic features of vortex reconnection described in the literature. The effect of viscosity on the circulation transfer rate was investigated. The reconnection time was normalised by an appropriate inviscid timescale to account for the variable parameters of the vortex ring at the beginning of the circulation transfer. The normalised reconnection time decreases with increasing Reynolds number at low Reynolds numbers before reaching a minimum value at $Re \simeq 2000$. For greater values of Reynolds number the reconnection time almost remains constant, only increasing very slowly with Reynolds number. The near-saturation of reconnection time implies that the vorticity gradient at the surface varies as $\mathcal{O}(1/\nu)$. This is achieved by an intensification of the vortex core flattening and filament stretching process with increasing Reynolds number.

The scaling of the peak circulation transfer rates with Reynolds number was compared to the scaling in the case of the reconnection of a pair of anti-parallel vortex tubes investigated by Hussain and Duraisamy (2011). In both cases the peak rates increased with Re at low Reynolds numbers and remained nearly constant at moderate Reynolds numbers. The scaling behaviour is different at high Reynolds numbers with the peak rates rising sharply with Re for the reconnecting vortex tubes but not for the colliding vortex rings.

At high Reynolds numbers the vortex core interacting with the surface is flattened and stretched into a thin, intense vortex sheet. The head edge of the vortex sheet rolls up and detaches creating a new edge which can then undergo the same process, ultimately producing several strands of vorticity which become intertwined. An anti-symmetric mode of the same instability occurs in the case of the reconnecting vortex tubes. The anti-symmetric mode did not occur in the case of colliding vortex rings despite the absence of the constraint imposed by the surface.

At high Reynolds numbers the thin vortex sheet and the multiple vortex tubes (generated by the roll-up of the vortex sheet) are wrapped around the bridges of reconnected surface-normal vorticity. As the bridges rotate under their self-induced velocity the vortex sheet and the vortex tubes get further stretched and wrapped around the bridges. This leads to a rapid generation of small-scale vortical structure at the site of the bridges. The flow becomes increasingly complex and is dominated by a profusion of vortex tubes and small-scale structure.

Unlike the well-known Widnall instability (Widnall et al., 1974) associated with wavy displacement of the vortex core, the breakdown studied in this work occurs solely due to the mechanics of the reconnection process and provides a means of producing small-scale structure from the reconnected vortex ring. The mechanism involves two processes:

(i) The flattening of the reconnecting vortex ring core into a thin sheet which repeatedly splits up into strands of vorticity and (ii) The wrapping up of the vortex strands around the two bridges of reconnected surface-normal vorticity destabilising them and generating fine-scale complex structure.

Chapter 7

Vortex rings with swirl in unbounded flow

In this chapter DNS of vortex rings with swirl in unbounded flow is presented. The numerical approach and initial setup (figure 7.1) used here is the same as used in section 4.1 to study classical vortex rings in unbounded flow.

The details of the simulation including the initialisation of the vortex rings with swirl are presented in section 7.1. The method used to track the amount of swirl in the vortex ring is introduced in section 7.2. The adequacy of the spatial resolution is demonstrated in section 7.3. The formation of an axial vortex and the structure of the vortex ring with the developed axial vortex are discussed in section 7.4. The existence of a maximum limit for the swirl in a vortex ring is shown in section 7.6. The final conclusions are summarised in section 7.7.

7.1 Simulation details

All the simulations discussed in this chapter were performed in a cubic domain with dimensions $8R_0 \times 8R_0 \times 8R_0$ with $512 \times 512 \times 512$ uniformly spaced grid points. The timestep was chosen such that the Courant-Freidrichs-Lewy (CFL) number remained below 0.20 throughout the simulation to ensure numerical stability.

7.1.1 Vortex ring initialisation

Two different types of vortex rings with swirl were used as the initial condition in this study. This provided a means of verifying the independence of the observed characteristics of the vortex rings in the simulations from the particular method of initialisation.

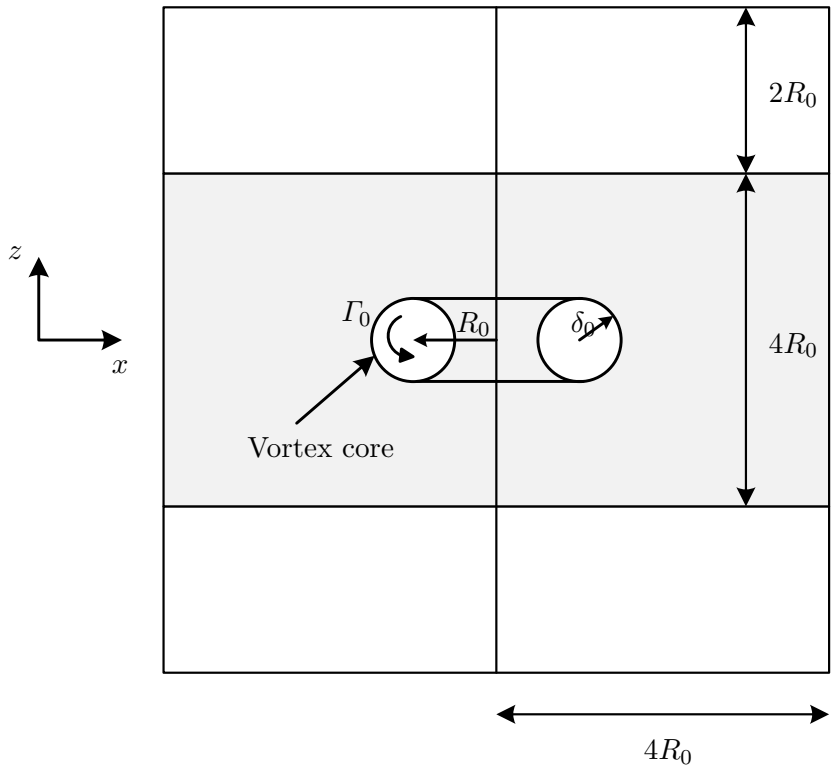

Figure 7.1: Schematic of the computational domain for the study of vortex rings with swirl in unbounded flow. The shaded region corresponds to the logging domain.

7.1.1.1 Gaussian profile

The core of the vortex ring was initialised with a Gaussian distribution of vorticity

$$\omega_\theta = \frac{\Gamma_0}{\pi\delta_0^2} \exp\left(-\frac{(r-R_0)^2+z^2}{\delta_0^2}\right) \tag{7.1}$$

where $r^2 = x^2 + y^2$ and δ_0 defines the core thickness. The velocity field corresponding to this vorticity distribution was computed using the vector stream function method outlined in section 4.1.2.

An azimuthal (swirl) velocity field directly proportional to the Gaussian vorticity distribution was added to obtain the complete initial velocity field used for the DNS, so that

$$u_\theta = \frac{S\Gamma_0}{R_0} \exp\left(-\frac{(r-R_0)^2+z^2}{\delta_0^2}\right) \tag{7.2}$$

where S is the swirl parameter. It should be noted that for this initialisation the maximum azimuthal velocity is $(S\Gamma_0/R_0)$ and the angular momentum in the vortex rings (measured as described in section 7.2) depends on both the swirl parameter and the core radius.

7.1.1.2 Steady-state Euler solution

Eydeland and Turkington (1988) developed a variational method to find exact steady solutions of the Euler equations for inviscid, incompressible, axisymmetric flow with a compact vorticity distribution confined to a toroidal region. These solutions form a two-parameter family. Lifschitz et al. (1996) provided a method of obtaining these steady-state solutions for a finite computational domain enclosing the vortex ring.

The solutions are expressed in terms of the Stokes stream-function, ψ for axisymmetric, inviscid flows:

$$u_r = -\frac{1}{r}\frac{\partial \psi}{\partial z},\ u_z = \frac{1}{r}\frac{\partial \psi}{\partial r}$$

where u_r, u_θ, u_z are the cylindrical velocity components.

The solution is given by

$$\begin{aligned} u_\theta &= \frac{1}{r} f(\psi) \\ \omega_\theta &= -r h'(\psi) + \frac{1}{r} f(\psi) f'(\psi) \end{aligned} \tag{7.3}$$

where ω_θ is the azimuthal vorticity component. The structure functions $f(\psi)$ and $h(\psi)$ are given by

$$\begin{aligned} f(\psi) &= \sqrt{\frac{2\alpha}{\zeta+1}}\psi_+^{(\zeta+1)/2} \\ h(\psi) &= h_0 - \frac{\beta}{2(\zeta+1)}\psi_+^{\zeta+1} \end{aligned} \tag{7.4}$$

where $\psi_+ = \max(\psi, 0)$. α, β, ζ and h_0 are positive constants. The value of h_0 is not important. A value of 1.5 was used for the exponent ζ as in Lifschitz et al. (1996). Thus we have a two-parameter family of vortex rings. For $\alpha = 0$ swirl-free vortex rings are obtained for which β determines the slenderness ratio. The core azimuthal vorticity profile for these swirl-free vortex rings given by $\omega_\theta/r = (\beta/2)\psi_+^\zeta$, was shown to be close

Vortex ring	Type	Parameters	Ring characteristics	
			δ_0/R_0	$\mathcal{A}/(\Gamma_0 R_0^3)$
EU1	Euler solution	$\alpha = 50, \beta = 0$	0.29	1.54
EU2	Euler solution	$\alpha = 60, \beta = 35$	0.23	1.05
EU3	Euler solution	$\alpha = 150, \beta = 60$	0.16	0.71
GS1	Gaussian	$S = 0.30$	0.30	0.56
GS2	Gaussian	$S = 0.40$	0.30	0.74
GS3	Gaussian	$S = 0.60$	0.30	1.11
GS4	Gaussian	$S = 1.00$	0.30	1.85

Table 7.1: Vortex rings used in study of vortex rings with swirl in unbounded flow.

to that of an equilibrium vortex ring without swirl in chapter 4. For $\beta = 0$ Beltrami vortex rings in which the vorticity vector is parallel to the velocity vector are obtained.

The method described by Lifschitz et al. (1996) was altered slightly to obtain vortex rings with radius $R = R_0$ and circulation $\Gamma = \Gamma_0$ (R and Γ as defined in equations 4.9 and 4.8 respectively). The numerical method is described in detail in Appendix A.

The vorticity field solution obtained using the Euler solver is used to compute the corresponding initial velocity field using the vector stream function method outlined in section 4.1.2. Table 7.1 lists the different Euler solution initialised and Gaussian initialised vortex rings used in this chapter along with the defining parameters and the ring characteristics.

Simulations of all the vortex rings were performed at $Re = 1500$. For the Gaussian initialised vortex rings an additional simulation was performed at $Re = 3000$.

7.2 Tracking the vortex ring swirl

The linear impulse is an integral quantity defined as

$$I = \frac{\rho}{2} \iiint_V \vec{r} \times \vec{\omega} dV \tag{7.5}$$

where $\vec{r}$ is the position vector and $\vec{\omega}$ is the vorticity vector. Linear impulse can be interpreted as the total impulsive force required to generate a flow from rest (Saffman, 1992).

To measure the swirl the integral quantity angular impulse defined as

$$\mathcal{A} = \frac{\rho}{3} \iiint_V \vec{r} \times (\vec{r} \times \vec{\omega}) dV \,, \tag{7.6}$$

was used. Angular impulse can be interpreted as the total moment of the impulsive force system that generated the flow from rest (Saffman, 1992) and is zero for swirl-free vortex rings. For an axisymmetric vortex ring, the angular impulse is directed purely along the axial direction.

The angular impulse is invariant in unbounded flow in the absence of any moment due to external non-conservative forces. As the vortex ring translates along its axis it sheds fluid with angular momentum into the wake. In order to track the swirl present in the vortex ring alone, the angular impulse was computed by performing the integration within a logging domain attached to the vortex ring defined by $-2R_0 < z < 2R_0$ (shaded region in figure 7.1).

7.3 Adequacy of spatial resolution

The adequacy of the spatial resolution is demonstrated for the highest swirl case at $Re = 3000$. The energy balance between the volume integrated kinetic energy per unit mass with respect to the co-moving reference frame K, the volume integrated rate of kinetic energy dissipation ϵ_K and the total volume integrated kinetic energy flux out of the domain F_K (see section 4.3.1 for details) given by

$$-\frac{\mathrm{d}K}{\mathrm{d}t} = \epsilon_K + F_K \,,$$

was tracked with time. Figure 7.2 compares the histories of the quantities represented by left and right hand sides of this equation for this case. A period of rapid enstrophy growth occurs immediately after initialisation for this flow (see section 7.6 for details of the flow). The difference between the two sides of (7.7) remains less than 4% at the enstrophy peak demonstrating that the spatial discretisation is sufficient to accurately compute the flow.

For all the other simulations performed in this chapter, the error remains less than 1% throughout.

7.4 Formation of an axial vortex

In this section the early period of evolution of the vortex rings with swirl after initialisation is studied. Both Gaussian initialised and Euler solution initialised vortex rings are shown to develop an axial vortex during this period. The mechanism for the formation of the axial vortex is explained.

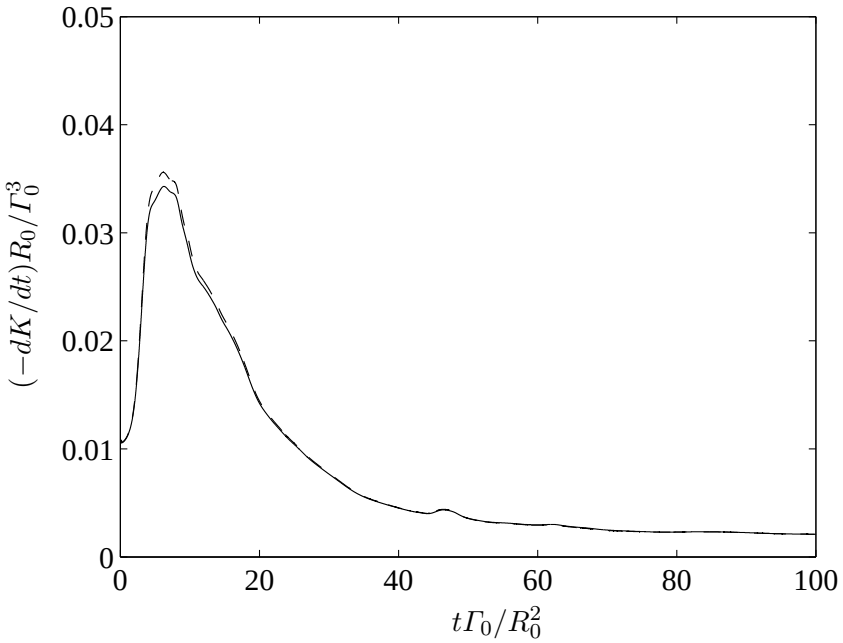

Figure 7.2: Comparison of histories of - - - - Rate of decrease of volume-integrated kinetic energy $(-\mathrm{d}K/\mathrm{d}t)$ and ——— Sum of volume-integrated rate of dissipation and energy flux $(\epsilon_K + F_K)$ for the simulation of vortex ring EU4 at $Re = 3000$.

7.4.1 Vortex ring initialised with Gaussian profile

The simulation of the Gaussian initialised vortex ring GS1 at $Re = 1500$ is considered in this section. Figure 7.3 shows the contours of azimuthal vorticity (ω_θ) and azimuthal velocity (u_θ) on the radial plane $\theta = 0$ at different times after the vortex ring initialisation. Fluid with azimuthal velocity is initially located within the core of the vortex ring. After initialisation the distribution of azimuthal velocity begins to relocate towards the axis of the vortex ring. However the azimuthal velocity is zero on the vortex ring axis. The axial vorticity (ω_z) in axisymmetric flow is given by

$$\omega_z = \frac{\partial u_\theta}{\partial r} + \frac{u_\theta}{r}$$

The centreline vorticity is

$$\omega_z|_{r=0} = 2 \lim_{r \to 0} \frac{\partial u_\theta}{\partial r}$$

Consequently the axial vorticity initially present only within the core is also present on the axis as well. Within $t = 35R_0^2/\Gamma_0$, fluid with azimuthal velocity extends from the core up to the axis. The vortex ring with a well-developed axial vortex is shown in figures 7.4(a) and (b).

Since the Gaussian profile is not an exact solution of the steady axisymmetric Navier Stokes equations, immediately after initialisation a rapid transient must occur as in the swirl-free case. In this readjustment, the vortex ring sheds fluid from the core with circulation and swirl as seen in figure 7.3(b). In order to determine if the development of the axial vortex is independent of the strong transient associated with this readjustment, a simulation was performed using a vortex ring initialised with a steady-state Euler solution which does satisfy axisymmetric Navier Stokes equations if viscous effects are neglected.

7.4.2 Vortex ring initialised with Euler solver

The simulation of the Euler solution initialised vortex ring EU2 at $Re = 1500$ is now considered. Figure 7.5 shows the contours of azimuthal vorticity and azimuthal velocity on the radial plane $\theta = 0$ during the initial stages after the vortex ring initialisation. Since the vortex ring was initialised with a solution of the steady-state Euler equations, the strong transient that occurs in the case of the Gaussian ring is not present. As in the case of the Gaussian ring the azimuthal velocity distribution expands towards the axis and an axial vortex develops by $t = 30R_0^2/\Gamma_0$. The vortex ring with the well-developed axial vortex is shown in figures 7.6(a) and (b). The structure is seen to be qualitatively similar to the Gaussian initialised ring after the formation of the axial vortex.

Therefore both Gaussian initialised and Euler-solution initialised vortex rings with swirl are seen to undergo a transfer of azimuthal velocity from the core to the axis of the vortex ring and the development of a strong, elongated, axial vortex. The formation of the axial vortex can now be explained. Due to viscous diffusion, azimuthal velocity is diffused across the entrainment bubble and transported to the rear stagnation point. A part of the fluid carrying azimuthal velocity re-enters the bubble and the rest is lost into the wake. The angular momentum of a fluid particle (ru_θ) is approximately conserved in a high Re axisymmetric flow. Therefore as the fluid particles move nearer to the axis of the vortex ring, their azimuthal velocity increases as $1/r$. But at $r = 0$ the azimuthal velocity must become zero. This is enforced by viscous diffusion generating an axial vortex. The axial velocity gradient dw/dz is positive in the vicinity of the rear stagnation point and hence stretches the axial vortex in this region.

Apart from the axial vortex, another feature of vortex ring with swirl with a developed axial vortex is the region of negative azimuthal vorticity (opposite sign to that of the core) at the head of the vortex ring and close to the axis as seen in figure 7.3 (e). The total circulation of this region of negative azimuthal vorticity increases in magnitude along with the development of the axial vortex and reaches a maximum value.

Both the development of an axial vortex and the region of negative azimuthal vorticity were also observed in the axisymmetric numerical simulations of polarised vortex rings

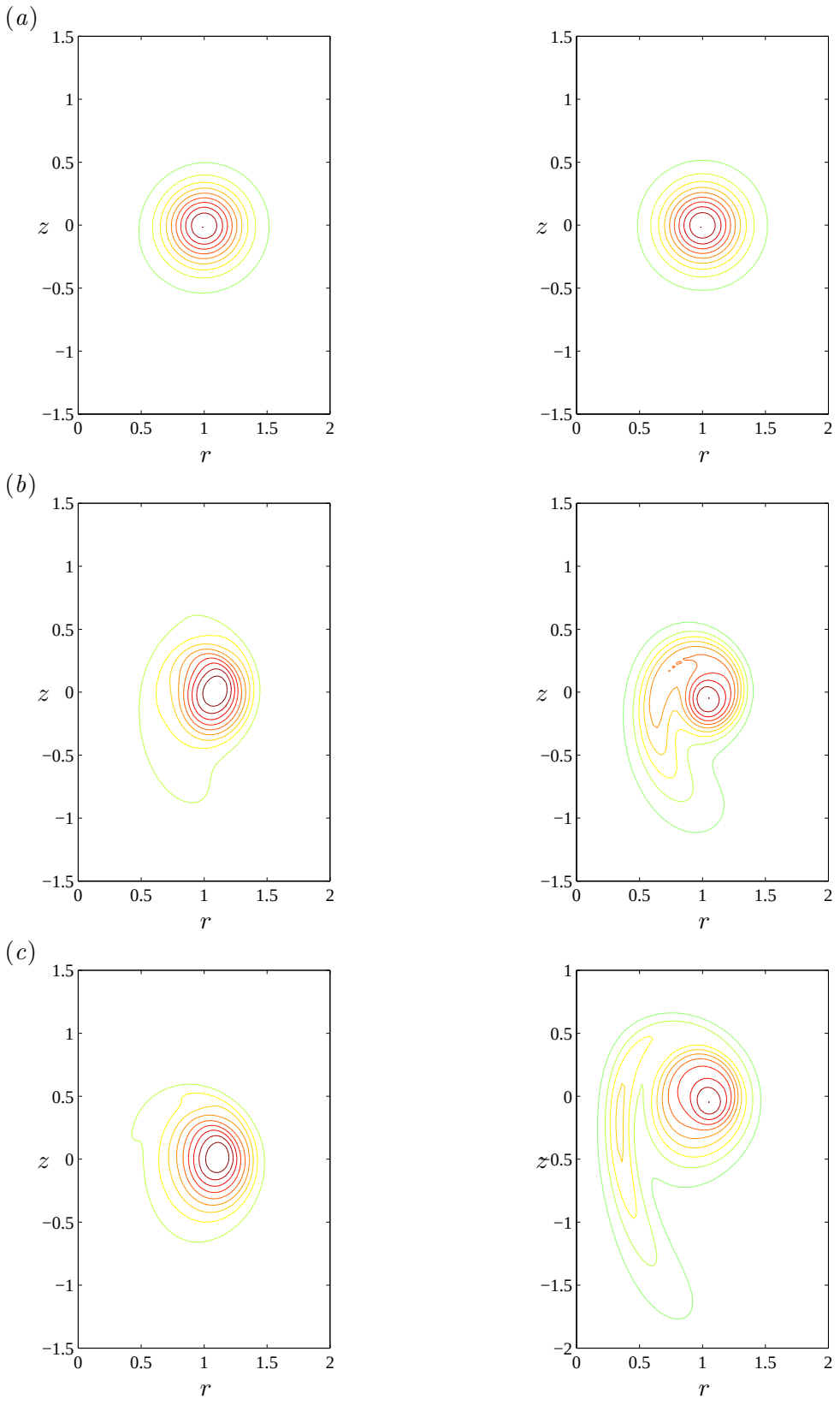

Figure 7.3: (a)–(c) See following page for caption.

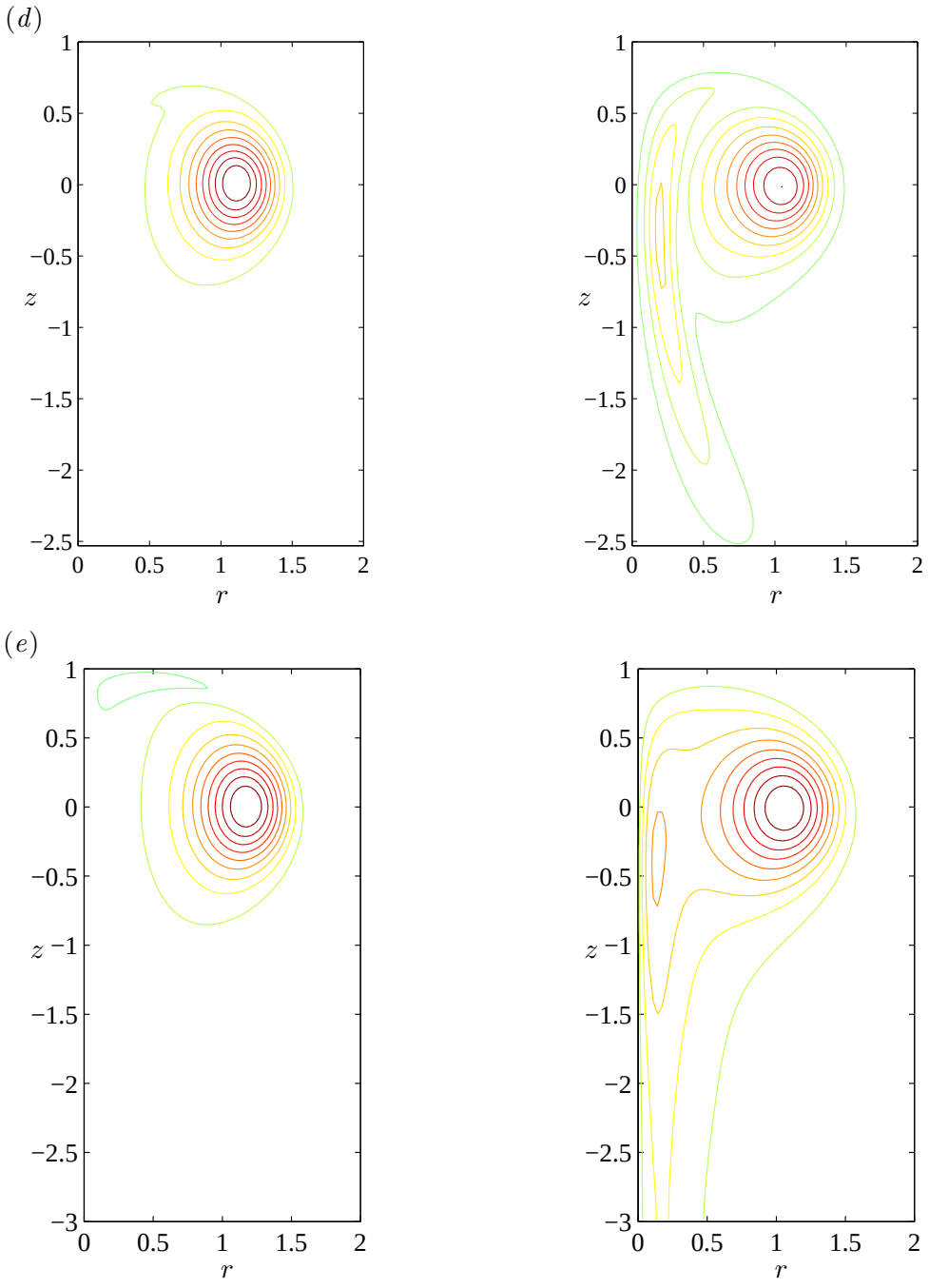

Figure 7.3: Contours of azimuthal vorticity (left) and azimuthal velocity (right) on the radial plane $\theta = 0$ at $t =$ (a) 0 (b) 5 (c) 10 (d) 15 and (e) 35 R_0^2/Γ_0 for ring GS1. Lowest contour levels of $|\omega_\theta|_{\max}/20$ and $|u_\theta|_{\max}/20$ and equal spacings of $|\omega_\theta|_{\max}/10$ and $|u_\theta|_{\max}/10$ respectively were used.

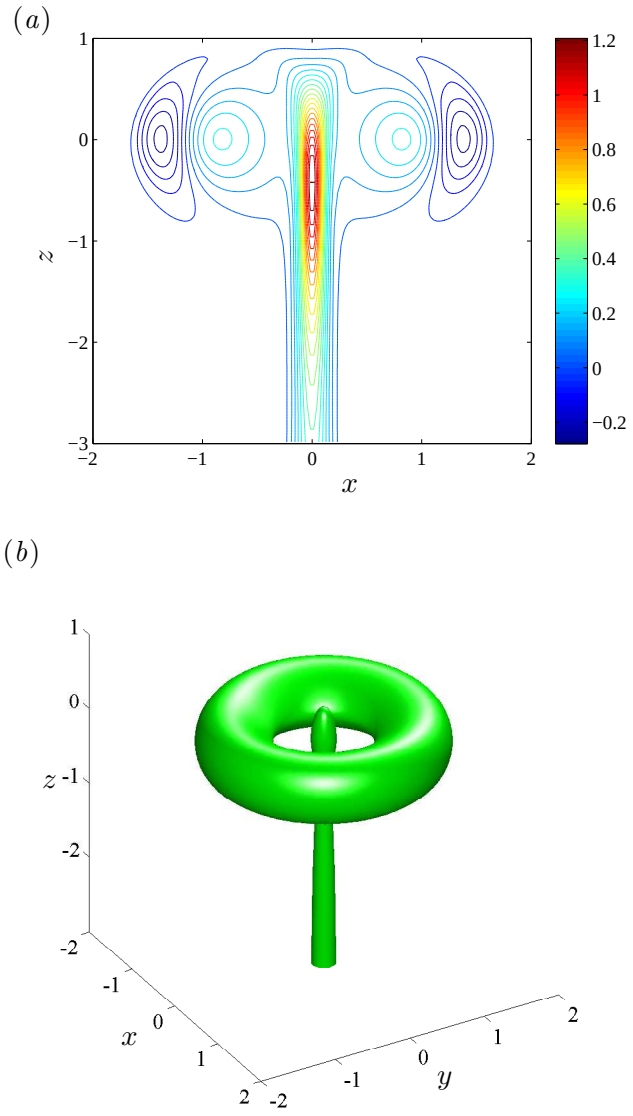

Figure 7.4: (*a*) Contours of axial vorticity (ω_z) on the plane $y = 0$. Contour levels are as indicated normalised by Γ_0/R_0^2 (*b*) Isosurface of second invariant of velocity gradient tensor, $QR_0^4/\Gamma_0^2 = -0.005$ at $t = 35R_0^2/\Gamma_0$ for ring GS1.

(which contain non-zero swirl) by Virk et al. (1994) and the formation of a vortex ring with swirl by Ooi et al. (2001). Virk et al. (1994) showed that the coupling between the swirl and meridional flow leads to the generation and destruction of ω_θ/r due to the twisting of vortex lines. Ooi et al. (2001) explained the generation of negative azimuthal vorticity as due to the tilting of the filaments of the axial vortex.

The Helmholtz equation for the azimuthal component of vorticity in axisymmetric flow is

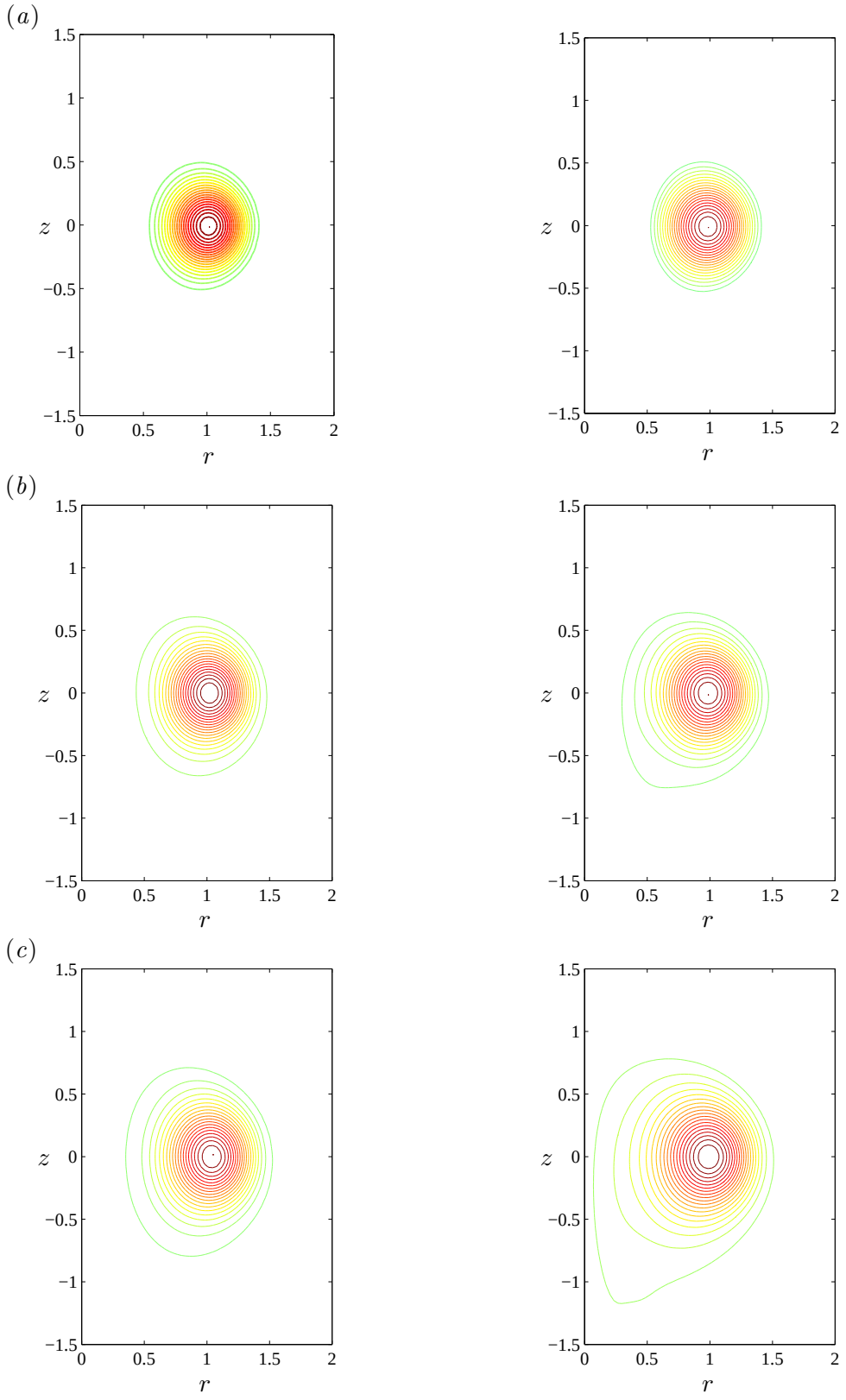

Figure 7.5: (a)–(c) See following page for caption.

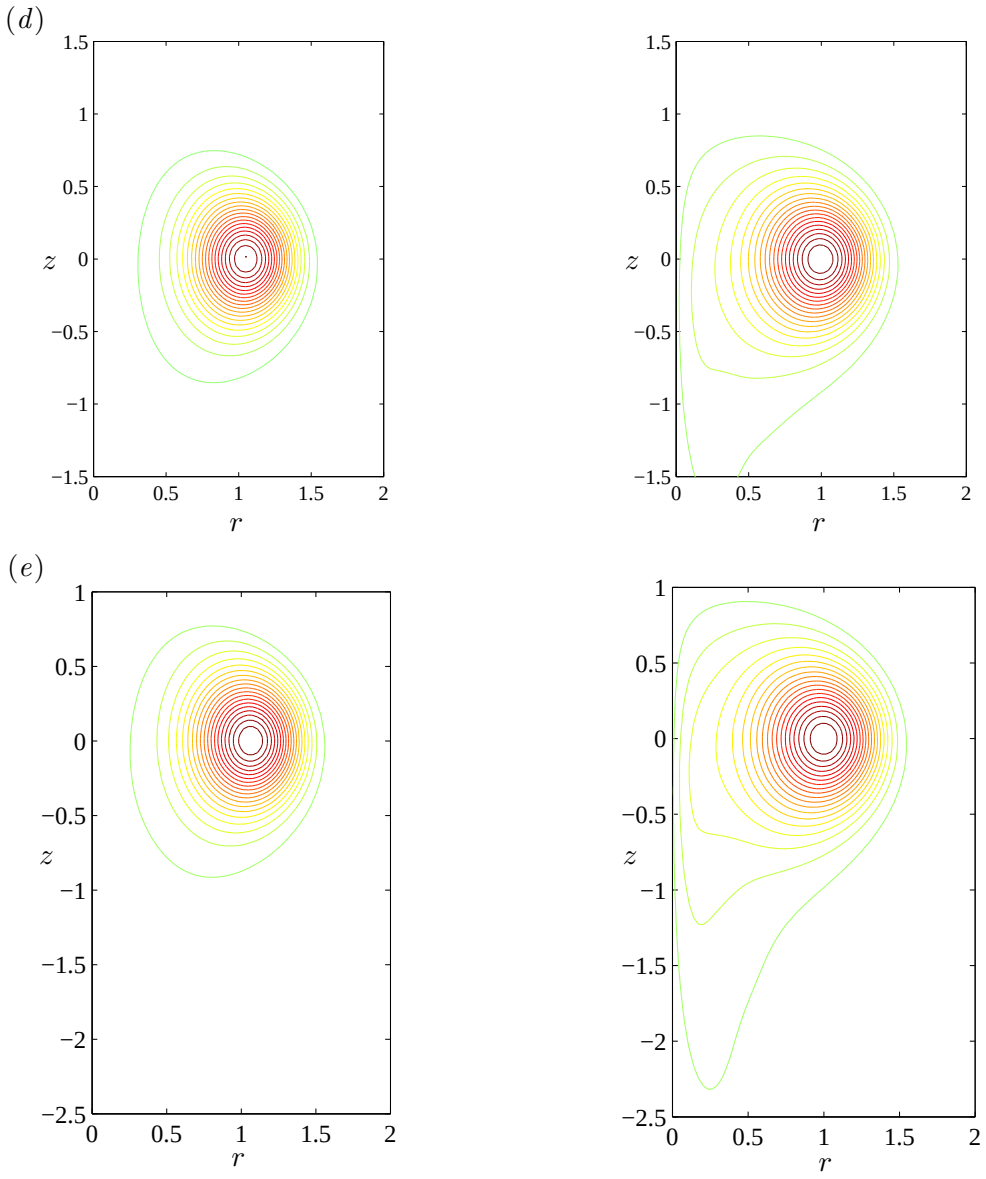

Figure 7.5: Contours of azimuthal vorticity (left) and azimuthal velocity (right) on the radial plane $\theta = 0$ at $t = (a)\ 0\ (b)\ 10\ (c)\ 20\ (d)\ 25$ and $(e)\ 30\ R_0^2/\Gamma_0$ for ring EU2. Lowest contour levels of $|\omega_\theta|_{\max}/40$ and $|u_\theta|_{\max}/40$ and equal spacings of $|\omega_\theta|_{\max}/20$ and $|u_\theta|_{\max}/20$ respectively were used.

$$\frac{D\omega_\theta}{Dt} : \frac{\partial \omega_\theta}{\partial t} + v_r \frac{\partial \omega_\theta}{\partial r} + v_z \frac{\partial \omega_\theta}{\partial z} + \frac{v_\theta \omega_r}{r} = \omega_r \frac{\partial v_\theta}{\partial r} + \omega_z \frac{\partial v_\theta}{\partial z} + \frac{\omega_\theta v_r}{r} + \nu \left(\nabla^2 \omega_\theta - \frac{\omega_\theta}{r^2} \right) \quad (7.7)$$

Figure 7.8(a) shows the contours of the sum of the vortex tilting terms (the first two terms on the right hand side). The vortex lines are tilted to generate negative and positive azimuthal vorticity at the front and rear halves of the vortex core respectively. In the region ahead of the vortex ring core near the axis, due to the negative axial gradient of the azimuthal velocity, the vortex filaments in the axial vortex are tilted towards

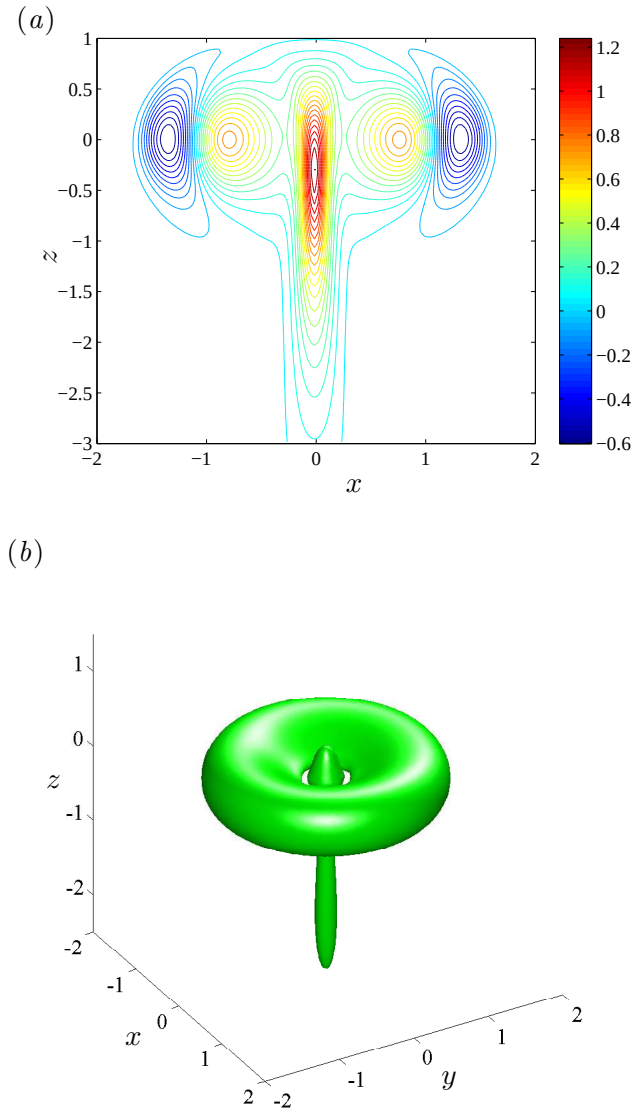

Figure 7.6: (*a*) Contours of axial vorticity (ω_z) on the plane $y = 0$. Contour levels are as indicated normalised by Γ_0/R_0^2 (*b*) Isosurface of second invariant of velocity gradient tensor, $QR_0^4/\Gamma_0^2 = -0.005$ at $t = 35R_0^2/\Gamma_0$ for ring EU2.

the negative azimuthal direction, generating negative azimuthal vorticity. Similarly the radial vortex filaments ahead of the vortex ring core extending from the axis to the outer edge of the core are also tilted towards the negative azimuthal direction due to a negative radial gradient of azimuthal velocity.

Figure 7.8(b) shows the vortex filament structure of a vortex ring with swirl with an axial vortex illustrating the tilting of the vortex lines generating negative azimuthal vorticity.

Once established, the axial vortex is a persistent and robust feature of the vortex ring with swirl.

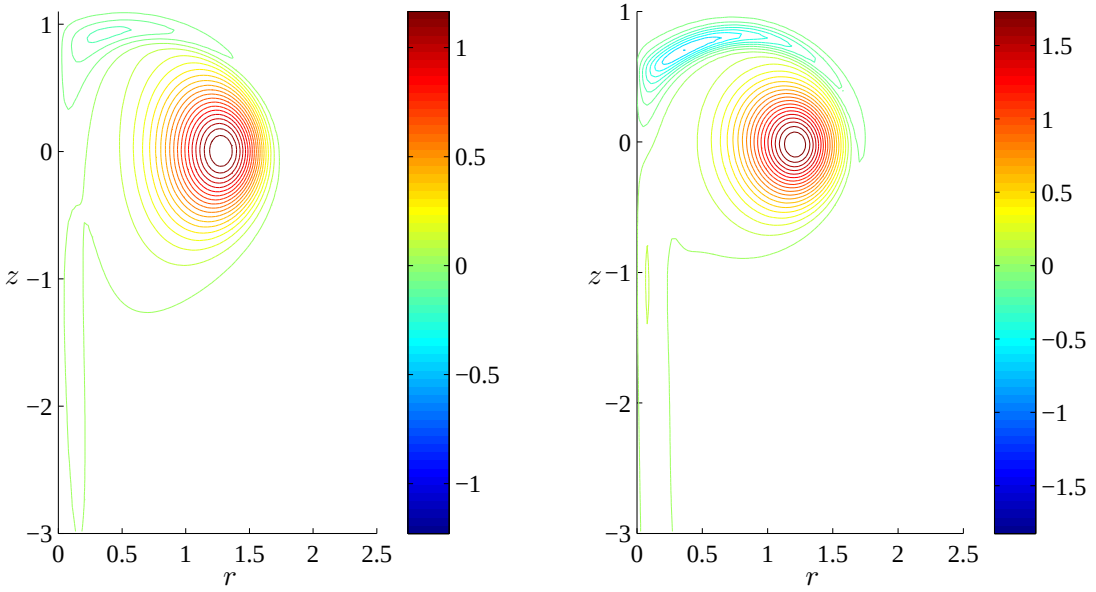

Figure 7.7: Contours of azimuthal vorticity on the radial plane $\theta = 0$ at $t = 70R_0^2/\Gamma_0$ for the Gaussian initialised vortex ring GS1 (left) and the Euler solution initialised ring EU2 (right). The contour levels are normalised by Γ_0/R_0^2.

7.5 Evolution of angular impulse

Figure 7.9 shows the histories of the angular impulse ($\mathcal{A}$) for all the vortex rings listed in table 7.1 at $Re = 1500$. The total angular impulse in the flow field must be conserved. However, as the vortex ring propagates fluid with angular momentum is shed into the wake. Consequently the angular impulse associated with the vortex ring alone as measured by using a logging domain as described in section 7.2 must decrease. The loss of fluid with angular momentum begins to be logged only after the initial wake leaves the logging domain. Therefore for a small initial period the angular impulse is indicated as constant (as seen in figure 7.9), but falls rapidly as the initial wake passes out of the logging domain. The length of this time period depends on the propagation speed of the vortex ring and the step down in angular impulse indicates the strength of the wake. For the Gaussian initialised vortex rings, the initial rate of decrease of angular impulse when the initial wake leaves the logging domain is higher compared to the Euler solution initialised vortex rings. This is due to the fact that the Gaussian initialised rings undergo a strong initial readjustment shedding fluid with azimuthal vorticity and azimuthal velocity (as described in section 7.4) unlike the Euler rings. After the fluid shed during the readjustment exits the logging domain, the rate of change of $\mathcal{A}$ is more gradual. For the Gaussian initialised vortex ring with $S = 1.0$, a significantly large reduction in angular impulse occurs at a rapid rate of decrease at $t \simeq 15R_0^2/\Gamma_0$ when the wake begins to exit the logging domain. The flow field associated with this ring is

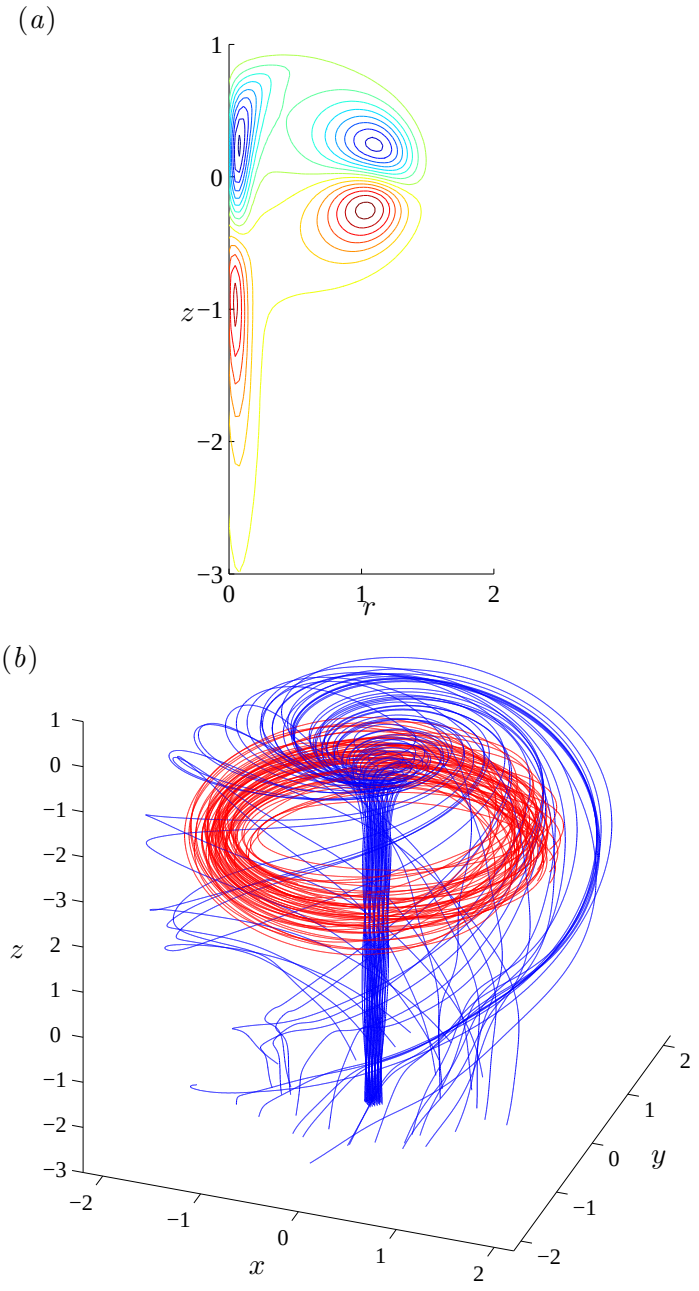

Figure 7.8: (a) Contours of the sum of the vortex tilting terms from 7.7 for ring GS1 at $t = 40R_0^2/\Gamma_0$. The contour levels are normalised by Γ_0/R_0^2. (b) Vortex filament structure of a vortex ring with swirl after the formation of the axial vortex. The filaments with a starting location within the axial vortex are coloured blue and the filaments located close to the centre of the vortex core are coloured red. The direction of vorticity within the axial vortex is along the $+z$ direction.

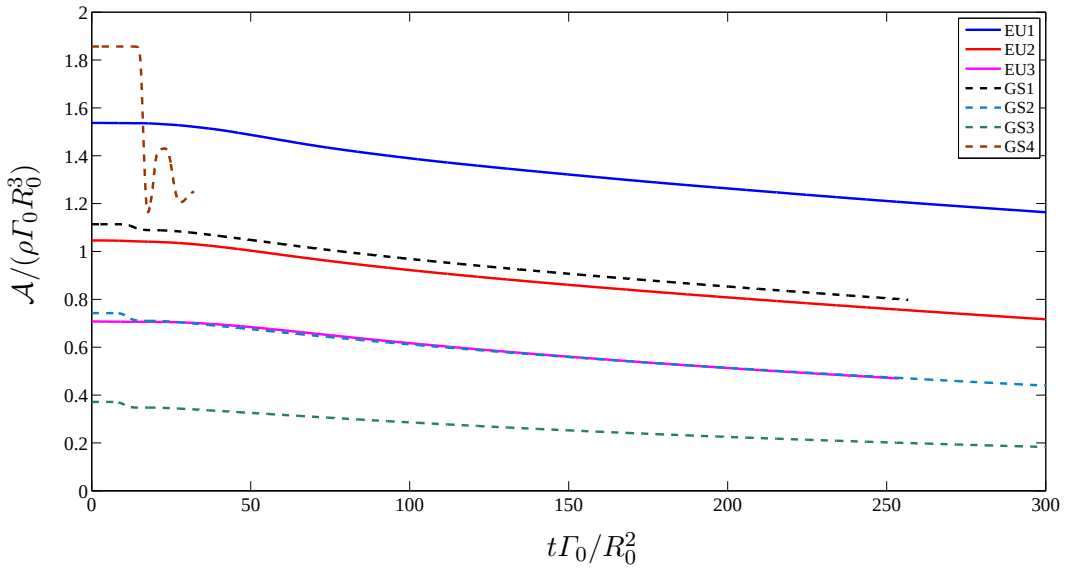

Figure 7.9: Evolution of the angular impulse with time for the different Euler solution initialised vortex rings (solid) and the Gaussian initialised (dashed) vortex rings with swirl at $Re = 1500$.

investigated separately in section 7.6. The subsequent gradual decay of angular impulse is due to continuing loss to the wake.

Although figure 7.9 suggests that it might be possible to collapse the curves by finding a suitable scaling law, initial attempts did not find a convincing collapse, but did not rule one out either. It was decided to redirect efforts towards investigation of the instabilities and breakdown of swirling vortex rings.

7.6 Swirl limit

In this section the existence of a maximum limit for the amount of swirl on a vortex ring is investigated. The numerical Euler solver imposes an implicit limit on the angular impulse of the vortex rings that can be generated as steady solutions to the Euler equations. Among the vortex rings obtained for a given value of the parameter α, the Beltrami vortex ring with $\beta = 0$ has the maximum swirl. But for the Gaussian initialised vortex rings, by varying the swirl parameter S the initial angular impulse can be varied independently and without limit. This provides a means of testing for the existence of a maximum limit for the swirl by initialising with successively higher values of swirl and looking for a rapid readjustment to a lower swirl level. Gaussian initialised vortex rings with swirl with initial slenderness ratio, $\delta_0/R_0 = 0.3$ and swirl parameters $S = 0.3$ (GS1), $S = 0.4$ (GS2), $S = 0.6$ (GS3) and $S = 1.0$ (GS4) are used in this study.

In section 7.5 the histories of the angular impulse $\mathcal{A}$ of the Euler solution initialised and Gaussian initialised vortex rings at $Re = 1500$ are presented. The Gaussian initialised

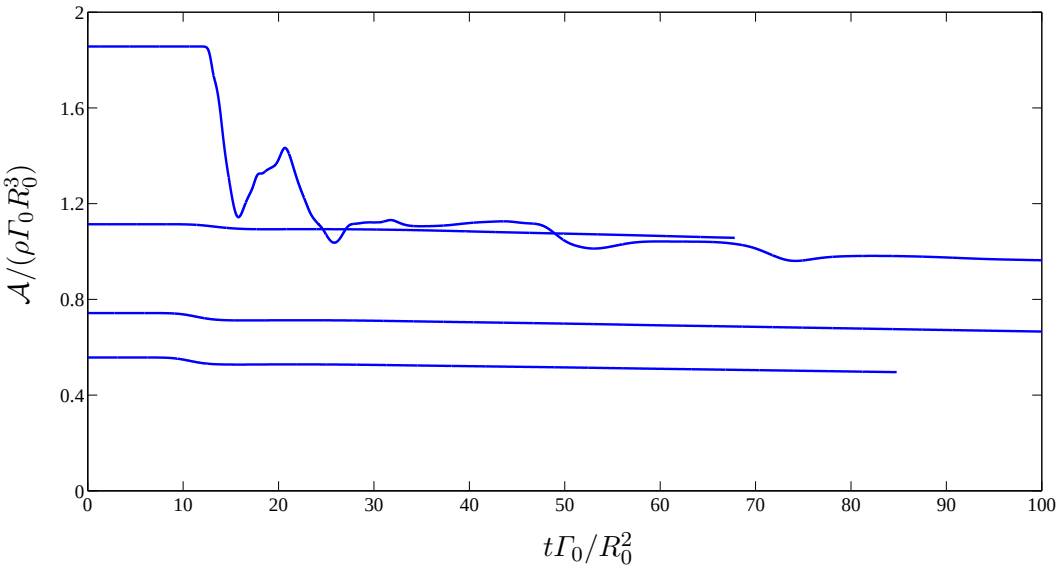

Figure 7.10: Evolution of the angular impulse with time for the Gaussian initialised vortex rings with swirl parameter $S = 0.3, 0.4, 0.6, 1.0$ at $Re = 3000$.

rings (except GS4) exhibit small steps at $t \sim 10R_0^2/\Gamma_0$ as discussed in section 7.5. A large step decrease in angular impulse is observed for the vortex ring GS4 with the highest swirl. Corresponding histories of the angular impulse at $Re = 3000$ for the Gaussian initialised vortex rings are shown in figure 7.10. As in the case at the lower Reynolds number, a large, rapid decrease in angular impulse occurs for the high swirl ring GS4 as its wake and adjustment products initially exit the logging domain. The reason for this large step is investigated below. In the following the $Re = 3000$ results alone are considered although the $Re = 1500$ results are qualitatively similar.

The evolution of the vortex ring is visualised using isosurfaces of the second invariant of the velocity gradient tensor and contours of azimuthal vorticity on a radial plane (figure 7.11). The observed flow can be explained as follows: Fluid with an azimuthal component of velocity is subject to a centrifugal acceleration which must be balanced by a radial pressure gradient. If we suppose that for vortex rings with swirl a limit exists for the maximum amount of swirl for a particular geometry, then for values of swirl above the limiting value the radial pressure gradient would be insufficient to balance the centrifugal acceleration of the swirling flow. This would result in rapid ejections of fluid with azimuthal velocity from the vortex ring as seen in figures 7.11(a),(b),(c) in the form of a jet-like flow directed radially outwards and downstream of the vortex ring. The swirl within the vortex ring (tracked by the angular impulse) is thereby reduced to a value below the maximum limit. The de-swirling phase naturally stops when $\mathcal{A}$ is below the upper limit. But there may be an overshoot and the final value may be below the upper limit. The drop of angular impulse of ring GS4 at $t \sim 15R_0^2/\Gamma_0$ (seen in figure 7.10) corresponds to the exit of the ejected fluid carrying azimuthal velocity from the logging domain at the $z = -2R_0$ plane. The shape of the ejected wake at this time is

shown in figure 7.11(e). The size of the drop indicates the amount of angular momentum ejected by the swirl readjustment. Subsequently the decay rate of angular impulse is significantly slower and similar to the case of the other vortex rings thus confirming that the drop in angular impulse corresponds to a de-swirl below an upper limit swirl.

At $t \simeq 12R_0^2/\Gamma_0$, new features begin to develop. The cross-section of the core of the vortex ring (visualised by the contours of azimuthal vorticity) is deformed into a shape with three lobes. The toroid of the vortex ring also begins to twist about the core centreline with the amplitude of the twist increasing along the azimuth of the ring. Due to the simultaneous deformation and twisting of the vortex ring, strands of vorticity begin to detach from the surface. When the strands of vorticity extend beyond the entrainment bubble, they are advected downstream in the form of hairpin vortices (figure 7.11(e)).

The vortical structure on the remaining ring is suggestive of an instability with a helical shape and is likely to depend on the level of swirl and/or the Reynolds number. The possibility of instabilities due to swirl is investigated in detail in chapter 8.

The evolution of the vortex ring and the vortical structures formed are similar to one of the vortex rings from the results of Cheng et al. (2010) (third row in their figure 2.16) who had also performed simulations of vortex rings with swirl initialised with Gaussian distributions of vorticity and velocity. Nearly all the vortex rings with swirl presented in their study underwent a similar evolution. Based on the present work, we can infer that nearly all the vortex rings in their study have angular impulse above the maximum limit. Therefore rather than representing the properties of a typical vortex ring with swirl, the flows in their study can be interpreted as rapid de-swirling readjustments.

7.7 Conclusions

After initialisation, both Euler solution initialised vortex rings with swirl and vortex rings with Gaussian distributions of azimuthal vorticity and azimuthal velocity, with angular impulse below an upper limit, develop an axial vortex and an associated region of negative azimuthal vorticity at the head of the vortex ring near the axis.

The formation of the axial vortex occurs as follows. Azimuthal velocity is diffused across the entrainment bubble and a part of the fluid carrying azimuthal velocity re-enters the bubble near the rear stagnation point. The azimuthal velocity increases as $1/r$, but must become zero at $r = 0$. This is enforced by viscous diffusion generating the axial vortex. The axial vortex, after its development is a persistent and robust feature of the vortex ring with swirl. As the vortex ring propagates, it gradually sheds angular momentum into the wake.

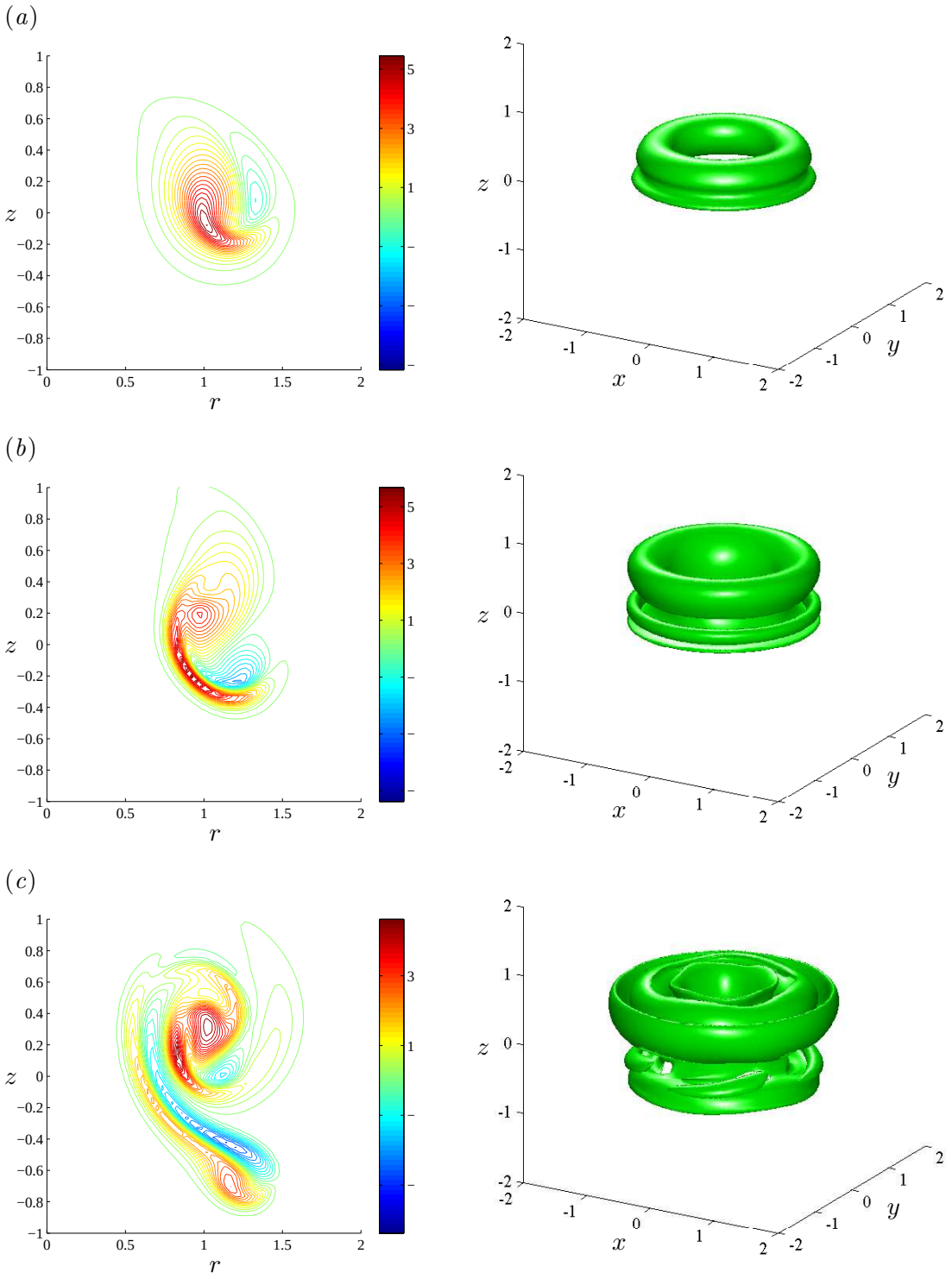

Figure 7.11: (a)–(c) See following page for caption.

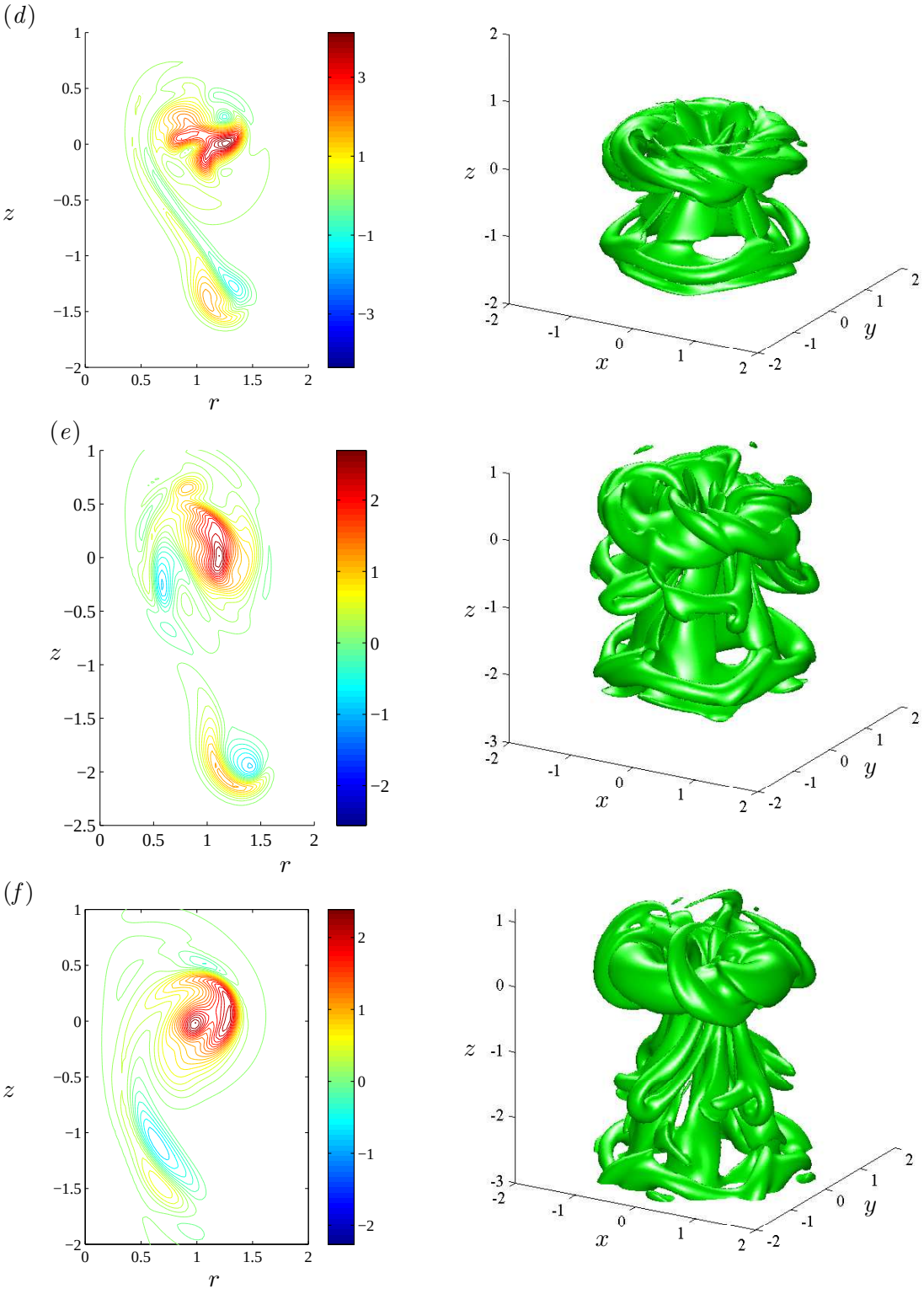

Figure 7.11: Contours of azimuthal vorticity on the radial plane $\theta = 0$ (left, contour levels normalised by Γ_0/R_0^2) and isosurface of Q (right, $QR_0^4/\Gamma_0^2 = -0.005$) at $t =$ (a) 2 (b) 4 (c) 8 R_0^2/Γ_0 (d) 12 (e) 18 (f) 24 R_0^2/Γ_0 for ring GS4.

An upper limit exists for the amount of swirl on a vortex ring. A vortex ring initialised with swirl above this limit undergoes a rapid de-swirling readjustment ejecting fluid with azimuthal velocity. The angular impulse of the vortex ring reduces to a level below the limit and subsequently decays slowly.

Chapter 8

Vortex rings with swirl: Instability

In this chapter DNS of a helical instability occurring in vortex rings due to swirl is presented. The instability appears at high Reynolds numbers. The modal structure of the instability is identified for different vortex rings and shown to be determined by the slenderness ratio. The numerical approach and initial setup (figure 8.1) used here is the same as in section 4.1 to study classical vortex rings in unbounded flow.

The details of the simulations are presented in section 8.1. The adequacy of the numerical resolution is demonstrated in section 8.2. In section 8.3 the evolution of a vortex ring with swirl at two different Reynolds numbers is discussed. The fully developed helical instability is shown to occur at the higher Reynolds number. In section 8.4 a numerical analysis is developed to determine the exact modal structure of the instability. In section 8.5 helical instabilities with different mode shapes are presented. The dependence of the mode shape of the instability on the geometric parameters of the vortex ring is shown in section 8.6. The final conclusions are summarised in section 8.7.

8.1 Simulation details

In all the simulations discussed in this chapter, the cubic domain size was $8R_0 \times 8R_0 \times 8R_0$ (along x, y, z directions). The timestep was chosen such that the Courant-Freidrichs-Lewy (CFL) number remained below 0.20 throughout the simulation to ensure numerical stability.

The Euler solution initialised vortex rings with swirl and Gaussian initialised vortex rings with swirl used in this chapter are listed in table 8.1 along with the defining parameters. The details of the initialisation methods are provided in section 7.1.1. Both

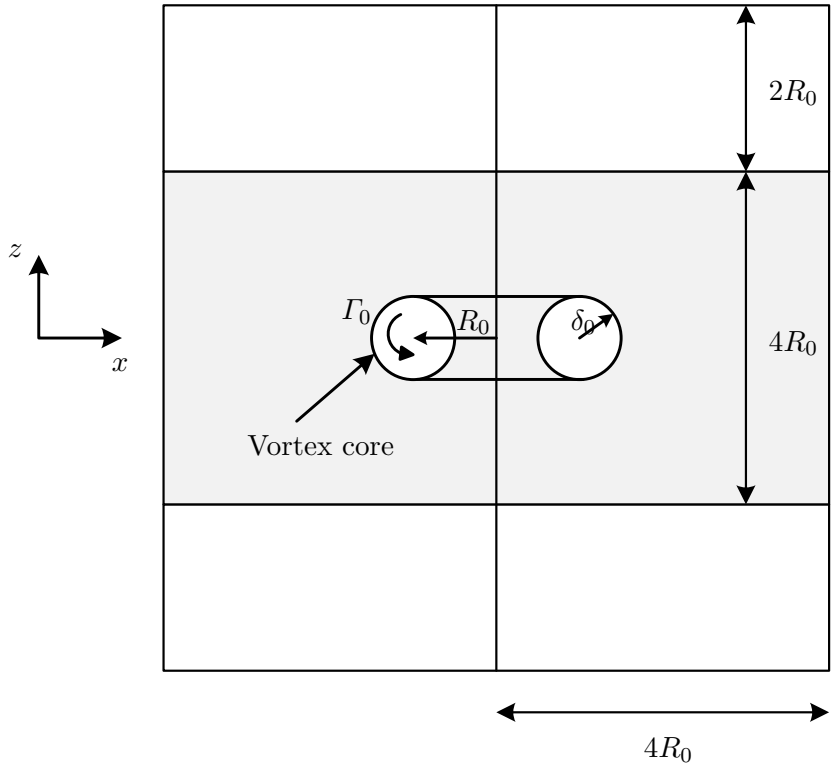

Figure 8.1: Schematic of the computational domain for the study of instability in vortex rings due to swirl. The shaded region corresponds to the logging domain.

Vortex ring	Type	Parameters	Ring characteristics	
			δ_0/R_0	$\mathcal{A}/(\Gamma_0 R_0^3)$
EU4	Euler solution	$\alpha = 100, \beta = 0$	0.21	1.06
EU5	Euler solution	$\alpha = 40, \beta = 0$	0.32	1.73
EU2	Euler solution	$\alpha = 60, \beta = 35$	0.23	1.05
GS3	Gaussian	$S = 0.60$	0.30	1.11
GS5	Gaussian	$S = 1.00$	0.20	0.81

Table 8.1: Vortex rings used to study instability due to swirl.

Euler solution and Gaussian initialised vortex rings are shown to develop the helical instability.

Table 8.2 lists the simulations discussed in this chapter along with the Reynolds number and grid resolution used in each case. Simulations S1 and S2 performed using the same vortex ring EU4 are used to show the effect of the Reynolds number on the development of the instability. A fully developed instability occurs in all the cases excepting S1. The parameters of the vortex rings at the time of the instability are used to investigate their relation to the modal structure of the instability.

An initial random noise level was defined on the flow in order to equally excite all possible

Simulation	Vortex ring	Reynolds number	Grid
1	EU4	1500	$512 \times 512 \times 512$
2	EU4	3000	$768 \times 768 \times 768$
3	EU5	3000	$768 \times 768 \times 768$
4	GS3	3000	$768 \times 768 \times 768$
5	GS5	3000	$768 \times 768 \times 768$
6	EU2	4500	$768 \times 768 \times 768$

Table 8.2: Vortex ring, Reynolds number and grid resolution used for the simulations of instability due to swirl.

modes before allowing them to grow. An initial perturbation was imposed in the form of small local, radial displacements of the vortex core. The radial displacement applied is a sum of 32 Fourier modes, each with amplitude $\eta = 0.0005R_0$ and random phase given by

$$\begin{aligned} \Delta R(\theta) &= \eta \sum_{n=1}^{32} \left(A_n \sin(n\theta) + B_n \cos(n\theta)\right) \\ R(\theta) &= R_0 + \Delta R \end{aligned} \tag{8.1}$$

where $A_n^2 + B_n^2 = 1$.

This is imposed following Archer et al. (2008) in which the ring geometry is perturbed.

8.2 Adequacy of numerical resolution

The adequacy of the numerical resolution for the simulations of flow instability in this chapter is demonstrated for an example case of vortex ring EU4 at $Re = 3000$ performed on a grid with $768 \times 768 \times 768$ points.

The energy balance between the volume integrated kinetic energy per unit mass with respect to the co-moving reference frame K, the volume integrated rate of kinetic energy dissipation ϵ_K and the total volume integrated kinetic energy flux out of the domain F_K (see section 4.3.1 for details) given by

$$-\frac{\mathrm{d}K}{\mathrm{d}t} = \epsilon_K + F_K\,, \tag{8.2}$$

was tracked with time. Figure 8.2 compares the histories of the quantities represented by left and right hand sides of this equation for this case. A period of rapid enstrophy growth occurs at $t \simeq 10R_0^2/\Gamma_0$. The difference between the two sides remains less than $1 \times 10^{-5}\Gamma_0^3/R_0$ up to $t = 10R_0^2/\Gamma_0$ and less than $1 \times 10^{-4}\Gamma_0^3/R_0$ throughout the entire

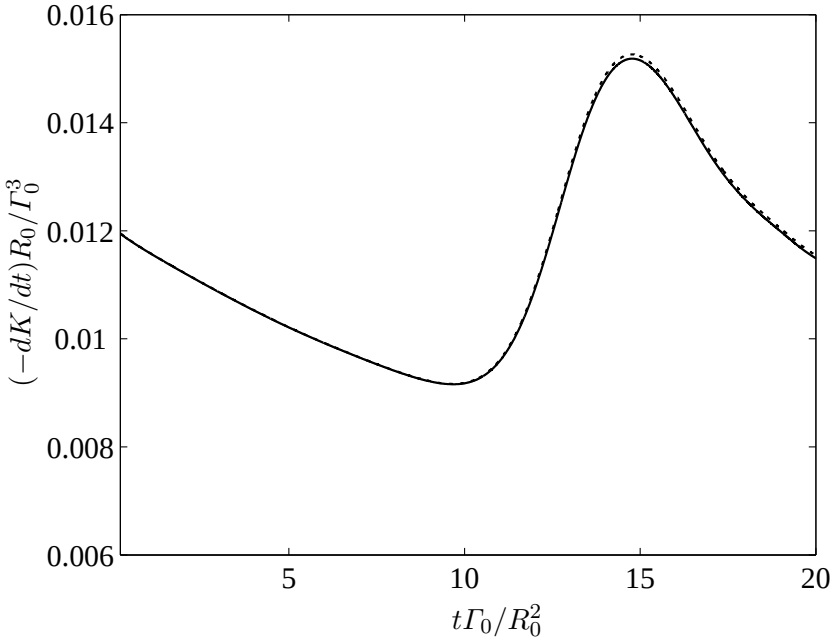

Figure 8.2: Comparison of histories of - - - - Rate of decrease of volume-integrated kinetic energy $(-\mathrm{d}K/\mathrm{d}t)$ and ——— Sum of volume-integrated rate of dissipation and energy flux $(\epsilon_K + F_K)$ for the simulation of vortex ring EU4 at $Re = 3000$.

simulation reaching the maximum value at the enstrophy peak demonstrating that the spatial discretisation error is negligible throughout.

8.3 Euler solution initialised vortex ring EU4 at different Reynolds numbers

8.3.1 Re=1500

Firstly, the simulation of the Euler solution initialised vortex ring EU4 ($\alpha = 100, \beta = 0$) at the lower Reynolds number $Re = 1500$ is considered. Figure 8.3 shows the contours of azimuthal vorticity and velocity on a radial plane at different times during the simulation. The evolution up to $t \simeq 10R_0^2/\Gamma_0$ appears similar to the Euler solution initialised vortex ring described in chapter 7 (figure 7.5). However a deformation of the vortex core cross-section begins to be seen at $t \simeq 15R_0^2/\Gamma_0$. At $t = 20R_0^2/\Gamma_0$, the vortex core cross-section is significantly deformed into a near-elliptical shape and sheds fluid with azimuthal velocity towards the ring axis aiding the formation of the axial vortex. The strong deformation of the vortex core indicates the possible growth of an instability. However within $t = 40R_0^2/\Gamma_0$ the deformation is attenuated and the core cross-section regains a near-circular shape and the instability dies out.

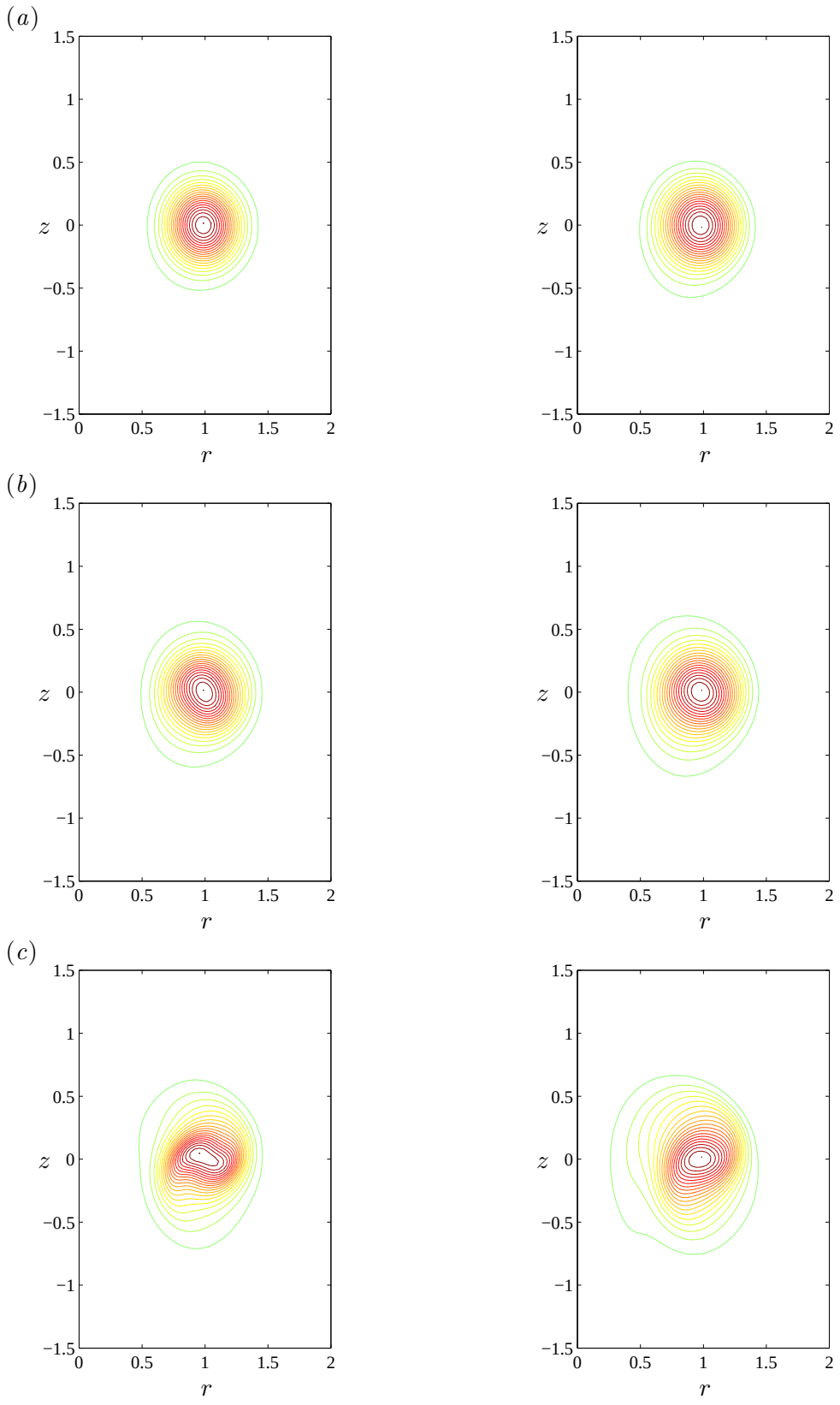

Figure 8.3: (a)–(c) See following page for caption.

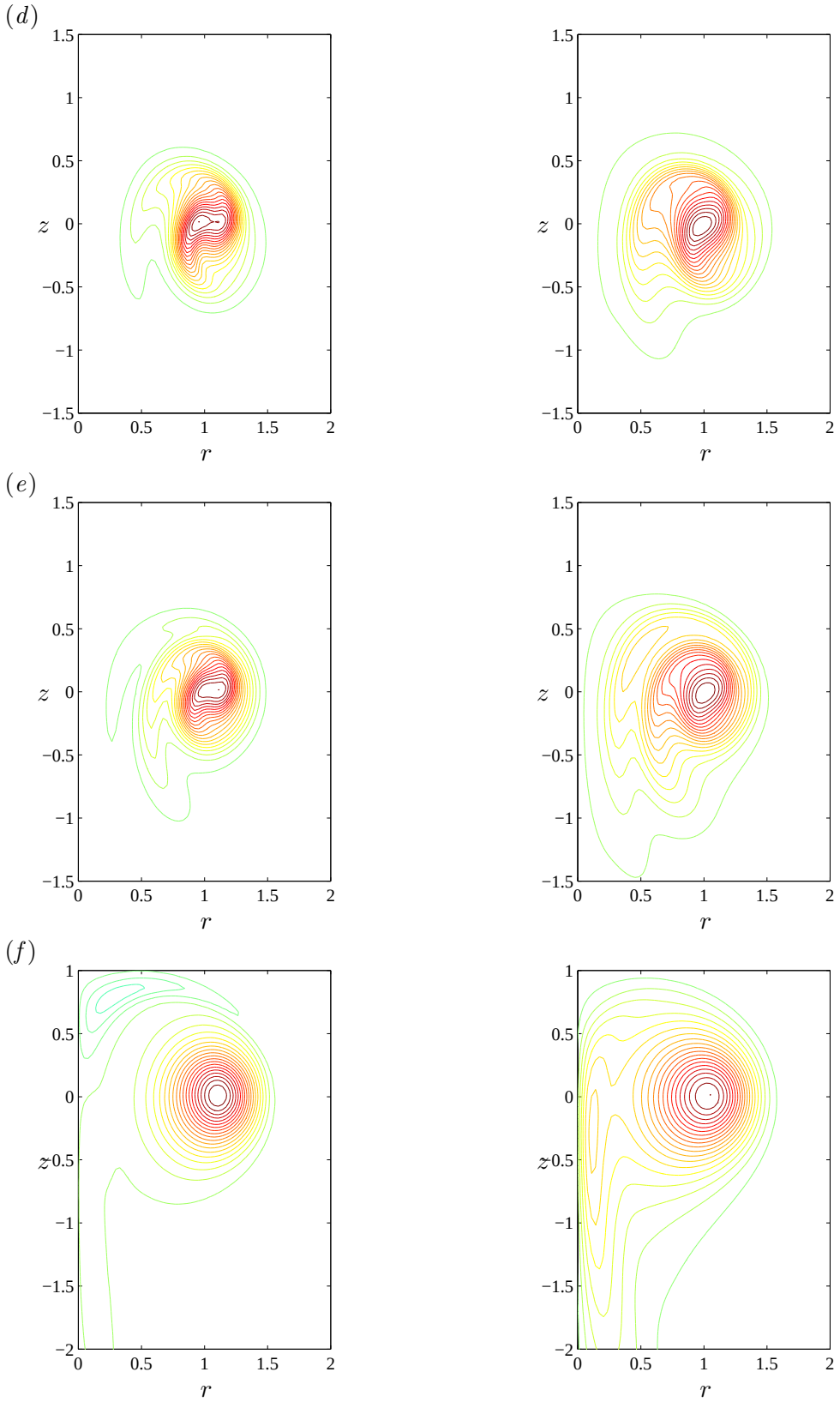

Figure 8.3: Contours of azimuthal vorticity (left) and azimuthal velocity (right) on the radial plane $\theta = 0$ at $t =$ (a) 5 (b) 10 (c) 15 (d) 20 and (e) 25 (f) 40 R_0^2/Γ_0 for ring EU4 at $Re = 1500$.

8.3.2 Re=3000

Now the simulation of the vortex ring EU4 ($\alpha = 100, \beta = 0$) at a higher Reynolds number of $Re = 3000$ is considered. At this Reynolds number a fully developed instability is found to occur.

Figure 8.4 shows the contours of azimuthal vorticity and velocity on a radial plane during the evolution of the vortex ring. As in the simulation at $Re = 1500$, the vortex core cross-section begins to appear deformed at $t = 9R_0^2/\Gamma_0$. In the present simulation however, the deformation becomes stronger and a distinct shape begins to emerge with three lobes along the core azimuth.

The isosurfaces of the second invariant of the velocity gradient tensor (Q) in figure 8.5 show that, apart from the deformation of the cross-section, the vortex core is also twisted about its centre along the ring azimuthal direction. Due to the twisting, the deformed vortex ring is no longer axisymmetric and instead acquires a helical structure. Figure 8.6 provides a front-on view of the helical structure of the deformed vortex ring at $t = 12R_0^2/\Gamma_0$.

The stretching of the vortex filaments during the vortex ring deformation leads to fine scale lobe structure and consequently in rapid enstrophy growth and a corresponding growth in the volume-integrated dissipation at $t = 10R_0^2/\Gamma_0$ as seen in figure 8.2. The rapid enstrophy growth is an indicator of the occurrence of an instability.

At later times, due to the simultaneous deformation of the core cross-section into a three lobed shape and the progressive twisting of the vortex ring, individual vortex tubes begin to detach from the surface of the vortex ring. The shape of the instability is similar to the flow behaviour observed in the case of the Gaussian initialised vortex ring with high swirl discussed in section 7.6. The structure of the instability is analysed in section 8.4.

8.4 Structure of the instability

In this section a simplified model of the geometric structure of the instability is presented as a helical wave with modes along both the core azimuthal and ring azimuthal directions. A numerical analysis of the flow field is performed to verify the model and determine the exact modal structure of the instability for the case of ring EU4 at $Re = 3000$.

The instability is described within a toroidal coordinate system whose schematic is provided in figure 8.7. The origin of the coordinate system is located at $(R, 0, 0)$ where R is the radius of the vortex ring. The coordinates are the radial distance from the centreline of the torus σ, the ring azimuth θ and the core azimuth ϕ.

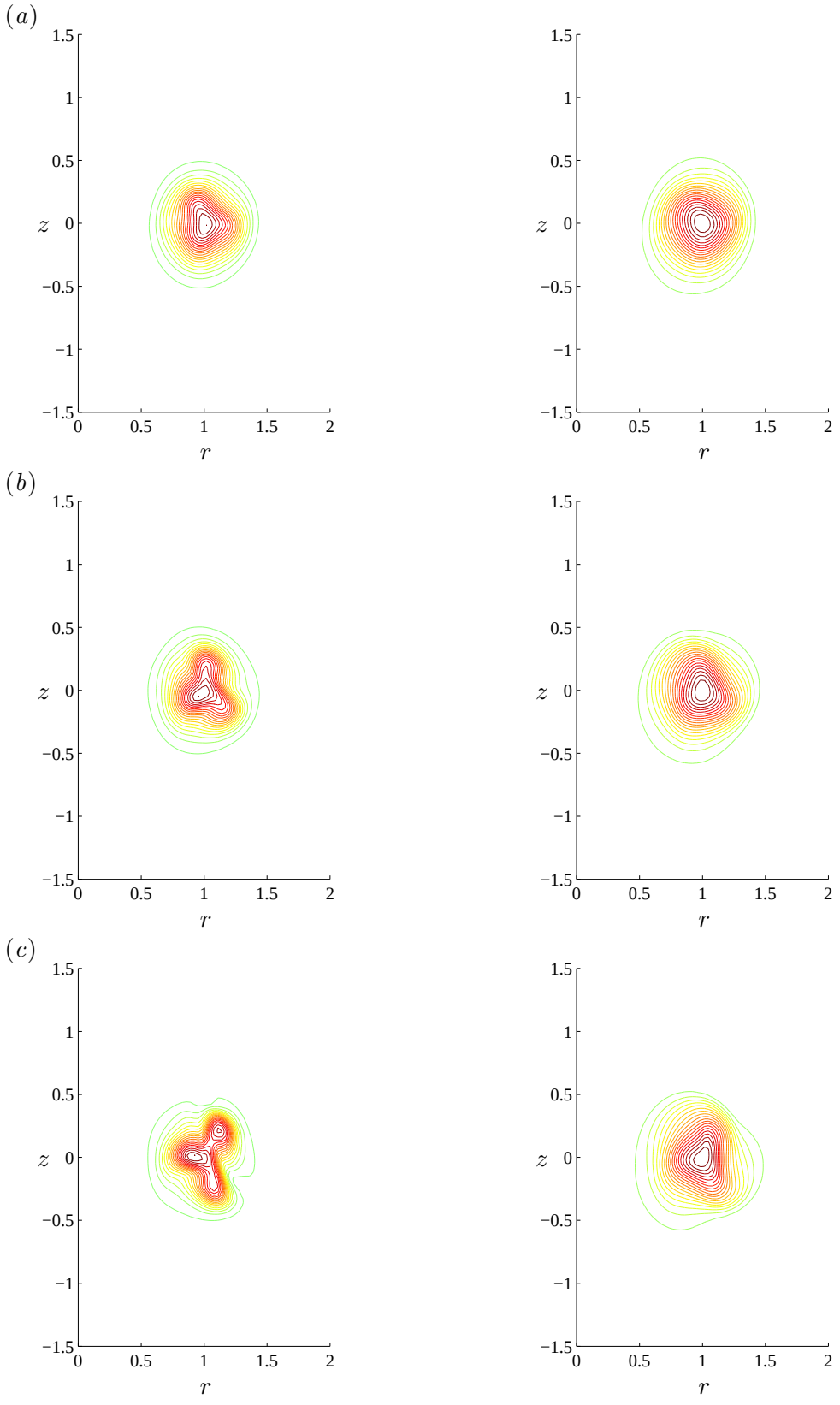

Figure 8.4: Contours of azimuthal vorticity (left) and azimuthal velocity (right) on the radial plane $\theta = 0$ at $t =$ (a) 9 (b) 10 (c) 11 R_0^2/Γ_0 for ring EU4 at $Re = 3000$.

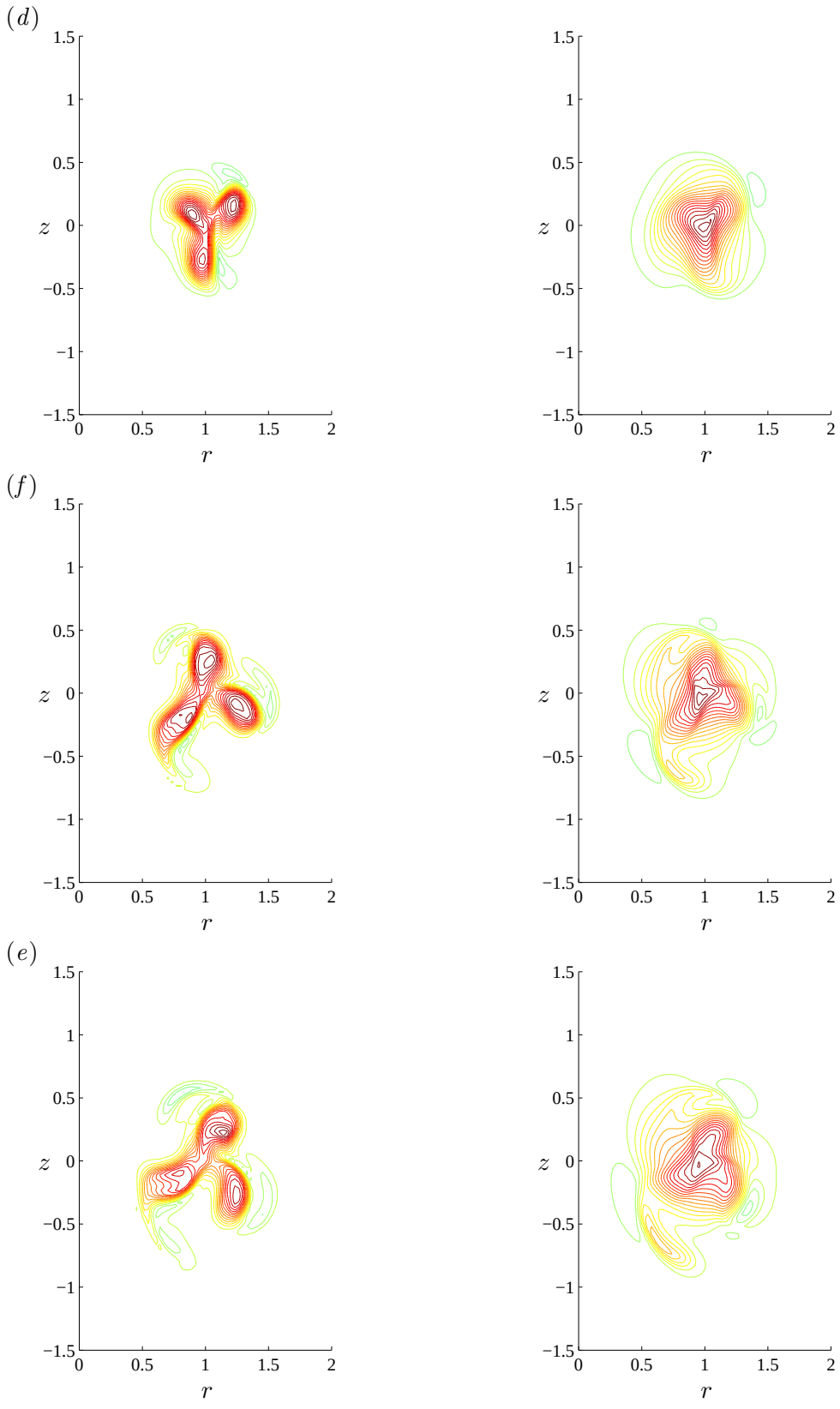

Figure 8.4: Contours of azimuthal vorticity (left) and azimuthal velocity (right) on the radial plane $\theta = 0$ at $t =$ (d) 12 (e) 14 (f) 16 R_0^2/Γ_0 for ring EU4 at $Re = 3000$.

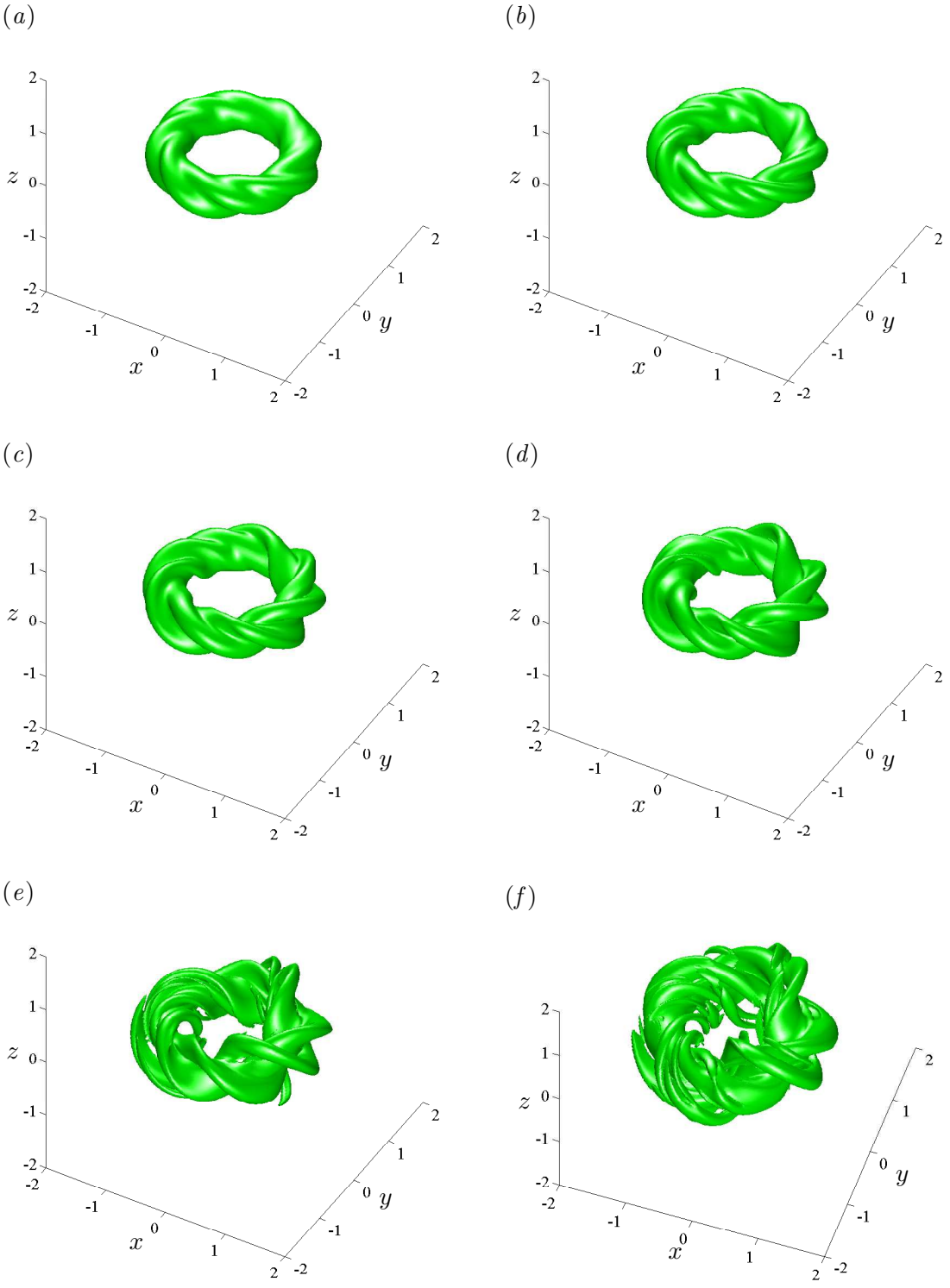

Figure 8.5: Isosurfaces of Q ($QR_0^4/\Gamma_0^2 = -0.005$) showing the growth of the helical instability for ring EU4 at $Re = 3000$ at $t =$ (a) 9 (b) 10 (c) 11 (d) 12 and (e) 14 (f) 16 R_0^2/Γ_0.

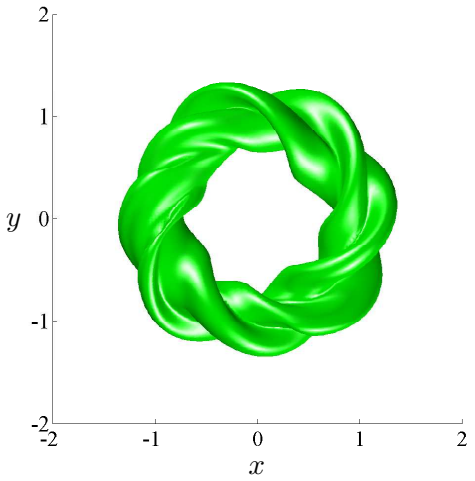

Figure 8.6: Isosurface of Q ($QR_0^4/\Gamma_0^2 = -0.005$) showing the helical structure of the instability for ring EU4 at $Re = 3000$ at $t = 12\ R_0^2/\Gamma_0$.

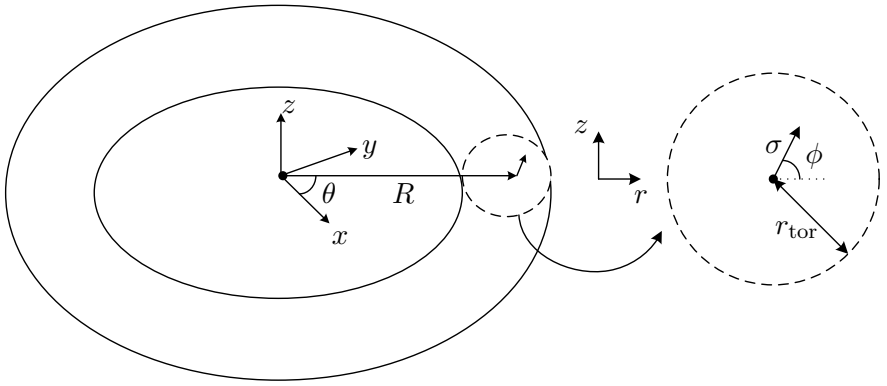

Figure 8.7: Schematic of the toroidal coordinate system.

The amplitude of the deformation of the vortex core $\xi(\sigma, \theta, \phi)$ at the ring azimuth $\theta = 0$ can be given by

$$\xi(\sigma, 0, \phi) \sim f(\sigma) \exp(in_\phi(\phi + \phi_0)) \,,$$

where n_ϕ is the 'shaping mode' associated with the deformation of the core cross-section. The instability occurring in ring EU4 at $Re = 3000$ appears to deform the core cross-section into a shape with $n_\phi = 3$ (figure 8.4).

The effect of the twisting of the core is to introduce a phase shift in ϕ with the shift increasing along the ring azimuth. By including the phase shift due to the twist, the entire deformation field can be given by

$$\begin{aligned} \xi(\sigma,\theta,\phi) &\sim f(\sigma)\exp(in_\phi(\phi+\phi_0+n_\theta\theta)) \\ &\sim f(\sigma)\exp(in_\phi(\phi+\phi_0))\exp(in_\phi n_\theta\theta)\,, \end{aligned} \tag{8.3}$$

where n_θ is the 'twisting mode' or the number of 'twists' along the circumference of the vortex ring. The periodicity of the deformation along the ring azimuthal direction ($\xi(\sigma,\theta,\phi)=\xi(\sigma,\theta+2\pi,\phi)$) requires that the product $n_\phi n_\theta$ should be an integer. Therefore although the shaping mode n_ϕ should necessarily be an integer, the twisting mode n_θ can assume fractional values if the product $n_\phi n_\theta$ is an integer. The number of twists along the circumference can be fractional due to the fact that the vortex core cross-section is symmetric with respect to a rotation in ϕ by $2\pi/n_\phi$. Therefore the vortex core cross-sections at $\phi=0$ and $\phi=2\pi_-$ can match despite a fractional twist.

If a two-dimensional Fourier transform of the velocity field is performed along the ring and core azimuthal directions to obtain the modal energy spectrum, the Fourier mode along the core azimuthal direction is n_ϕ and along the ring azimuthal direction is $n'_\theta = n_\phi n_\theta$.

A numerical analysis of the flowfield was performed at different times during the growth of the instability for the ring EU4 at $Re=3000$. The radius of the toroid was measured as the enstrophy weighted average,

$$R_\Omega = \frac{1}{2\Omega}\int_V r\omega^2 d\mathrm{V}\,. \tag{8.4}$$

The velocity field within the toroidal region with a centreline $r=R, z=0$ and radius of $r_{\mathrm{tor}}=0.5\,R_\Omega$ is interpolated onto the toroidal coordinate system with its origin located at $(x=R_\Omega, y=0, z=0)$. A two-dimensional Fourier transform was performed along the ring azimuthal and core azimuthal directions to obtain the energy spectrum. Figure 8.8 shows bar charts of the modal energy spectrum at each of the sampling times with the axes corresponding to the Fourier modes n_ϕ and n'_θ.

The $(n_\phi=2, n_\theta=2)$ mode grows initially followed by the (3,7/3) and (3,8/3) modes. After $t=5R_0^2/\Gamma_0$ the (3,7/3) and (3,8/3) modes become the fastest growing and are the dominant ones at $t=13R_0^2/\Gamma_0$.

The distribution of energy over a few isolated modes confirms the helical structure of the instability. The dominant shaping and twisting modes identified by the numerical analysis are consistent with the observed vortical structure of the instability. The shape of the deformed vortex core was seen to be a three-lobed structure in figure 8.4. In the front-on view of the instability in figure 8.6, the interference between the twisting modes 7/3 and 8/3 can be seen in the $\pi/2<\theta<\pi$ quadrant.

After the amplitudes of these modes become significant, the instability enters the non-linear phase during which the modes begin to interact generating higher order harmonics and lower order intermodulation products ($n'_\theta = 11, n_\phi = 4$ at $t = 15R_0^2/\Gamma_0$).

The numerical analysis was also performed for the evolution of ring EU4 at the lower Reynolds number ($Re = 1500$). The deformation of the vortex ring at $Re = 1500$ was found to be associated with the ($n_\theta = 2, n_\phi = 2$) mode. The (7/3,3) and (8/3,3) which are the dominant modes at $t = 13R_0^2/\Gamma_0$ at $Re = 3000$ are not significant at $Re = 1500$. The difference between the growth rates of these modes at the two Reynolds numbers is explained in section 8.6.

8.5 Helical instabilities with varying twisting and shaping modes

In this section, the helical instabilities occurring in the other vortex rings with swirl used in this work (simulations 3,4,5 and 6 from table 8.2) are presented. Both Gaussian and Euler solution initialised vortex rings with swirl are shown to develop the helical instability. The dominant instability modes in each case are determined by numerical analysis of the flowfield. The simulations in this chapter provide a set of instances of the helical instability with varying mode shapes. The relation between the parameters of the vortex ring and the mode shapes of the instability is investigated in section 8.6.

8.5.1 Euler solution initialised vortex ring EU5 at Re=3000

The simulation of the Euler solution initialised vortex ring EU5 ($\alpha = 40, \beta = 0$) at $Re = 3000$ is now presented. As in the case of ring EU4 at $Re = 3000$, a helical instability develops within $t = 40R_0^2/\Gamma_0$ deforming the vortex core cross-section and twisting the vortex core about the core centreline. Figure 8.9 shows the deformation of the vortex core cross-section into a three-lobed structure at $t = 38R_0^2/\Gamma_0$, similar to ring EU4 at $Re = 3000$. The helical structure of the instability is seen in figure 8.10. The modal energy spectrum shows that at $t = 38R_0^2/\Gamma_0$, a single dominant mode is present with ($n_\theta = 5/3, n_\phi = 3$) (figure 8.11).

8.5.2 Gaussian initialised vortex ring GS3 at Re=3000

Figures 8.12 and 8.13 show the structure of the helical instability occurring in the case of the Gaussian initialised vortex ring GS3 ($S = 0.6, \delta_0/R_0 = 0.3$) at $Re = 3000$ and the corresponding modal energy spectrum respectively. Due to the strong initial readjustment from the Gaussian profile, fluid with azimuthal velocity is shed towards the axis

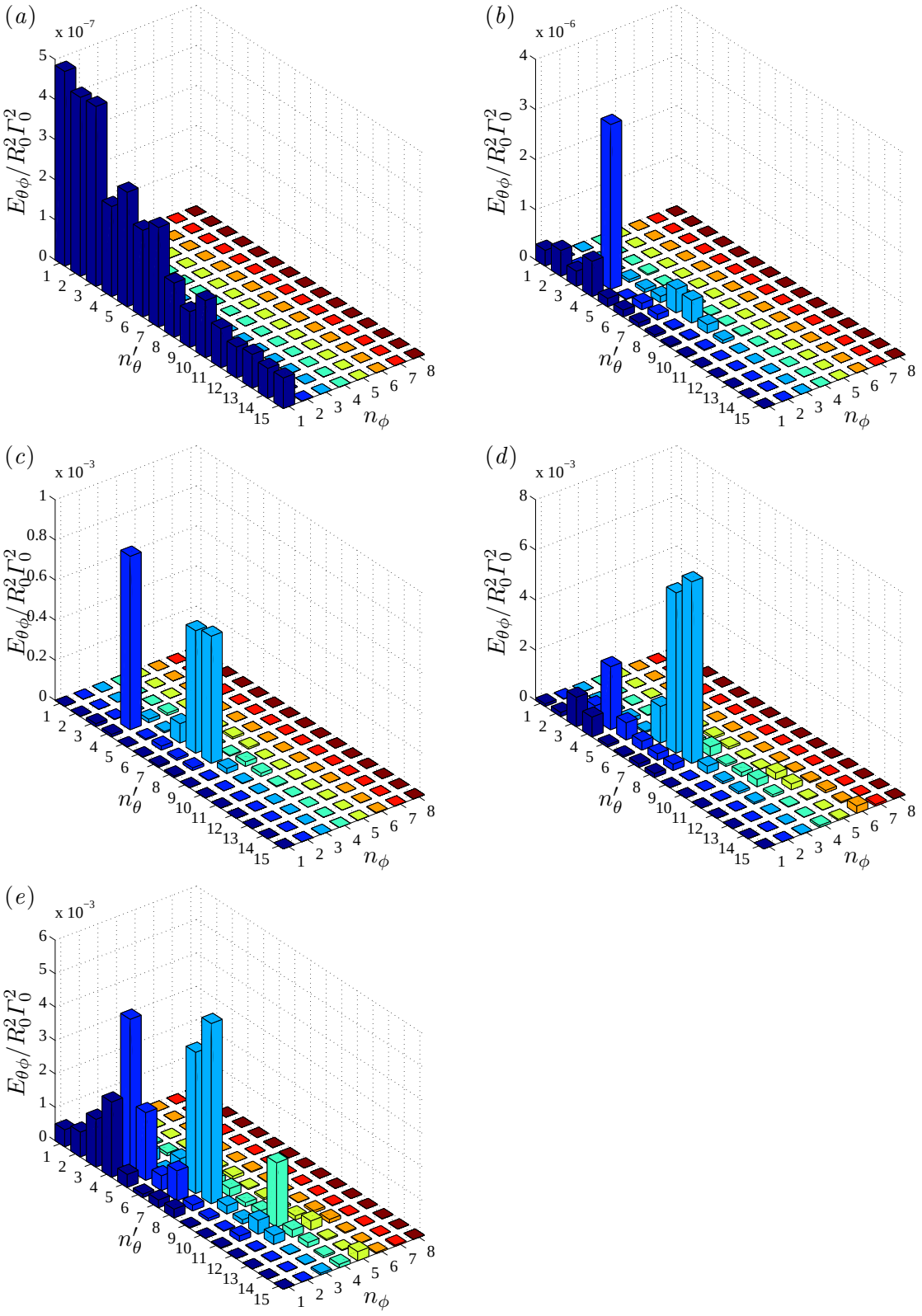

Figure 8.8: Modal energy spectrum for ring EU4 at $Re = 3000$ at $t = (a)$ 0 (b) 5 (c) 10 (d) 13 and (e) 15 R_0^2/Γ_0. The shaping and twisting modes are n_ϕ and n_θ respectively.

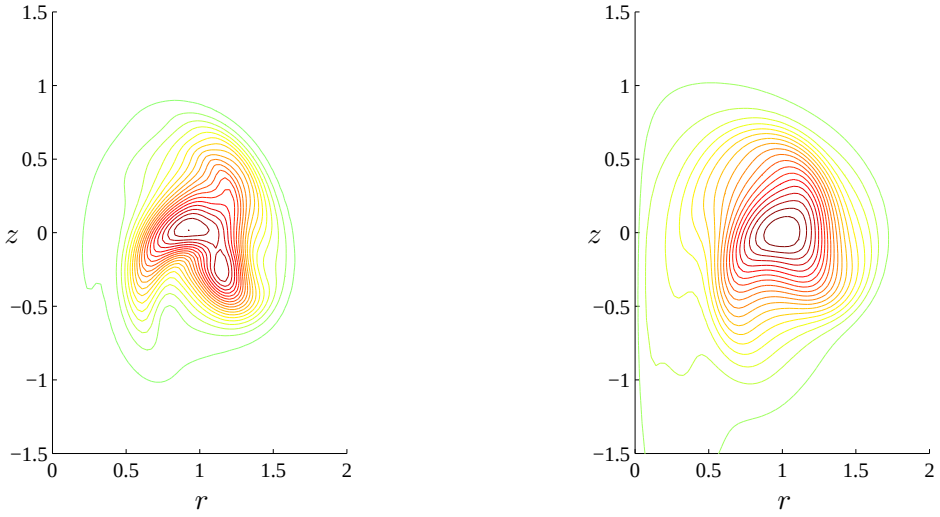

Figure 8.9: Contours of azimuthal vorticity (left) and azimuthal velocity (right) on the radial plane $\theta = 0$ at $t = 38R_0^2/\Gamma_0$ for ring EU5 at $Re = 3000$.

aiding the formation of the axial vortex as in the case of the Gaussian initialised vortex ring described in section 7.4.1. As a result an axial vortex is present in addition to the helical instability at $t = 22R_0^2/\Gamma_0$.

The helical instability is thus shown to occur in both Euler solution initialised and Gaussian initialised vortex rings with swirl.

8.5.3 Gaussian initialised vortex ring GS5 at Re=3000

The simulation of the Gaussian initialised vortex ring GS5 ($S = 0.8, \delta_0/R_0 = 0.2$) at $Re = 3000$ resulted in a helical instability. At $t = 7R_0^2/\Gamma_0$ a few different modes centred about the strongest ($n_\theta = 3, n_\phi = 2$) mode are present. Unlike in the case of the Gaussian ring GS2 at $Re = 3000$, an axial vortex is not present along with the instability (figure 8.14). The development of the instability occurs earlier than the formation of the axial vortex in this case.

8.5.4 Euler solution initialised vortex ring EU2 at Re=4500

The Euler solution initialised vortex ring EU2 ($\alpha = 60, \beta = 35$) at $Re = 4500$ develops a helical instability with ($n_\theta = 7/3, n_\phi = 3$) as seen in figure 8.15.

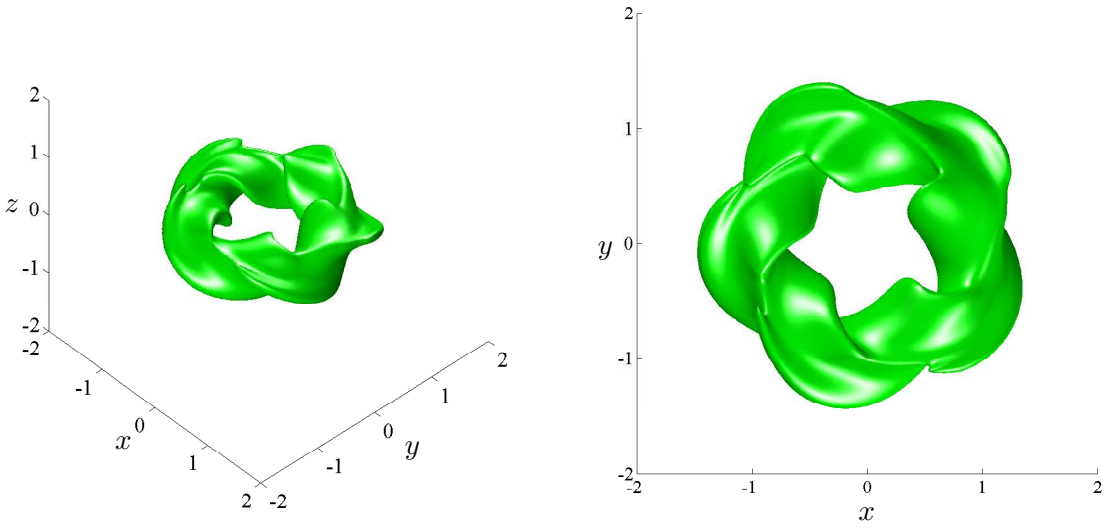

Figure 8.10: Isosurface of Q ($QR_0^4/\Gamma_0^2 = -0.5$) showing the helical structure of the instability for ring EU5 at $Re = 3000$ at $t = 38R_0^2/\Gamma_0$.

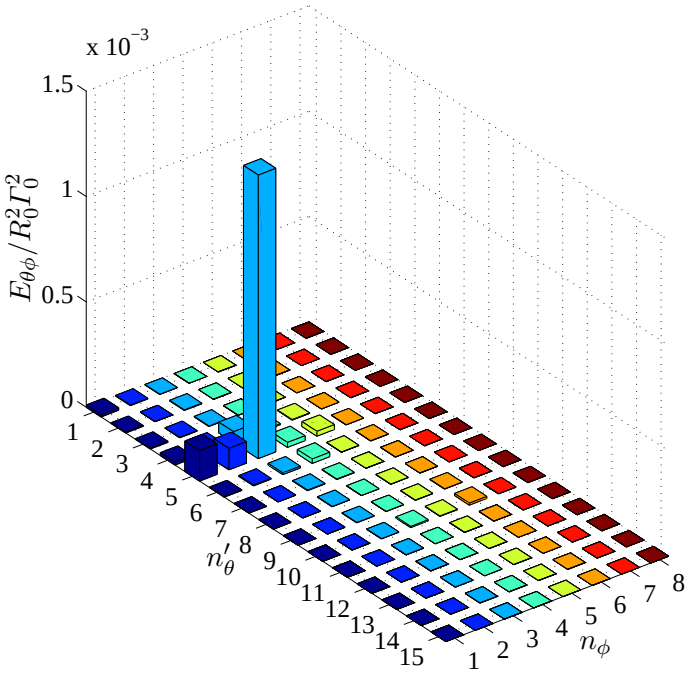

Figure 8.11: Modal energy spectrum for ring EU5 at $Re = 3000$ at $t = 38$ R_0^2/Γ_0. The shaping and twisting modes are n_ϕ and n_θ respectively.

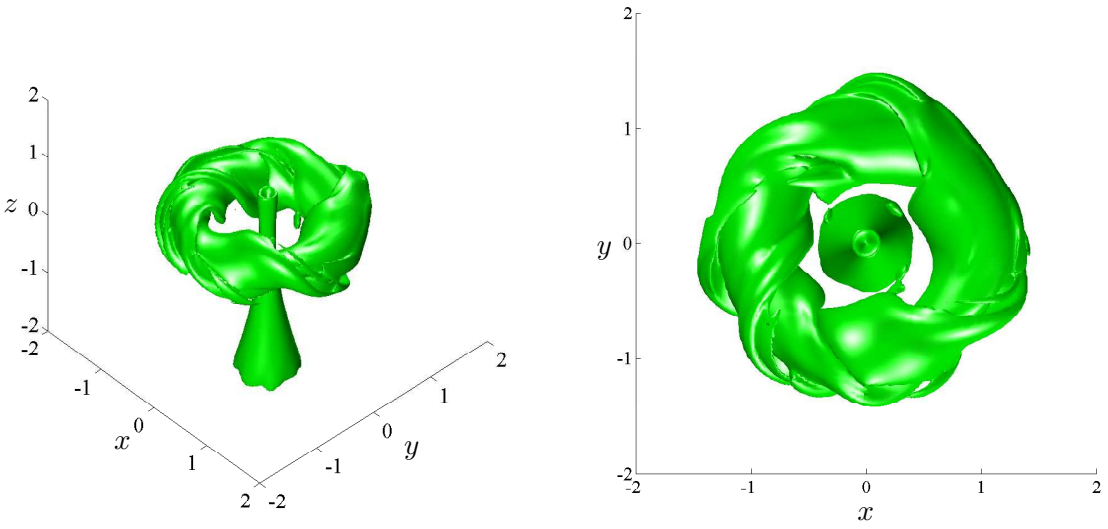

Figure 8.12: Isosurface of Q ($QR_0^4/\Gamma_0^2 = -0.5$) showing the helical instability for ring GS3 at $Re = 3000$ at $t = 22\ R_0^2/\Gamma_0$.

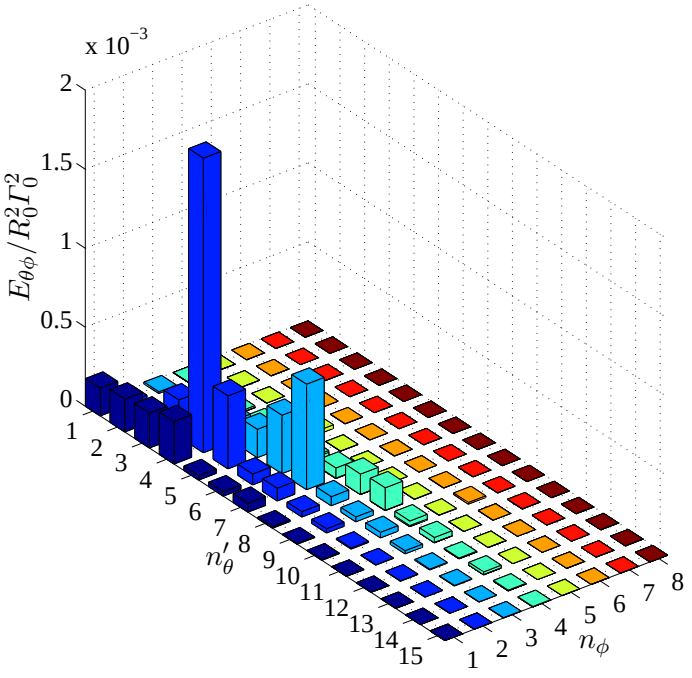

Figure 8.13: Modal energy spectrum for ring GS3 at $Re = 3000$ at $t = 22\ R_0^2/\Gamma_0$. The shaping and twisting modes are n_ϕ and n_θ respectively.

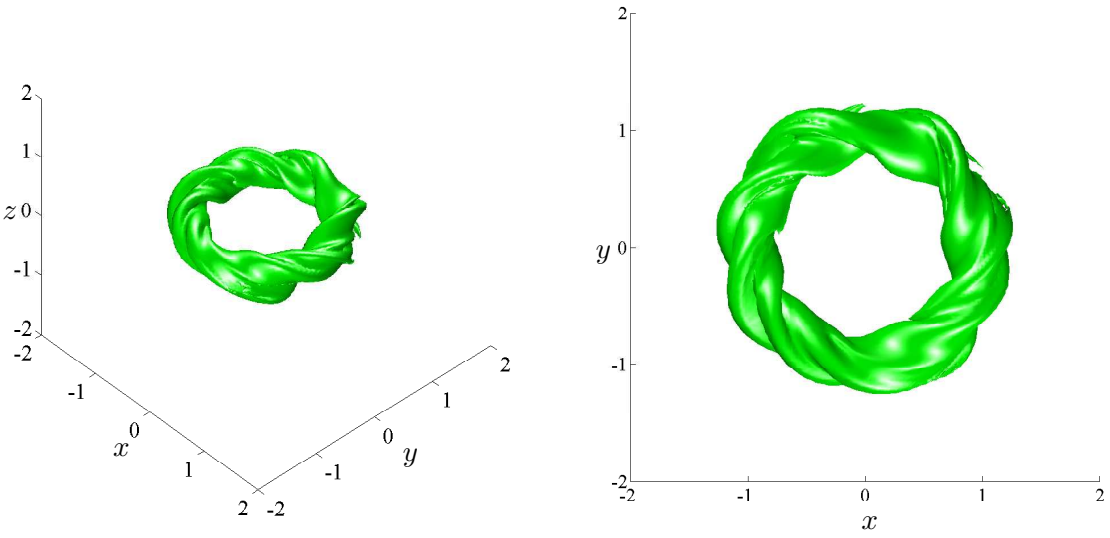

Figure 8.14: Isosurface of Q ($QR_0^4/\Gamma_0^2 = -0.1$) showing the helical instability for ring GS5 at $Re = 3000$ at $t = 7R_0^2/\Gamma_0$.

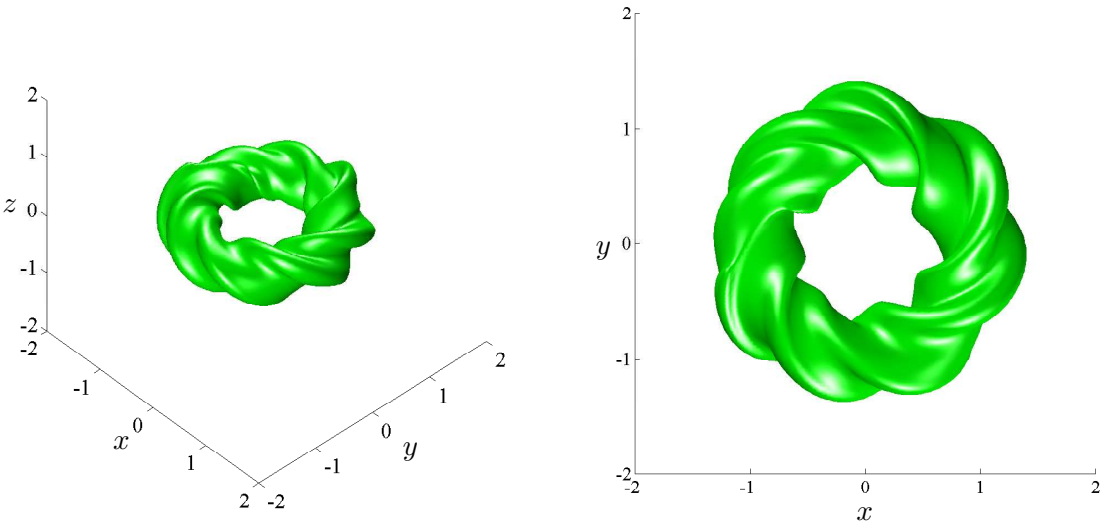

Figure 8.15: Isosurface of Q ($QR_0^4/\Gamma_0^2 = -0.1$) showing the helical instability for ring EU2 at $Re = 4500$ at $t = 17R_0^2/\Gamma_0$.

8.6 Dependence of twisting mode on slenderness ratio

In this section, the dependence of the modes of the helical instability on the geometric parameters of the vortex ring is investigated. If the pitch of the helical instability λ is assumed to scale linearly with the core radius of the vortex ring according to

$$\lambda = a\delta\,, \tag{8.5}$$

then the number of wavelengths (or 'twists') along the circumference of the vortex ring i.e. the twisting mode is given by

Vortex ring	Reynolds number	n'_θ	n_ϕ	n_θ	$t_h\Gamma_0/R_0^2$	$\epsilon(t_h)$
GS5	3000	6	2	3.00	5.50	0.208
EU4	3000	7,8	3	2.50	10.0	0.231
EU2	4500	7	3	2.33	15.0	0.255
GS3	3000	4	2	2.00	15.0	0.321
EU5	3000	5	3	1.66	34.0	0.389

Table 8.3: Modes of the helical instability occurring for each vortex ring. A representative slenderness ratio during the growth of the instability is also provided.

$$\begin{aligned} n_\theta &= \frac{2\pi R}{\lambda} \\ &= \left(\frac{2\pi}{a}\right)\frac{1}{\epsilon} \end{aligned} \tag{8.6}$$

The data from the present work is used to investigate whether the twisting mode scales linearly with the inverse of the slenderness ratio in accordance with (8.6). The values of the dominant twisting mode of the helical instabilities presented in this chapter are plotted against the inverse of the slenderness ratio at a representative time (t_h) at which the instability occurs in each case.

Table 8.3 lists the dominant shaping and twisting modes for all the instances of the helical instability presented in this chapter along with the values of t_h and the slenderness ratio at t_h in each case. The representative time t_h was chosen as the approximate time at which the period of rapid enstrophy growth associated with the instability begins. The slenderness ratios at which the instability occurs ranges from 0.2 up to nearly 0.4.

The plot of the variation of the twisting mode with the inverse of the representative slenderness ratio is presented in figure 8.16. For ring EU4, since the (7/3,3) and (8/3,3) modes are of nearly equal strength, the value of the twisting mode was taken as 2.5. The twisting mode is seen to approximately scale linearly with the slenderness ratio in agreement with (8.6) with the slope given by

$$n_\theta = \frac{0.61}{\epsilon}\,. \tag{8.7}$$

Hence the pitch of the helical instability is given by (8.5) with $a = 10.30$, so that

$$\lambda = 10.30\,\delta\,. \tag{8.8}$$

The scaling relation (8.7) indicates that small values of n_θ ($\lesssim 1$) are not permissible since they correspond to very large values of the slenderness ratio.

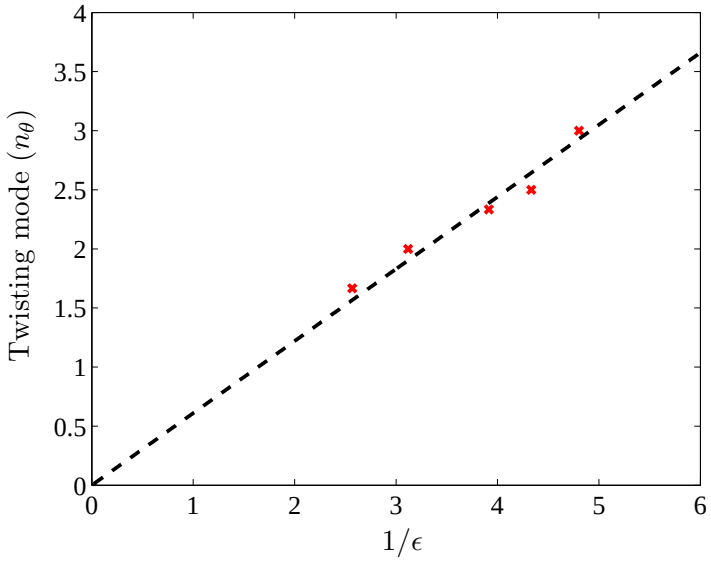

Figure 8.16: Scaling of the twisting mode n_θ with the inverse of the slenderness ratio $1/\epsilon$. Dashed line corresponds to $n_\theta = 0.61/\epsilon$.

Therefore the core size of the vortex ring determines the pitch of the instability. The number of wavelengths of the helix within the circumference of the vortex ring is the twisting mode n_θ. If an integral number of wavelengths can be fitted within a single turn around the circumference of the vortex ring, then the twisting mode is an integer. But if an integral number of wavelengths cannot be fit within the circumference, then the twisting mode is a fraction. As mentioned in section 8.4, the number of twists along the circumference can be fractional due to the fact that the vortex core cross-section is symmetric with respect to rotation in ϕ by $2\pi/n_\phi$.

An alternate explanation for the structure of the instability that accounts for the rotational symmetry of the core cross-section and the fractional twisting mode is as follows. If an integral number of wavelengths cannot be fitted within the circumference, then multiple turns around the circumference are required. The 'shaping mode' of the instability n_ϕ is actually the number of turns of the helix around the circumference. In this alternate view, the cross-sectional mode shape of the instability is a result of the superposition of n_ϕ interlacing, small amplitude helices.

With a single helix ($n_\phi = 1$), twisting modes of $1, 2, 3 \ldots$ can occur. With two interlacing helices ($n_\phi = 2$) twisting modes of $1, 3/2, 2, 5/2 \ldots$ can occur. The number of interlacing helices could be limited by the Reynolds number since at low Reynolds numbers the viscosity might prevent a high degree of interlacing by smoothing over the individual helical strands.

An explanation can now be offered for the difference between the growth of the different modes of the helical instability at Re=1500 and 3000 for ring EU4. As mentioned in section 8.4 the $n_\theta = 7/3, 8/3$ modes grow rapidly only at $Re = 3000$. At $Re = 1500$

the core size of the vortex ring grows faster than at $Re = 3000$ due to viscous diffusion. As a result the $n_\theta = 7/3, 8/3$ modes which correspond to a thinner core size than the $n_\theta = 2$ mode might not be present within the window of the most amplified modes at $Re = 1500$. Based on the alternate view of the structure of the helical instability presented above, the low growth rates of the $n_\theta = 7/3, 8/3$ modes at $Re = 1500$ might also be due to the fact that an interlacing with degree 3 (n_ϕ) might be prevented at lower Reynolds numbers.

8.7 Conclusions

An instability with a helical structure occurring in vortex rings due to swirl was described. The instability is simultaneously deforms the vortex core cross-section and twists the vortex core about its centreline along the circumference of the vortex ring. A numerical analysis method was developed to determine the exact modal structure of the instability. Using the numerical analysis method the twisting and shaping modes (n_θ and n_ϕ respectively) characterising the instability can be obtained.

The instability was found to appear only at high Reynolds numbers. The helical instability was shown to occur in both Euler solution initialised and Gaussian initialised vortex rings with swirl. Vortex rings with different initial parameters were used to obtain instances of the helical instability with a range of mode shapes. The data from the simulations of helical instability was used to show that the pitch of the helical instability scales linearly with the core size of the vortex ring. This implies that the twisting mode is determined by the slenderness ratio of the vortex ring. Based on this result, an alternate explanation for the structure of the instability was proposed. According to this explanation the deformation of the vortex core cross-section is a result of the superposition of interlacing helices. The number of interlacing helices is the shaping mode of the instability.

Chapter 9

Summary and Future work

9.1 Classical vortex rings in unbounded flow

9.1.1 Summary

The study of classical vortex rings in unbounded flow showed that the structure of the equilibrium vortex ring formed after a rapid initial readjustment is independent of the particular core azimuthal vorticity profile characterising the initial state of the vortex ring. The study was an extension of the work of Archer et al. (2008) who had identified a common equilibrium state for Gaussian initialised vortex rings. The present work showed that vortex rings with a variety of initial core vorticity profiles readjust to the common equilibrium state identified by Archer et al. (2008).

The equilibrium state is a single parameter family of vortex rings in which the structure of the core is dependent on the slenderness ratio alone. The shape of the core vorticity profile of the equilibrium vortex ring is well approximated by that of the steady state inviscid Euler solution with $\omega_\theta/r = A\psi_+^\zeta$. The exponent of the power law is determined by the slenderness ratio of the equilibrium vortex ring. The extent of the regions in the flow where the inviscid steady state condition is not satisfied increases with the slenderness ratio.

This led to an investigation of the issue of whether the common equilibrium state extends up to large times. It was found that as the slenderness ratio of the equilibrium vortex rings increased beyond ~ 0.47, they no longer followed a common path on the C vs. ϵ plot and instead diverged into multiple paths dependent on the viscosity. At this stage the growth of the vortex ring core is constrained by the entrainment bubble and the vortex ring sheds large amounts of circulation into the wake. The shape of the core vorticity profile begins to be influenced by viscosity.

By a comparison with the study of Weigand and Gharib (1997) it was shown that the behaviour of the vortex rings in the present work matched the experimental results very well both for moderate slenderness ratios at which the common equilibrium state is present and for large slenderness ratios ($\epsilon \gtrsim 0.47$) when the vortex rings follow different paths dependent on viscosity. The velocity of the vortex rings at large times was found to approach the known asymptotic solution for an axisymmetric vortex ring at large times.

9.1.2 Future work

In future work, the structure of the vortex ring at the asymptotic large time limit can be further investigated. The issue of the existence of a maximum slenderness ratio limit for a vortex ring and its relation to the large time asymptotic solution can be explored. The path of the vortex rings on the C vs. ϵ plot can also be extended upto the asymptotic limit.

9.2 Vortex ring reconnection with free-slip surface

9.2.1 Summary

The focus of the study of vortex ring reconnection with a free-slip surface was the effect of Reynolds number on reconnection. The simulation of a vortex ring starting from an initial depth below the surface and interacting with the surface at a shallow angle of incidence was performed at Reynolds numbers ranging from 500 to 10000.

Firstly the effect of Reynolds number on the reconnection timescale was investigated. Using an appropriate scaling rule to account for the variable ring geometry at the beginning of the circulation transfer, it was found that the normalised reconnection time decreases with Re at low Reynolds numbers, reaches a minimum value at $Re \simeq 2000$ and remains nearly constant with increasing Reynolds number for $Re \gtrsim 2000$. This near constant reconnection time at moderate and high Re is of the order of the inviscid timescale associated with a rotation of the vortex core about its centre. The reconnection time is maintained constant by an intensification of the process of vortex core flattening and out-of-plane stretching during reconnection with increasing Re.

At high Re due to the intense flattening, the interacting vortex core behaves like a thin, intense vortex sheet and undergoes an instability in which the head edge rolls up and detaches itself from the remaining sheet. The newly formed edge of the vortex sheet undergoes the same process again.

The problem of vortex ring reconnection with a free-slip surface was compared with the problem of a reconnecting anti-parallel vortex pair using the study of Hussain and

Duraisamy (2011). A similar trend of flattening peak circulation transfer rates with Re over a range of moderate Reynolds numbers is found in their results. At high Re, the instability occurring in the case of the vortex ring reconnection occurs during the reconnection of the anti-parallel vortex pair as well. But in the case of the latter, the antisymmetric mode of the same instability was found to occur. Along with the appearance of antisymmetric features at high Re, the peak circulation transfer rates rise sharply with Re unlike in the present case of vortex ring reconnection with a surface. A simulation of colliding vortex rings showed that the difference between the two problems at high Re persists despite the absence of the limit imposed by a free-slip surface. The antisymmetric mode of the instability does not occur during vortex ring reconnection even at high Re.

At the end of a vortex ring reconnection with a free-slip surface at high Re, the entire reconnected vortex ring structure undergoes a breakdown to a turbulent-like flow with a profusion of interlinked vortex tubes and small-scale vortical structure. The breakdown occurs as an allied effect of two phenomena: (i) Reconnection at high Re generating a thin vortex sheet and multiple vortex strands and (ii) The progressive wrapping up of the vortex strands around the bridges of reconnected surface-normal vorticity destabilising the flow and generating complex fine-scale vortical structure.

9.2.2 Future work

In the present work the effect of the inclination angle on the reconnection time has not been considered. This could be investigated in future work.

In the present work, vortex ring interactions with a non-deformable free-slip surface was studied. The work can be extended by considering reconnection of a vortex ring with a linearised free-surface with small deformation or a full free-surface. Surface parallel vorticity can be non-zero on a deformable free surface. The vorticity at the free surface interacts with the vortex ring and introduces additional dynamics.

9.3 Vortex rings with swirl in unbounded flow

9.3.1 Summary

The investigation of vortex rings with swirl was aimed at identifying characteristics of the vortex rings with swirl independent of the particular method of initialisation.

One of the defining features of a vortex ring with swirl in viscous flow was found to be the development of an elongated axial vortex. The formation of the axial vortex is the result of the following three aspects of the flow: (i) Transport of azimuthal velocity from

the core towards the axis of the vortex ring (ii) The growth of azimuthal velocity as $1/r$ as the fluid particles move closer to the axis and (iii) Annihilation of azimuthal velocity near the axis due to viscous diffusion generating an axial vortex. After its development the axial vortex is a robust and persistent feature of the flow.

An upper limit was shown to exist for the amount of swirl on a vortex ring. Vortex rings initialised with swirl above the limit undergo a rapid de-swirling readjustment ejecting fluid carrying angular momentum such that the swirl reduces to a level below the upper limit.

A helical instability occurring in vortex rings due to swirl and appearing at high Reynolds numbers was described. The helical instability simultaneously deforms the vortex core cross-section and twists the core about its centreline along the circumference of the vortex ring. The instability was shown to occur in both Euler solution initialised and Gaussian initialised vortex rings with swirl.

A numerical analysis method was developed that can identify a shaping mode and a twisting mode to characterise a particular instance of the helical instability. An investigation of the geometric parameters of the vortex rings at the time of the rapid growth of the instability found a linear scaling relationship between the pitch of the helical instability and the core size of the vortex ring. This scaling implies that the twisting mode of the instability is determined by the slenderness ratio of the vortex ring.

This finding led to an alternate explanation according to which the structure of the helical instability is due to a superposition of multiple turns of a helix whose pitch is determined by the core size of the vortex ring. According to this explanation the shape of the vortex core cross-section is a result of the superposition and the shaping mode is actually the number of turns of the helix.

9.3.2 Future work

As mentioned in section 7.5 the initial attempts at finding a scaling law for collapsing the histories of the decay of angular impulse for the different vortex rings with swirl were unsuccessful. This can be pursued further in future work.

Equilibrium vortex rings without swirl in viscous flow form a single parameter family whose core structure is determined by the slenderness ratio. It might be possible to identify a similar equilibrium family for vortex rings with swirl with additional parameters defining the angular impulse of the vortex ring and/or the strength of the axial vortex.

The possible effect of the angular impulse of the vortex rings on the growth rates of the modes of the helical instability has not been explored in the present work. This can be investigated in future work.

The well known Widnall instability occurs in vortex rings without swirl. The mode of the Widnall instability also depends on the slenderness ratio of the vortex ring similar to the twisting mode of the helical instability. The present work leads to the following question – Is the helical instability a modification of the Widnall instability due to swirl or does it represents a new kind of instability?

Appendix A

Numerical Euler solver

Eydeland and Turkington (1988) developed a numerical variational method to obtain exact steady solutions of the Euler equations for inviscid, incompressible, axisymmetric flow with a compact vorticity distribution confined to a toroidal region. These solutions form a two-parameter family. Lifschitz et al. (1996) provided a way of accurately computing the steady state solution within a truncated domain enclosing the vortex ring by imposing non-reflective boundary conditions. Their method was used in the present work to obtain vortex rings with and without swirl which are exact, steady, inviscid solutions. The method was slightly altered to obtain vortex rings with a specified radius R_0 and circulation Γ_0. The outline of the method from Lifschitz et al. (1996) is presented below.

The modified cylindrical coordinate system (y, θ, z) with $y = r^2/2$ was used. The velocity and vorticity components in terms of the Stokes stream function $\psi(y, z)$ are given by

$$\begin{aligned} \boldsymbol{u} &= -\frac{1}{\sqrt{2y}}\frac{\partial\psi}{\partial z}\hat{e}_y + u_\theta\hat{e}_\theta + \frac{\partial\psi}{\partial y}\hat{e}_z \\ \boldsymbol{\omega} &= -\frac{\partial u_\theta}{\partial z}\hat{e}_y - \frac{1}{\sqrt{2y}}\mathcal{L}\psi\hat{e}_\theta + \frac{\partial(\sqrt{2y}u_\theta)}{\partial y}\hat{e}_z\,, \end{aligned} \tag{A.1}$$

where $\mathcal{L}$ is the linear elliptic operator

$$\mathcal{L} = 2y\frac{\partial^2}{\partial y^2} + \frac{\partial^2}{\partial z^2} \tag{A.2}$$

From the Euler equations in the modified cylindrical coordinates, the following equations for u_θ and ω_θ can be obtained

$$\boldsymbol{u}.\boldsymbol{\nabla}(\sqrt{2y}u_\theta) = 0 \tag{A.3}$$
$$\boldsymbol{u}.\boldsymbol{\nabla}\left(\frac{\omega_\theta}{\sqrt{2y}}\right) - \frac{1}{2y}\frac{\partial u_\theta^2}{\partial z} = 0\,.$$

Based on these equations the azimuthal velocity and azimuthal vorticity can be expressed as

$$u_\theta = \frac{1}{\sqrt{2y}}f(\psi)\,, \tag{A.4}$$
$$\omega_\theta = -\sqrt{2y}h'(\psi) + \frac{1}{\sqrt{2y}}f(\psi)f'(\psi)\,. \tag{A.5}$$

The equilibrium equation for ψ is given by

$$\mathcal{L}\psi = 2yh'(\psi) - f(\psi)f'(\psi)\,. \tag{A.6}$$

Lifschitz et al. (1996) used the adjusted streamfunction $\tilde{\psi} = \psi + \mu + \kappa y$. To determine the values of the constants μ and κ two additional conditions are required. Lifschitz et al. (1996) used conditions which effectively specified the circulation and the axial component of the linear impulse of the vortex ring. In the present work the initial setup for the computations consisted of a vortex ring with circulation Γ_0 and radius R_0. Therefore the additional conditions used to determine μ and κ in the present work specified the circulation and the radius of the vortex ring as follows

$$-\iint \frac{1}{2y}(2yh' - ff')dydz = \Gamma_0$$
$$-\iint \frac{1}{\sqrt{2y}}(2yh' - ff')dydz = R_0\Gamma_0$$

Lifschitz et al. (1996) introduced the structure functions

$$f(\psi) = \sqrt{2\alpha/(\zeta+1)}\psi_+^{(\zeta+1)/2} \tag{A.7}$$
$$g(\psi) = h_0 - \frac{\beta}{2(\zeta+1)}\psi_+^{(\zeta+1)} \tag{A.8}$$

where $\psi_+ = \max(\psi, 0)$. The value of the positive constant h_0 is not important. Lifschitz et al. (1996) used a value of the exponent ζ as 1.5 to ensure a reasonably smooth

variation of ψ on the boundary of the compact region within which non-zero vorticity is present. The same value was adopted in the present work as well. Therefore the positive constants α and β are the parameters that determine the geometric parameters and the swirl present in the vortex ring.

The equilibrium equation reduces to

$$\mathcal{L}\tilde{\psi} = -(\alpha + \beta y)(\tilde{\psi} - \mu - \kappa y)_+^{\zeta} \,. \tag{A.9}$$

The additional conditions reduce to

$$\iint \frac{1}{2y}(\alpha + \beta y)(\tilde{\psi} - \mu - \kappa y)_+^{\zeta} \mathrm{d}y\mathrm{d}z = 1 \tag{A.10}$$

$$\iint \frac{1}{\sqrt{2y}}(\alpha + \beta y)(\tilde{\psi} - \mu - \kappa y)_+^{\zeta} \mathrm{d}y\mathrm{d}z = 1 \,. \tag{A.11}$$

Since all the flow quantities are normalized with respect to R_0 and Γ_0 in the present work, the right hand sides of (A.10) and (A.11) are taken to be unity.

Lifschitz et al. (1996) used the following non-reflective boundary conditions on the boundary of the truncated domain $D = (y, z)|0 \leq y \leq Y, -Z \leq z \leq Z$,

$$\tilde{\psi}(y, \pm Z) = \Phi(y, \pm Z),\ \tilde{\psi}(0, z) = 0,\ \tilde{\psi}(Y, z) = \Phi(Y, z) \tag{A.12}$$

where

$$\Phi(y, z) = -\iint \mathcal{G}(y, \bar{y}, z, \bar{z})(\alpha + \beta\bar{y})(\tilde{\psi} - \mu - \kappa\bar{y})_+^{\zeta} \mathrm{d}\bar{y}\mathrm{d}\bar{z} \,. \tag{A.13}$$

$\mathcal{G}$ is the Green's function for the operator $\mathcal{L}$ in free space given by

$$\mathcal{G}(y, \bar{y}, z, \bar{z}) = -\frac{1}{2\pi}\frac{(2y)^{1/4}}{(2\bar{y})^{3/4}}\left[\left(\frac{2}{k} - k\right)K(k) - \frac{2}{k}E(k)\right] \tag{A.14}$$

where $K(k)$ and $E(k)$ are complete elliptical integrals of the first and second kind of modulus k and

$$k^2 = \frac{4(2y)^{1/2}(2\bar{y})^{1/2}}{((2y)^{1/2} + (2\bar{y})^{1/2})^2 + (z - \bar{z})^2} \,.$$

A.1 Iterative method

The equilibrium equation (A.9) and the additional constraints (A.10),(A.11) need to be solved to obtain the quantities $\tilde{\psi}$,μ and κ satisfying the boundary conditions given by (A.12). Lifschitz et al. (1996) used the following iterative method.

Let the values of the required quantities at the end of the n^{th} iterative step be denoted by $\tilde{\psi}^{(n)}$,$\mu^{(n)}$ and $\kappa^{(n)}$. The following steps are performed

1. Using $\tilde{\psi}^{(n)}$,$\mu^{(n)}$ and $\kappa^{(n)}$, compute

$$\chi^{(n)} = -(\alpha + \beta y)(\tilde{\psi}^{(n)} - \mu^{(n)} - \kappa^{(n)} y)_+^{\zeta} \tag{A.15}$$

and

$$\Phi^{(n)} = \iint \mathcal{G}\chi^{(n)} \mathrm{d}y\mathrm{d}z \tag{A.16}$$

2. The boundary value problem

$$\begin{aligned} \mathcal{L}\tilde{\psi}^{(n+1)} &= \chi^{(n)} \text{ in } D \\ \tilde{\psi}^{(n+1)} &= \phi^{(n)} \text{ on } \partial D\,. \end{aligned} \tag{A.17}$$

is solved to obtain $\tilde{\psi}^{(n+1)}$. In the present work the solution was obtained using the successive over-relaxation method.

3. The quantities $\mu^{(n+1)}$ and $\kappa^{(n+1)}$ are obtained from the additional constraints

$$\iint \frac{1}{2y}(\alpha + \beta y)(\tilde{\psi}^{(n+1)} - \mu^{(n+1)} - \kappa^{(n+1)} y)_+^{\zeta} \mathrm{d}y\mathrm{d}z = 1 \tag{A.18}$$

$$\iint \frac{1}{\sqrt{2y}}(\alpha + \beta y)(\tilde{\psi}^{(n+1)} - \mu^{(n+1)} - \kappa^{(n+1)} y)_+^{\zeta} \mathrm{d}y\mathrm{d}z = 1\,. \tag{A.19}$$

using Newton's method.

The iteration procedure is initiated with $\chi^{(0)}(y,z)$ satisfying

$$\begin{aligned} -\iint \frac{1}{2y}\chi^{(0)} \mathrm{d}y\mathrm{d}z &= 1 \\ -\iint \frac{\chi^{(0)}}{\sqrt{2y}} \mathrm{d}y\mathrm{d}z &= 1\,. \end{aligned} \tag{A.20}$$

Iterations of the steps outlined above are performed until convergence is reached. The converged adjusted streamfunction field is used to obtain the vorticity field satisfying the steady state inviscid Euler equations.

References

Archer, P. J. (2008). A numerical study of laminar to turbulent evolution and free-surface interaction of a vortex ring. *Ph. D. Thesis, Aerodynamics and Flight Mechanics group, School of Engineering Sciences, University of Southampton.*

Archer, P. J., Thomas, T. G., and Coleman, G. N. (2008). Direct numerical simulation of vortex ring evolution from the laminar to the early turbulent regime. *J. Fluid Mech.*, 598:201.

Archer, P. J., Thomas, T. G., and Coleman, G. N. (2010). The instability of a vortex ring impinging on a free surface. *J. Fluid Mech.*, 642:79.

Balakrishnan, S. K., Thomas, T. G., and Coleman, G. N. (2011). Oblique interaction of a laminar vortex ring with a non-deformable free surface: Vortex reconnection and breakdown. *J. Phys. Conf. Ser.*, 318(6):062002.

Batchelor, G. K. (1967). *An Introduction to Fluid Dynamics*, chapter 7. Cambridge University Press.

Bernal, L. P. and Kwon, J. T. (1989). Vortex ring dynamics at a free-surface. *Phys. Fluids A-Fluid*, 1(3):449.

Buntine, J. D. and Pullin, D. I. (1989). Merger and cancellation of strained vortices. *J. Fluid Mech.*, 205:263.

Cantwell, B. J. and Rott, N. (1988). The decay of a viscous vortex pair. *Phys. Fluids*, 31:3213.

Chen, H. L. (1991). Numerical study on cut-and-connect of three-dimensional vortex tubes. *The Institute of Space and Astronautical Science report*, 639.

Cheng, M., Lou, J., and Lim, T. T. (2010). Vortex ring with swirl: A numerical study. *Phys. Fluids*, 22:097101.

Dabiri, J. O. and Gharib, M. (2004). Fluid entrainment by isolated vortex rings. *J. Fluid Mech.*, 511:311.

Eydeland, A. and Turkington, B. (1988). A computational method of solving free-boundary problems in vortex dynamics. *J. Comput. Phys.*, 78:194.

Fohl, T. and Turner, J. S. (1975). Colliding vortex rings. *Phys. Fluids*, 18(4):433.

Garten, J. F., Werne, J., Fritts, D. C., and Arendt, S. (2001). Direct numerical simulations of the crow instability and subsequent vortex reconnection in a stratified fluid. *J. Fluid Mech.*, 426:1.

Gharib, M. and Weigand, A. (1996). Experimental study of vortex disconnection and connection at a free surface. *J. Fluid Mech.*, 321:59.

Helmholtz, H. (1858). On integrals of the hydrodynamical equations which express vortex-motion, translation by P. G. Tait. *Phil. Mag. J. Sci. Series 4*, 33:485.

Hu, G. H., Sun, D. J., and Yin, X. Y. (2001). A numerical study on vortex rings with swirl. *J. Hydrodyn.*, B,2:1.

Hussain, F. and Duraisamy, K. (2011). Mechanics of viscous vortex reconnection. *Phys. Fluids*, 23(2):021701.

Izutsu, N. and Oshima, Y. (1991). Hot-wire measurement of cross-linking and unlinking in uniting two circular vortex rings. *Institute of space and astronautical science report*, 638.

J. Jeong, J. and Hussain, F. (1995). On the identification of a vortex. *J. Fluid Mech.*, 285:69.

Kambe, T. (1983). A class of exact-solutions of two-dimensional viscous flow. *J. Phys. Soc. Jpn.*, 52(3):834.

Kambe, T. and Oshima, Y. (1975). Generation and decay of viscous vortex rings. *J. Phys. Soc. Jpn.*, 38:271.

Kambe, T. and Takao, T. (1971). Motion of distorted vortex rings. *J. Phys. Soc. Jpn.*, 31(2):591.

Kelvin, L. (1867). The translatory velocity of a circular vortex ring. *Phil. Mag*, 33:511.

Kida, S., Takaoka, M., and Hussain, F. (1991). Collision of two vortex rings. *J. Fluid Mech.*, 321:59.

Kida, S., Takaoka, S. M., and Hussain, F. (1989). Reconnection of 2 vortex rings. *Phys. Fluids A-Fluid*, 1(4):630.

Lifschitz, A., Suters, W. H., and Beale, J. T. (1996). The onset of instability in exact vortex rings with swirl. *J. Comput. Phys.*, 128:8.

Melander, M. V. and Hussain, F. (1989). Cross-linking of two antiparallel vortex tubes. *Phys. Fluids*, 1(4):633.

Moffatt, H. K. (1988). Generalised vortex rings with and without swirl. *Fluid Dyn. Res.*, 3:22.

Norbury, J. (1973). A family of steady vortex rings. *J. Fluid Mech.*, 57:417.

Ooi, A., Soria, J., Lim, T. T., Kollmann, W., and Chong, M. S. (2001). A numerical study of swirling vortex rings. In *Fourteenth Australasian Fluid Mechanics Conference.*

Oshima, Y. and Asaka, S. (1975). Interaction of two vortex rings moving side by side. *Natural Science Report, Ochanomizu University*, 26(1):31.

Oshima, Y. and Asaka, S. (1977). Interaction of 2 vortex rings along parallel axes in air. *J. Phys. Soc. Jpn.*, 42(2):708.

Oshima, Y. and Izutsu, N. (1988). Cross-linking of 2 vortex rings. *Phys. Fluids*, 31(9):2401.

Pumir, A. and Siggia, E. D. (1987). Vortex dynamics and the existence of solutions to the navier-stokes equations. *Phys. Fluids*, 30(6):1606.

Redford, J. A., Castro, I. P., and Coleman, G. N. (2012). On the universality of turbulent axisymmetric wakes. *J. Fluid Mech.*, 710(10):419.

Rees, W. M. V., Hussain, F., and Koumoutsakos, P. (2012). Vortex tube reconnection at Re = 10000. *Phys. Fluids*, 24(7):075105.

Saffman, P. G. (1970). The velocity of viscous vortex rings. *Stud. App. Math.*, 49:371.

Saffman, P. G. (1990). A model of vortex reconnection. *J. Fluid Mech.*, 212:395.

Saffman, P. G. (1992). *Vortex dynamics*, chapter 3. Cambridge University Press.

Schatzle, P. (1987). An experimental study of fusion of vortex rings. *Ph. D. Thesis, California Institute of Technology.*

Serrin, J. (1959). Mathematical principles of classical fluid mechanics in: S. Flügge. *Encyclopedia of Physics*, page 125.

Shelley, M. J., Meiron, D. I., and Orszag, S. A. (1993). Dynamic aspects of vortex reconnection of perturbed anti-parallel vortex tubes. *J. Fluid Mech.*, 246:613.

Stanaway, S. K., Cantwell, B. J., and Spalart, P. R. (1988). A numerical study of viscous vortex rings using a spectral method. *NASA Technical Memorandum*, 101041.

Thomas, T. G. and Williams, J. J. R. (1997). Development of a parallel code to simulate skewed flow over a bluff body. *J. Wind Eng. Ind. Aerod.*, 67,68:155.

Turkington, B. (1986). Vortex rings with swirl: axisymmetric solutions of the euler equations with nonzero helicity. *SIAM J. Math. Anal.*, 20:57.

Virk, D., Melander, M. V., and Hussain, F. (1994). Dynamics of a polarized vortex ring. *J. Fluid Mech.*, 260:23.

Weigand, A. and Gharib, M. (1995). Turbulent vortex ring free surface interaction. *J. Fluid Eng-T ASME*, 117(3):374.

Weigand, A. and Gharib, M. (1997). On the evolution of laminar vortex rings. *Exp. Fluids*, 22(6):447.

Widnall, S. E., Bliss, D. B., and Tsai, C. Y. (1974). The instability of short waves on a vortex ring. *J. Fluid Mech.*, 66:35.

Yao, Y. F., Thomas, T. G., Sandham, N. D., and Williams, J. J. R. (2001). Direct numerical simulation of turbulent flow over a rectangular trailing edge. *Theoret. Comput. Fluid Dyn.*, 14:337.

Zhang, C., Shen, L., and Yue, D. K. P. (1999). The mechanism of vortex connection at a free surface. *J. Fluid Mech.*, 384:207.